



HAL
open science

Solid-State Conversion of Positive Electrode Materials into Water-soluble Sulfates for Easier Metals Recycling of Spent Li-ion Batteries

Lydia Hamitouche

► **To cite this version:**

Lydia Hamitouche. Solid-State Conversion of Positive Electrode Materials into Water-soluble Sulfates for Easier Metals Recycling of Spent Li-ion Batteries. Analytical chemistry. Sorbonne Université, 2022. English. NNT: 2022SORUS511 . tel-04127615

HAL Id: tel-04127615

<https://theses.hal.science/tel-04127615v1>

Submitted on 14 Jun 2023

HAL is a multi-disciplinary open access archive for the deposit and dissemination of scientific research documents, whether they are published or not. The documents may come from teaching and research institutions in France or abroad, or from public or private research centers.

L'archive ouverte pluridisciplinaire **HAL**, est destinée au dépôt et à la diffusion de documents scientifiques de niveau recherche, publiés ou non, émanant des établissements d'enseignement et de recherche français ou étrangers, des laboratoires publics ou privés.



Sorbonne Université

Ecole doctorale – ED 388 – Chimie Physique et Chimie Analytique de Paris centre

Laboratoire PHENIX

Doctorat en chimie physique et chimie analytique

Solid-State Conversion of Positive Electrode Materials into Water-soluble Sulfates for Easier Metals Recycling of Spent Li-ion Batteries

Lydia HAMITOUCHE

Directeur de thèse : Damien DAMBOURNET

Thèse présentée et soutenue publiquement le 13 décembre 2022

Devant un jury composé de :

Prof. Christel Laberty-Robert	Professeur, LCMCP, Sorbonne Université	Présidente
Prof. Dany Carlier-Larregaray	Professeur, ICMCB, Université de Bordeaux	Rapporteur
Prof. Lorenzo Stievano	Professeur, ICGM, Université de Montpellier	Rapporteur
Prof. Christian Masquelier	Professeur, LRCS, UPJV Amiens	Examineur
Dr. Damien Dambournet	Maître de conférences, PHENIX, Sorbonne Université	Directeur

Remerciements

Le présent travail a été réalisé au sein du Laboratoire PHENIX, à Sorbonne université. Il a été financé par le CNRS dans le cadre d'un projet ANR Reliable.

Je voudrais exprimer ma gratitude sincère envers Damien DAMBOURNET, mon directeur de thèse. Il a été incroyablement disponible et m'a apporté un soutien constant tout au long de mon parcours de thèse. Il m'a accordé sa confiance et m'a permis de travailler dans des conditions optimales. Je tiens à lui témoigner ici toute ma reconnaissance.

Je suis profondément reconnaissante envers le Professeur Dany Carlier-Larregaray, le Professeur Lorenzo Stievano, le Professeur Christel Laberty-Robert et le Professeur Christian Masquelier d'avoir accepté de faire partie du jury.

Je souhaite également exprimer ma gratitude envers les membres du laboratoire PHENIX pour leur accueil chaleureux. Pendant les trois années de ma thèse, j'ai eu la chance de travailler avec Anne-Laure ROLLET, Denise KRULIC, Nicolas FATOUROS, Ana Gabriela PORRAS GUTIERREZ, Sandrine LECLERC, José GOMES et Juliette SIRIEIX PLENET, je les remercie pour le temps qu'ils m'ont consacré. Également, je tiens à adresser mes remerciements particuliers à tous les collaborateurs qui m'ont aidé à accomplir ce travail.

J'aimerais également remercier toutes les personnes qui sont chères à mon cœur : mes parents, qui représentent ma plus grande source de motivation et de force ; ma sœur et mon frère, avec qui j'ai partagé de bons moments ; et je voudrais remercier Aymene BITAM, qui m'a constamment soutenu, aidé et accompagné de manière inestimable.

Enfin, je tiens à remercier tous mes amis, qu'ils soient thésards ou non, et en particulier : Briséis MERCADIER, Kyle REEVES, Kateryna GOLOVIZNINA et Maxime SORRIAUX, dont la bonne humeur, la gentillesse et l'aide ont rendu ma thèse aussi agréable qu'elle l'a été.

Table of contents

Chapter I.	Introduction to lithium-ion batteries and recycling.....	11
I.1	Chemistry of Li-ion battery.....	11
I.1.1	Working principle of Li-ion batteries.....	11
I.1.2	History of Li-ion batteries.....	13
I.1.3	Composition of Li-ion batteries.....	13
I.2	Applications of Li-ion batteries.....	18
I.3	Recycling processes of spent Li-ion battery.....	21
I.3.1	Pyrometallurgical process.....	23
I.3.2	Hydrometallurgical process.....	24
I.3.3	Direct recycling.....	26
I.3.4	Alternative recycling process: Deep eutectic solvent.....	28
I.3.5	Salt conversion approach.....	28
I.4	Conclusion.....	29
Chapter II.	Investigation of the sulfation conversion of lithiated transition metal oxide using potassium hydrogensulfate.....	32
II.1	Introduction.....	32
II.2	Reaction parameters.....	33
II.2.1	Reaction stoichiometry.....	33
II.2.2	Effect of the temperature.....	34
II.2.3	Effect of the atmosphere.....	35
II.3	Identification of the sulfation equation.....	37
II.4	Extension to NMC and NCA layered positive electrode materials.....	42
II.4.1	Crystal structure of Langbeinite $K_2M_2(SO_4)_3$	42
II.4.2	Extension to NMC and NCA positive electrode materials.....	43
II.4.3	Conclusion.....	49

II.5	Mechanistic investigation	50
II.5.1	Differential scanning calorimetry.....	50
II.5.2	Variable-temperature XRD analysis	52
II.5.3	X-ray absorption spectroscopy	56
II.6	DFT-calculations	80
II.6.1	Electronic structure of LiCoO ₂	80
II.6.2	Substitutions Li ⁺ /H ⁺	82
II.7	Conclusion.....	85
Chapter III. Lux-Flood concept applied to sulfation of lithiated transition metal oxides.....		88
III.1	Introduction	88
III.2	Reaction conditions	90
III.3	From oxide to sulfate: transformation mechanism	93
III.3.1	Variable temperature XRD analysis.....	93
III.3.2	X-ray absorption spectroscopy	97
III.4	Conclusion.....	105
Chapter IV. General conclusion		108

Context

Li-ion batteries (LIBs) have become extremely popular since their commercialization by SONY in 1991. One of major components of Li-ion batteries is the positive electrode. This latter is made of lithiated transition metal oxide LiMO_2 ($M = \text{Co}, \text{Ni}, \text{Mn}$). In the recent years, the LIB production grows rapidly due to their use in electric vehicles, which induce an increase in the use of raw materials. This raising is expected to be further enhanced in the future, as European environment minister support a goal of 100% reduction of CO_2 emissions by 2035 *i.e.* a transition to 100% electric vehicle¹. However, the large production and application of LIBs causes depletion of raw material. In addition, it will unfortunately lead to a large number of spent LIBs, bringing about environmental problems. Therefore, recycling of spent LIBs has both environmental and economic benefits.

Several processes have been developed to recycle spent LIBs (**Figure -1**). The industrial process includes pyrometallurgy and hydrometallurgy, while, direct recycling is still under development. The pyrometallurgical is a high-temperature process and the hydrometallurgical is a low temperature process based on the lixiviation of positive electrode material in acidic solution. These processes are efficient for metal recycling *i.e.* Co and Ni. Nevertheless, both pyrometallurgy and hydrometallurgy have disadvantages such as less recovery of the lithium, manganese and aluminum. As reported by United Nation Environment Programme (UNEP) less than 1% of lithium is being recycled². In addition, they require extensive off-gas and effluent treatment. Therefore, development of new recycling approach is crucial to overcome the drawback of pyro and hydro- metallurgical processes.

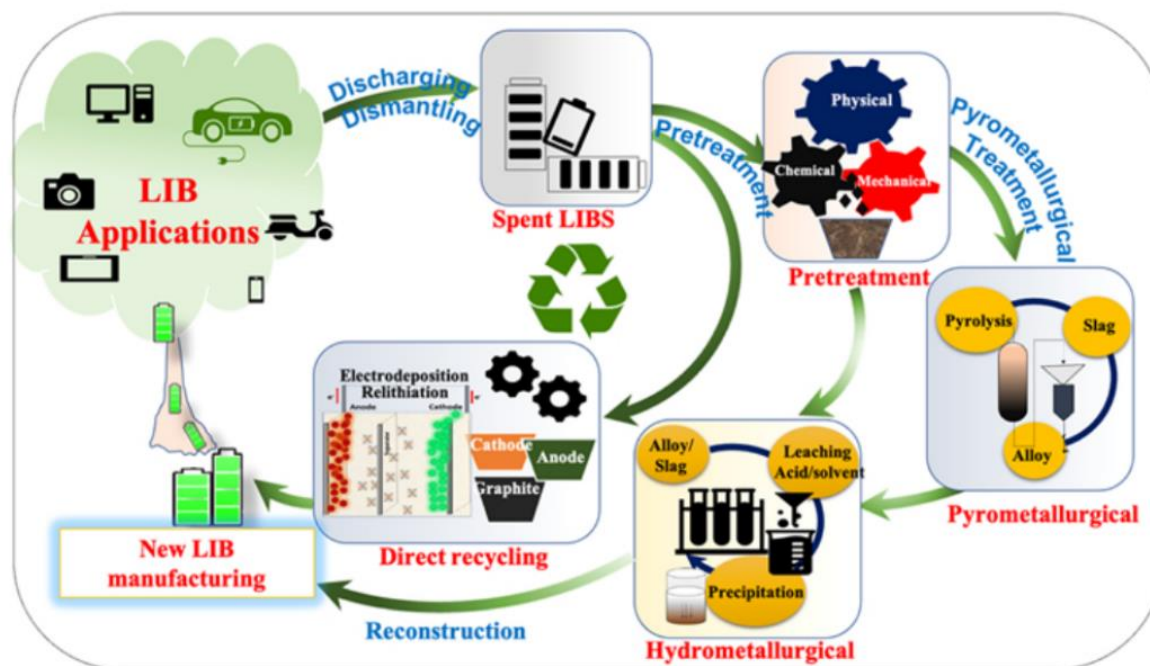


Figure -1: Recycling processes of spent Li-ion batteries³.

Thesis outline

The aim of this work, is to developed new approach to recycling positive electrode material of spent Li-ion batteries. This approach consists on the solid-state conversion of positive electrode material LMO (with M= Co, Ni, Mn, and Al) into water soluble sulfate-based product using molten salt. During this work, the reaction condition and conversion mechanism will be investigated. We selected two different molten salt, hydrogen potassium sulfate KHSO_4 and potassium pyrosulfate $\text{K}_2\text{S}_2\text{O}_7$ to convert positive electrode material of spent LIBs into soluble sulfate product.

This work is divided in four chapters:

The first chapter provides an overview of the principle, the composition of positive electrode material and the application of Li-ion batteries. This chapter reveals the importance and challenges of the recycling of spent Li-ion batteries. The recycling processes currently used will be presented in order to clarify the need for a new recycling approach, as well as the understanding of its reaction mechanism.

In the second chapter, hydrogenosulfate (KHSO_4) molten salt with melting point of 200°C^4 is used to convert positive electrode material LMO ($\text{M}=\text{Co}, \text{Ni}, \text{Mn}, \text{and Al}$) into water soluble-sulfate product: $\text{K}_2\text{M}_2(\text{SO}_4)_3$, KLiSO_4 , and K_2SO_4 . The effect of molar ratio LMO: KHSO_4 , reaction temperature, and atmosphere on the sulfation rate were studied, for LiCoO_2 , and then extended to NMC and NCA. The reaction mechanism involved upon the sulfation of LiCoO_2 with KHSO_4 is investigated. The variable-temperature XRD and X-ray absorption spectroscopy (XAS) reveals an ionic exchange H^+/Li^+ and formation of cobalt hydroxy sulfate $\text{Co}_3(\text{SO}_4)_2(\text{OH})_2$ prior to conversion into $\text{K}_2\text{Co}_2(\text{SO}_4)_3$. Furthermore, DFT calculation are performed to deeply understand the conversion mechanism.

The third chapter focus on the conversion of LiCoO_2 into sulfate product using $\text{K}_2\text{S}_2\text{O}_7$ free hydrogen molten salt with melting point of 400°C^5 . The resulting sulfate products are similar to those obtained with KHSO_4 . However, the reaction mechanism is different. Thereafter, the conversion mechanism is studied by variable-temperature XRD and XAS analyses. The results show that the reaction between LiCoO_2 and $\text{K}_2\text{S}_2\text{O}_7$ occurs according to the Lux-Flood theory^{6,7}. The Li and Co elements evolves as follow: $\text{Co}, \text{LiCoO}_2 \rightarrow \text{Li}_{1-2x}\text{CoO}_{2-x}\square_x \rightarrow \text{Co}_3\text{O}_4 \rightarrow \text{K}_2\text{Co}_2(\text{SO}_4)_3$ and $\text{Li}, \text{LiCoO}_2 \rightarrow \text{KLiSO}_4$.

To conclude, the main result of this work will be summarized in chapter IV, and the comparison between the two sulfation processes will be discussed.

Chapter I. Introduction to lithium-ion batteries and recycling

I.1 Chemistry of Li-ion battery

I.1.1 Working principle of Li-ion batteries

Rechargeable Li-ion batteries (LIBs) are electrochemical cells with ability to convert chemical energy to electrical energy through reversible redox reactions. **Figure I-1** shows a schematic representation of a LIB. It featuring a positive electrode typically made of lithiated transition metal oxide, a negative electrode made of graphite, and an electrolytic solution composed of an organic solvent (ethylene carbonate (EC) + dimethyl carbonate (DMC)) and a lithium salt (e.g. LiPF_6). Depending on the nature of the reaction, the positive and the negative electrodes are called also “cathode” and “anode”. The anode is the electrode where the oxidation reaction occurs, and the cathode represent the electrode where the reduction reaction take place. During discharge step, an oxidation reaction occurred at the negative electrode, the Li^+ ions are deintercalated and migrate through the electrolyte to reach the positive electrode. Simultaneously, the electrons flow through external circuit from negative to positive electrode, wherein the reduction reaction occurs.

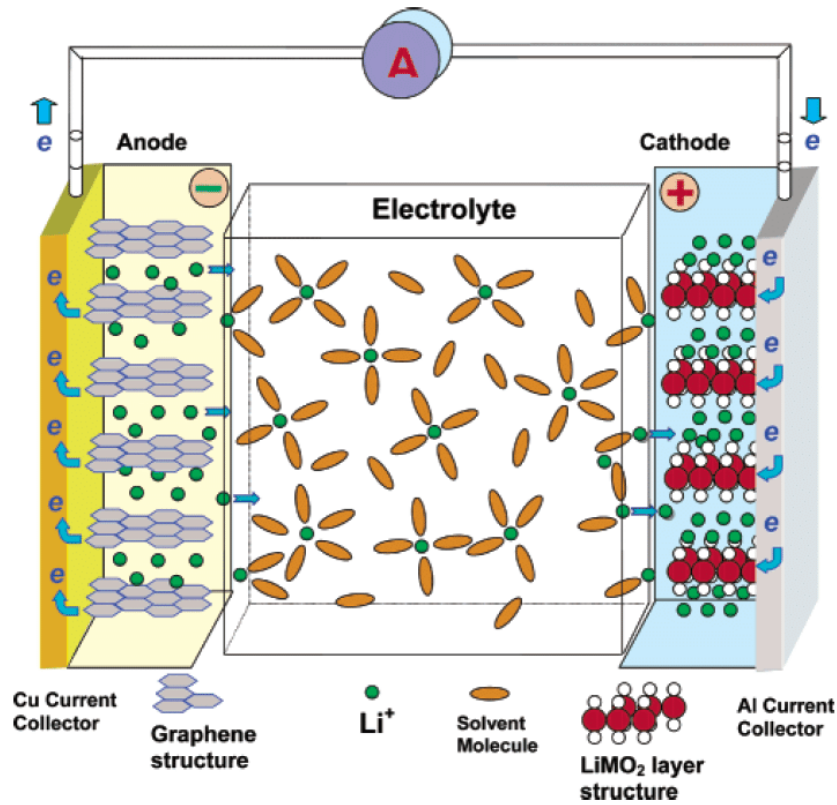


Figure I-1: Schematic representation of Li-ion batterie during discharge process⁸.

The voltage of Li-ion battery is the difference between the electrochemical potential of the anode μ_A and cathode μ_C (**Equation I-1**).

Equation I-1:

$$V_{oc} = \mu_A - \mu_C / e$$

Where, V_{oc} is the open-circuit voltage, and e is the magnitude of the electron charge.

The cell capacity Q is the total quantity of electrical energy generated through the electrochemical reactions per unit weight of the battery ($Ah \cdot Kg^{-1}$). It is related to the quantity of Li^+ ions intercalated/ deintercalated from the positive and negative electrode.

Equation I-2:

$$Q (Ah/kg) = \frac{F \times n(Li^+)}{3600 \times M}$$

Where F is Faraday number, $n(Li^+)$ is the number of Li^+ ions, and M is the molecular weight of the electrode material.

The energy density E_{specific} of a cell is the quantity of energy that can be stored in cell.

Equation I-3:

$$E_{\text{specific}} (\text{Wh/Kg}) = Q(\text{Ah/Kg}) \cdot V (\text{V})$$

I.1.2 History of Li-ion batteries

Since its commercialization by Sony in 1991, the LIB has known a great success in various energy storage applications. In recent years, LIBs have been used to power electric vehicles (EVs). Owing to the qualitative leap achieved by this technology in the field of energy, Stanley Whittingham, John B. Goodenough and Akira Yoshino have been awarded by the Nobel prize of chemistry in 2019⁹ for their contribution to the development of these devices.

Whittingham reported the first rechargeable battery in 1976¹⁰, it was composed of layered TiS_2 as positive electrode material, lithium metal as negative electrode material, and lithium perchlorate in dioxolane as the electrolyte. This battery has a good performance. However, upon repetitive charge and discharge cycles, lithium dendrites form, causing an internal short circuit. In 1980, Goodenough¹¹ reported the electrochemical properties of LiCoO_2 as positive electrode material. The use of oxide instead of sulfides is related to the energy gap between top band of oxide and sulfite relative to the negative electrode (Li). The bands O-2p is around 4 eV below electrochemical potential of the negative electrode (Li), while the sulfide S-3p bands of the layered sulfides LiMS_2 is around 2.5 eV below the electrochemical potential of the negative electrode (Li). Later, in 1986, Yoshino¹² improves LIB by replacing the pure lithium in the negative electrode by the carbonaceous to circumvent the safety issued surrounding the use of Li metals.

I.1.3 Composition of Li-ion batteries

As mentioned before, the LIBs are composed of three main components positive electrode, negative electrode, and electrolyte. In the present study, we will focus only on the positive electrode material.

- **LiCoO₂**: The LiCoO_2 (LCO) is the first commercialized positive electrode material. It has $\alpha\text{-NaFeO}_2$ -type layered structure with $R\bar{3}m$ space group. **Figure I-2** shows structure of LiCoO_2 , the oxygen atoms are arranged in a cubic close-packed, Li^+ and Co^{3+} are ordered in alternating

planes, and located respectively in octahedral (3a) and (3b) Wyckoff positions. Moreover, LCO has high open circuit voltage 3.9 - 4.7 V. Nevertheless, upon high voltage cycling, its capacity falls. The performances decay is related to the structural modifications of LiCoO_2 under charge/discharge process at high voltage cycling. It was demonstrated that, at near half of delithiation *i.e.* $\text{Li}_{0.5}\text{CoO}_2$, transition phase from hexagonal to monoclinic occurs. The formed monoclinic structure is unstable causing capacity loss. For this reason, LiCoO_2 delivers only half of its theoretical capacity (280 mAh/g). In addition, at the deeper delithiation rate, the irreversible phase transformation from hexagonal to spinel was observed. Indeed, the deeper extraction of lithium on the surface lead to the oxidation of O^{2-} and thereafter, the loss of oxygen from the surface, causing the formation of the spinel structure Co_3O_4 ¹³. Therefore, to improve the proprieties of layered structure, cobalt has been substituted by nickel, manganese, or aluminum yielding to NMC and NCA type positive electrode material.

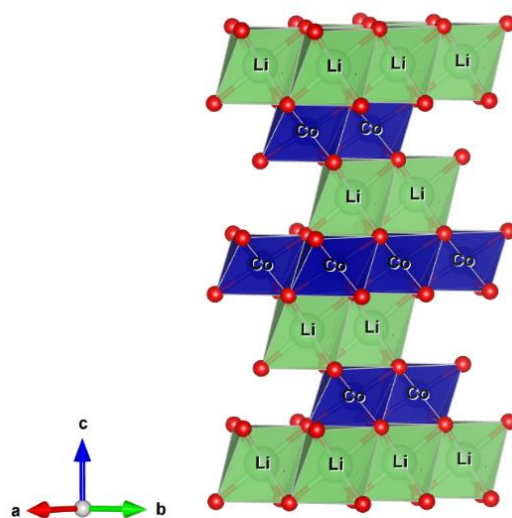


Figure I-2: Polyhedral and ball-and-stick representation of layered LiCoO_2 positive electrode material, with ABC stacking.

- **$\text{LiNi}_x\text{Co}_y\text{Mn}_z\text{O}_2$:** The NMC positive electrode material is isostructural with LiCoO_2 , wherein, Co, Ni, and Mn form solid solution. Different type of NMC exist, e.g. $\text{LiNi}_{1/3}\text{Mn}_{1/3}\text{Co}_{1/3}\text{O}_2$ (NMC 111), $\text{LiNi}_{0.8}\text{Mn}_{0.1}\text{Co}_{0.1}\text{O}_2$ (NMC 811), $\text{LiNi}_{0.6}\text{Mn}_{0.2}\text{Co}_{0.2}\text{O}_2$ (NMC 622). It shows higher specific capacity and lower structural failure compared to LiCoO_2 . The structural stability of NMC is related to the presence of Mn^{IV} and Ni^{II} with higher energy gap between transition metal and O-2p (**Figure I-3**), this reducing the formation of O_2 , therefore,

the O3 layered structure is maintained. The Mn^{4+} remains at constant oxidation state during charge/ discharge process, promoting long life cycle. While, the presence of Ni^{3+} offer the high capacity. However, the large amount of nickel reduces the thermal stability of NMC positive electrode causing decrease of electrochemical performances¹⁴. For example, NMC 111 has the best thermal stability and capacity retention, but, it presents low discharge capacity (~ 150 mAh/g) due to the poor Ni amount. At the opposite compound rich in Ni, NMC 811 present high discharge capacity ~200 mAh/g, but, it has low thermal stability and retention capacity.

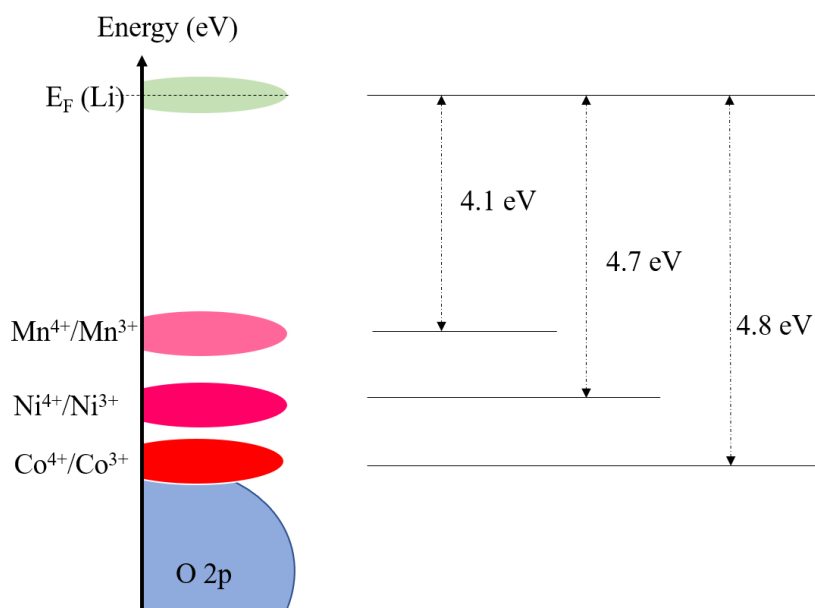


Figure I-3: Relative position of energy levels and typical electron configuration of Mn, Ni and Co.

- **$\text{LiNi}_x\text{Co}_y\text{Al}_z\text{O}_2$:** In the same way, to increase the capacity of positive electrode materials, researchers have been focused on $\text{LiNi}_x\text{Co}_y\text{Al}_z\text{O}_2$ (NCA). The commercialized NCA positive electrode material is $\text{Li}[\text{Ni}_{0.82}\text{Co}_{0.15}\text{Al}_{0.03}]\text{O}_2$. It has high capacity $199 \text{ mAh}\cdot\text{g}^{-1}$, high voltage 3.7 V, and good cycling life. The structural stability of NCA has been attributed to the presence of Al^{3+} ions¹⁵.

- **LiMn_2O_4 spinel structure:** Spinel oxides with the chemical formula LiMn_2O_4 (LMO) were first proposed by Thackeray *et al* in the early 1980s¹⁶. **Figure I-4** shows the spinel LMO structure with $\text{Fd}\bar{3}m$ space group, the Mn cation occupies the octahedral site (16d), and Li occupies the tetrahedral (8a). The structure gives 3D diffusion network for Li^+ ions. LiMn_2O_4 has a high voltage 4V but low capacity (~ 120 mAh/g). The cycling performance are not

satisfactory due to the dissolution of Mn upon several charge/discharge processes, limiting its uses in EVs.

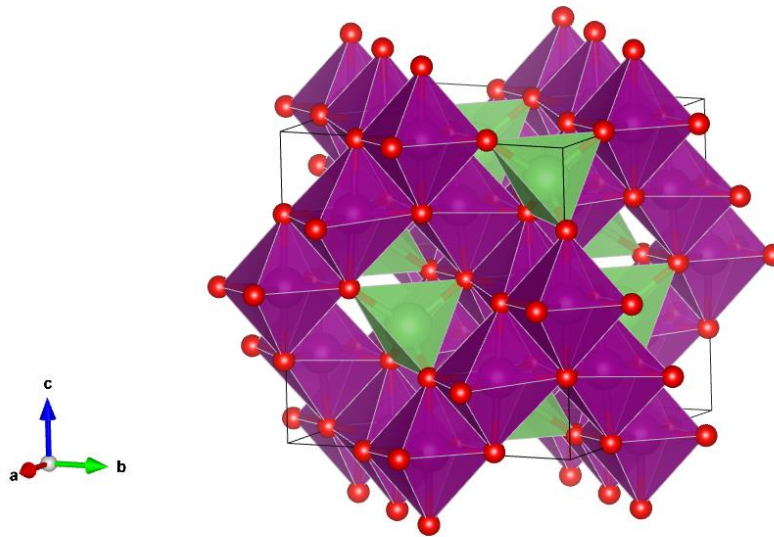


Figure I-4: LiMn_2O_4 spinel structure ($Fd\bar{3}m$), Mn cation are situated in octahedra site (purple), Li in tetrahedral site (green) and oxygen (red sphere).

- **Olivine Phosphates LiFePO_4 :** The phosphate material LiFePO_4 (LFP) was first reported by Padhi *et al.*¹⁷. It has an orthorhombic structure with $Pnma$ space group. The Li and Fe, occupy distorted octahedral (4a) and octahedral (4c) Wyckoff sites, respectively. While, P atoms are in tetrahedral (4c) Wyckoff sites (**Figure I-5**). LiFePO_4 has the experimental specific capacity close to the theoretical capacity 170 mAh/g ¹⁸, nevertheless, its energy density is lower due to its low operating voltage 3.4 V .

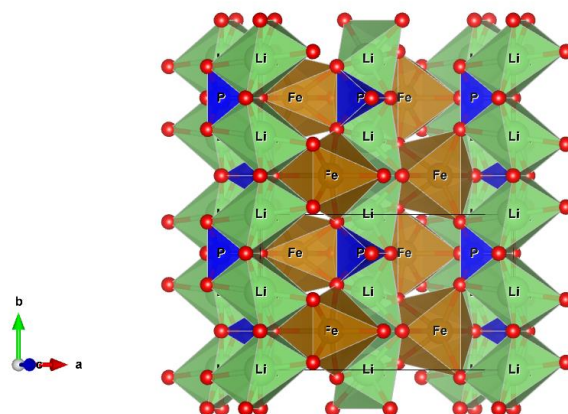
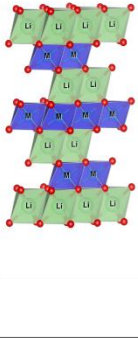
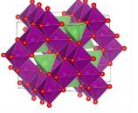
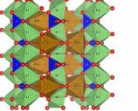


Figure I-5: Olivine Phosphates LiFePO_4 structure, Li (green octahedra), Fe (brown octahedra), P (bleu tetrahedra), O (red sphere).

Table I-1 summarize the structures of positive electrode materials and their electrochemical characteristics. Layered LiCoO_2 offers relatively high voltage 3.9 V, high energy, and high-power density storage with long life cycle performance. However, its reversible capacity is about 140 mAh/g, which is lower compared to NMC (~180 mAh/g) and NCA (~200 mAh/g). positive electrode material. The spinel LiMn_2O_4 present interesting proprieties such as high voltage ~ 4.1 V. Nevertheless, it has limited cycle life and low capacity (~ 120 mAh/g). while, the olivine LiFePO_4 has a higher capacity compared to LiCoO_2 (~ 165 mAh/g), but, its present low voltage.

Table I-1: Composition, chemistries and electrochemical performances of positive electrode material of LIBs.

LIBs cathode chemistries									
		Ideal						Poor	
Crystal structure	Structure	Cathode type	Year commercialized	Specific capacity (mAh.g ⁻¹)		Average voltage	Safety	Cost	
Layered		LiCoO ₂	1991	148	562	3.8	● ●	●	
		LiNi _{0,33} Co _{0,33} Mn _{0,33} O ₂	2008	150	555	3.7	● ● ● ●	● ● ● ●	
		LiNi _{0,5} Co _{0,3} Mn _{0,2} O ₂		170	629				
		LiNi _{0,6} Co _{0,2} Mn _{0,2} O ₂		180	666				
		LiNi _{0,8} Co _{0,1} Mn _{0,1} O ₂		200	740				
LiNi _{0,85} Co _{0,15} Al _{0,03} O ₂	1999	199	736	3.7	● ● ● ●	● ● ● ●			
Spinel		LiMn ₂ O ₄	1996	120	492	4.1	● ● ● ● ● ●	● ● ● ● ● ●	
Olivine		LiFePO ₄	1996	165	561	3.4	● ● ● ● ● ● ● ●	● ● ● ● ● ● ● ●	

I.2 Applications of Li-ion batteries

The long cycle life, high power density and high thermal stability of LIBs, have enable the extension of their application fields. **Figure I-6** shows three main application fields. The first applications were in consumer electronics and devices, thereafter, the LIB rapidly extended to large format applications that are transportation and industrial energy storage. This extension was assisted by the use of positive electrode material containing multiple transition metals. Indeed, The LCO positive electrode material are usually used for consumer electronics and devices. While, NMC, NCA, and LFP are used in transportation industry.

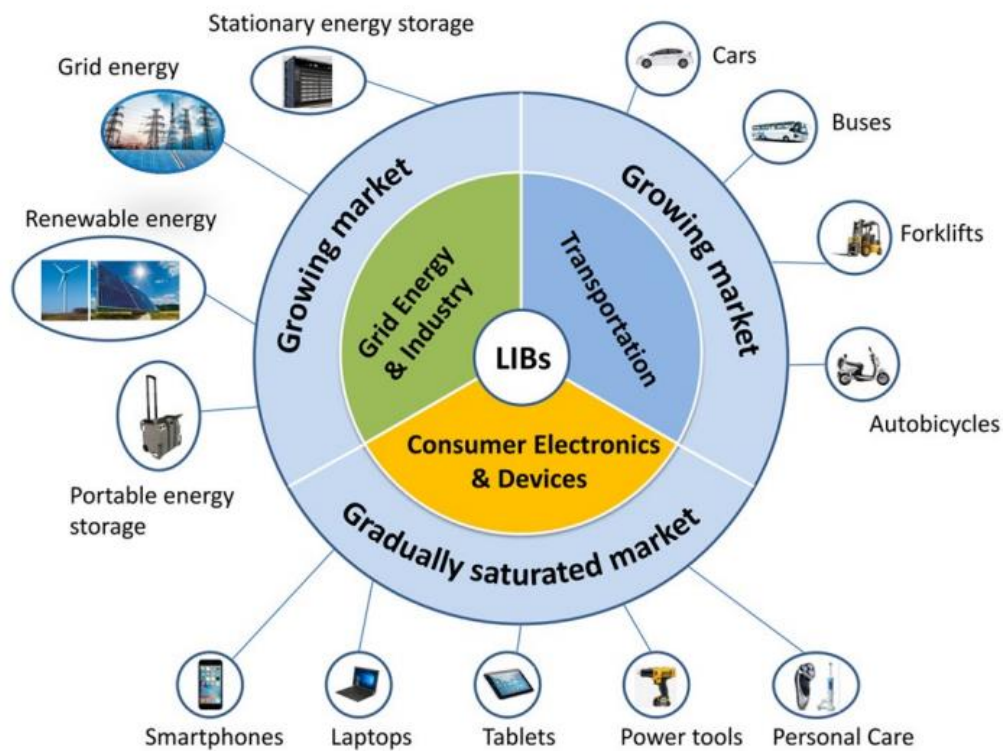


Figure I-6: Three main fields application of LIBs¹⁹.

Nowadays, LIBs gained popularity in electric vehicles (EVs) to substitute conventional petrol and diesel fuels and thereby reduce greenhouse gas (GHG) emissions. **Figure I-7**²⁰ shows global electric vehicles sales from 2011 to 2021. The global EVs demand has been 7 million of EVs in 2021, 107% higher than in 2020. EVs are more sold in China, with approximately 3.5 million *i.e.* 50% of the world's total EVs sales. The EVs manufacturers have adopted different positive electrode material to power their vehicles. **Figure I-8**²¹ shows the type of positive electrode material used by some EVs manufacturers. In 2017-2018, most manufacturers used the NMC 111, except Tesla and BYD which used NCA and LFP positive electrode material, respectively. Then, in 2019-2020, the NMC 111 was replaced by higher Ni content NMC 622. From 2021, Tesla and Volkswagen add LFP to NMC 622 and NCA positive electrode material.

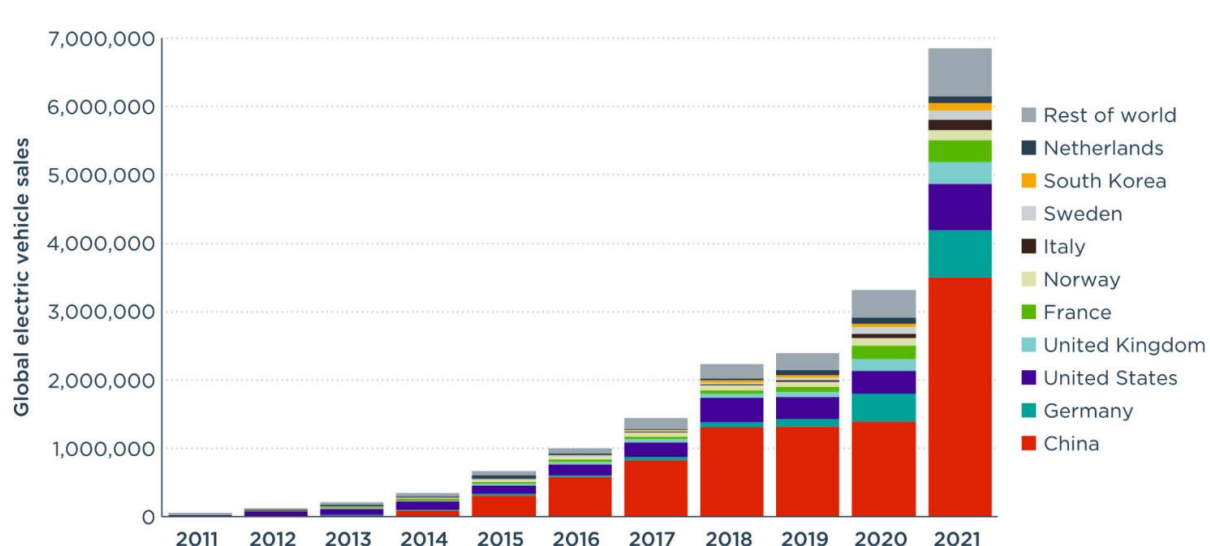


Figure I-7: Global electric vehicles sales from 2011 to 2021²⁰.

	2017	2018	2019	2020	2021	2022	2023
	NMC 111		NMC 532		NMC 622		
	NMC 111		NMC 622				
	NMC 111		NMC 622			+LFP	
	NMC 111	NMC 622					NMC 811
	NMC 532		NMC 622				
	NMC 111		NMC 622				
	NMC 111			NMC 622			
	NCA					NCA + LFP	
	NMC 111			NMC 622		+ LFP	
	NMC 111 ?		NMC 622				
					NCA		
	NMC						
	LFP	LFP	NMC				
	NMC 111			NMC 622			
	NMC 111					NMC532/622?	

Figure I-8: Example of LIBs positive electrode material used by some manufacturers²¹.

I.3 Recycling processes of spent Li-ion battery

The demand of LIBs for EVs growth continuously, resulting in higher demand of positive electrode material. **Figure I-9.a**²¹ shows the demand of LIBs positive electrode materials between 2010 and 2020. According to the graph, the global demand increases significantly from 67000 tons in 2010 to 450 000 tons in 2020 and expected to reach 2 100 000 tons in 2030 (**Figure I-9.b**). In 2010, the commercialized LIBs were mainly based on LCO and NMC type. As LCO positive electrode material type is used in consumer electronic and devices, so its commercialization remained constant, from 2010 to 2020. Unlike, the demand for NMC and NCA positive electrode materials has increased significantly due to their use in transportation. Since 2015, the consumption of LFP positive electrode material has been increased because of their use in EVs and e-bus in China. **Figure I-9.c**, shows the percentage of different positive electrode materials commercialized in 2020. In 2030, it is expected that the layered positive electrode material *i.e.* LCO, NMC, and NCA will reach 70% of global demand as represented in **Figure I-9.d**²¹. Since, LIB lifetime is between 5-10 years, therefore, huge amount of spent LIBs (SLIBs) will be generated in the coming years. The available quantity of SLIBs increases significantly, it was around 200,000 tons in 2020, and it is suspected to reach 1,200,000 in 2030²².

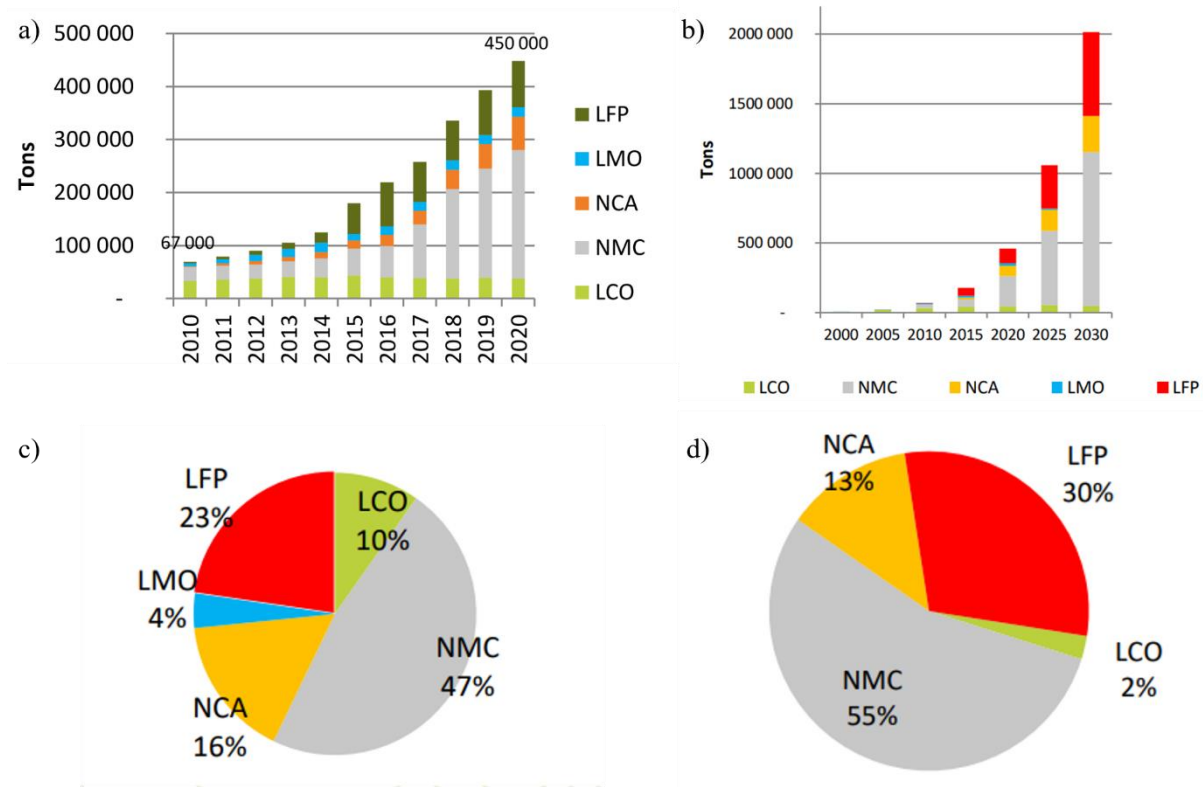


Figure I-9: a) Evolution of the demand for positive electrode material between 2010 and 2020 classified by type²¹. b) Expected evolution of the positive electrode material demand between 2010 and 2020²¹. c) Proportion of each type of positive electrode material marketed in 2020²¹. d) Proportion of type of positive electrode material expected to be in 2030²¹.

The SLIBs are composed of toxic elements Ni, Co, electrolyte, and plastic materials. Therefore, their accumulation endangers human health and lead to the environmental problems. In addition, owing to the large demand, raw materials are depleting. Thereby, the recycling can minimize the impact of this waste. According to European regulations on batteries, the legislation provides for recycling at least 50% of the total mass of lithium ion batteries²³. **Figure I-10** shows the typical composition of LIBs for EVs²⁴, the positive electrode material represents 30% of the total mass of a LIB, the negative electrode represents 17%, and the electrolyte 13%. Thereby, the recycling of positive electrode material representing 30% of total battery mass will allow to reach the recycling objective.

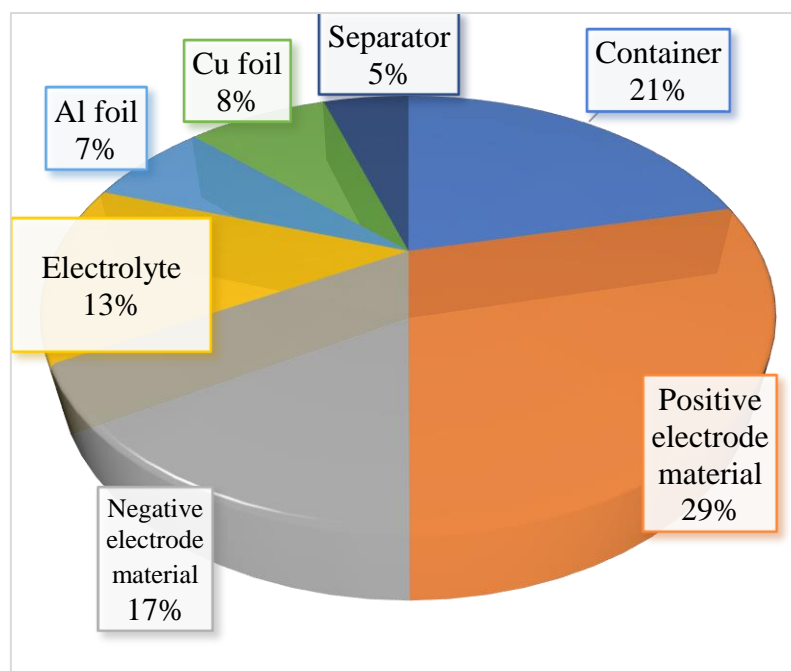


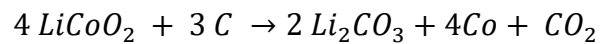
Figure I-10: Typical mass % composition of LIBs of electric vehicle. Note that in this representation the weight percentage of positive electrode and anode material include active material, conductor, and binder.

The complex chemistry of positive electrode materials especially those used for EVs present challenge for LIBs recycling. At present, numerous recycling methods have been demonstrated, such as, pyrometallurgy, hydrometallurgy, direct recycling, and salt conversion. For the later the term “roasting” is commonly used in the literature. On the industrial scale, the pyro- and hydro-metallurgical processes are applied. While, direct recycling process and salt conversion are still under development.

I.3.1 Pyrometallurgical process

The pyrometallurgical process consist of high temperature heating to convert metal oxide into metals or alloys. **Figure I-11** shows schematic representation of pyrometallurgical process²⁵. The SLIBs are melted alone or by adding some reducing agent to help the reduction of metals (**Equation I-4** and **Equation I-5**). After melting, the SiO_2 and CaO slag agents are added to segregate the lithium, the aluminum, and manganese as slag, then the alloys are deposit in the bottom of furnace.²⁶ Thereafter, metal alloys are recovered by hydrometallurgical process. However, lithium and manganese are lost.

Equation I-4:



Equation I-5:

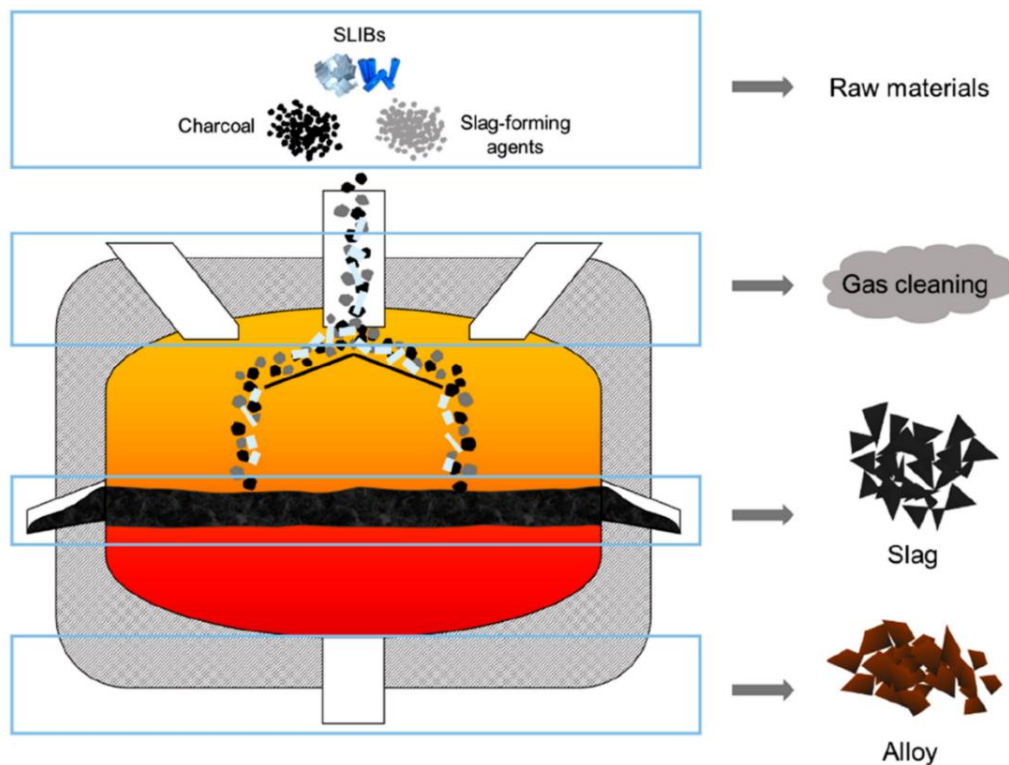
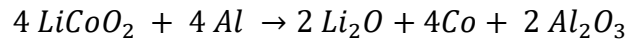


Figure I-11: schematic representation of pyrometallurgical process²⁵.

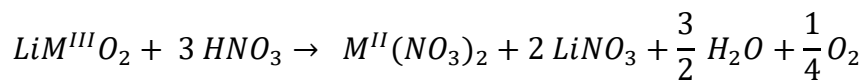
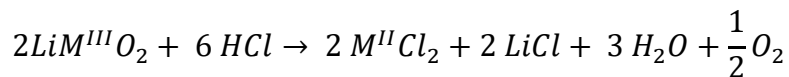
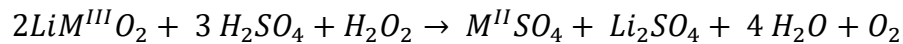
The pyrometallurgical route is easy operation process and the most used to recover cobalt and nickel. However, lithium, manganese and aluminum are lost. In addition, it is high energy consumption and presents environmental drawbacks owing to the production of toxic gases.

I.3.2 Hydrometallurgical process

Hydrometallurgical process is the most selective route to recover material of spent li-ion batteries. It is an aqueous chemistry approach, typically performed at low temperature²⁷. It consists of acid leaching and metals recovery. The aim of leaching step is to dissolve metals

from the positive electrode material in an acidic medium. Thereafter, the dissolved metals are separated through selective chemical reaction to recover target elements e.g. Co, Ni, Li.

The leaching process is usually performed using acid such as H_2SO_4 (2M)²⁸, HCl, HNO_3 ²⁹. Some reducing agent usually H_2O_2 are added in order to convert the metals to their divalent state which are more soluble in solution. The proposed reactions balance for leaching processes using various acids are²⁹:



To improve the leaching rate, the type and concentration of the acid, the reaction temperature, the S/L ratio, and reaction time are optimized³⁰. Sun *et al*³¹ reported the leaching of Li (99%) and Co (99%) by dissolving 50g of $LiCoO_2$ in 1L of H_2SO_4 (2M) -5 vol% of H_2O_2 under 80°C for 1h. Similarly, Machram *et al*³² showed the leaching of Li (93.4%), Co (79.2%), Ni (96.4%), and Mn (84.6%) from mixture positive electrode material using H_2SO_4 (1M) -5 wt% of H_2O_2 with S/L ratio of 50 g/L under heat treatment at 95°C for 4h.

After the leaching of $LiCoO_2$, the cobalt is recovered as oxalate^{33,34}, sulfate²⁸, hydroxide or carbonate³⁵. However, the extraction of lithium is more complex compared to transition metals. In most case, it is recovered as carbonate Li_2CO_3 ³⁴ or as phosphate Li_3PO_4 ³⁶ powders.

As the positive electrode material of LIBs used for EVs contains multiple transition metals Ni, Co, Mn, Al, this increases the complexity of the recovered process. Zou *et al*³⁷ used hydrometallurgical process to recycle mixed positive electrode materials, they performed successive precipitations to recover individual metals, **Figure I-12** shows the separation step of multiple transition metal oxide, the Co, Ni, and Mn with similar proprieties are not separated, but reused to regenerate NMC positive electrode material.

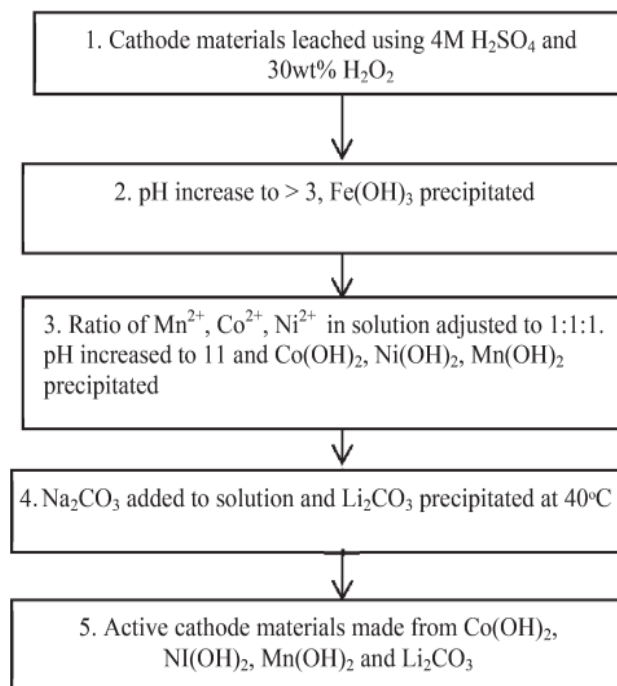


Figure I-12: Hydrometallurgical process for mixed positive electrode material³⁷.

The hydrometallurgical process is a low temperature process, it can be used for mixture of positive electrode materials. However, the big drawback of all hydrometallurgical route is the huge volume of required acid, the cost for effluent treatment, and low aluminum recovery.

I.3.3 Direct recycling

In order to develop new alternative approach to recycle spent LIB, the direct recycling process was proposed. It is based on the re-lithiation of spent LIBs positive electrode material to restore their electrochemical performance.

The direct regeneration of the positive electrode material is performed using a source of lithium that can be either in a solid-state e.g. Li₂CO₃ or liquid state such as LiOH. (i) The solid-state process is based on mixing positive electrode material with Li₂CO₃, thereafter, the positive electrode was re-lithiated by sintering at different time and temperature³⁸. Similarly, Shi *et al.*³⁹ showed the relithiation of NMC material using an eutectic molten salt compound (LiNO₃ and LiOH) which is in solid-state at room temperature and liquid at temperature higher than its melting point. The transition from solid to liquid state leads to relithiation of the material. The liquid regeneration involves the regeneration of positive electrode material using basic solution.

Shi *et al.*³⁸ showed the regeneration of the LiCoO₂ by hydrothermal treatment with annealing approach using LiOH (4M) base solution and annealing temperature around 800°C.

Despite the economic and environmental advantages of the direct recycling process, however, until now it has only been applied at the laboratory scale. Indeed, this method requires specific information on SLIBs such as the delithiation rate. In addition, the degradation of positive electrode material can limit the use of the direct recycling.

To summarize, **Figure I-13** shows a closed-loop recycling of SLIBs and the recovered elements through the pyrometallurgy, the hydrometallurgy, and the direct recycling processes⁴⁰. The pyrometallurgy requires a hydrometallurgical process to provide metal recovery e.g. Co, Ni, and Cu. Nevertheless, the recovery of Li, Mn and Al is almost negligible. Likewise, by the hydrometallurgical process, the Li and Al are not recovered. As reported by United Nation Environment Programme (UNEP) less than 1% of lithium is being recycled², via pyrometallurgy and hydrometallurgical processes. The direct recycling process is much advantageous for the recovery of Li.

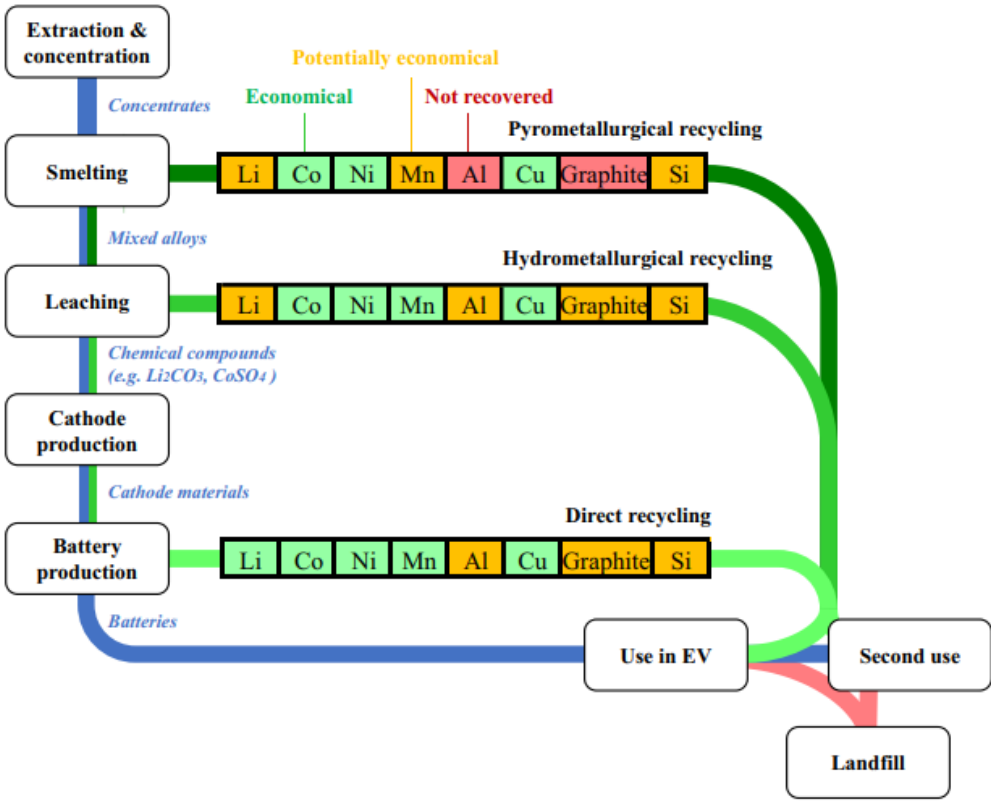


Figure I-13: close loop for LIBs recycling using three different processes, and material recovered from each process⁴⁰.

I.3.4 Alternative recycling process: Deep eutectic solvent

Deep eutectic solvent (DESs) are a class of green solvents, first introduced in 2003 by Abbot⁴¹. The DESs are mixtures of components that are hydrogen bond donors and hydrogen bond acceptor. These solvents present high capability of dissolving common metal oxide and they are biodegradable.

Currently, multiple researches have been demonstrated the efficiency of DESs for dissolving LIBs positive electrode material such as LiCoO_2 and NMC. The DESs act as reducing agent and leaching agent. Their reducing efficiency is mainly related to the presence of an oxygen acceptor in the eutectic solvent, allowing the cleavage of metal-oxide bond⁴². For example, the leaching of LiCoO_2 by choline chloride and ethylene glycol (ChCl:EG) based DES was reported⁴³. The interesting point in this study was that, the reduction of Co (III) in LiCoO_2 to Co (II) as tetrachlorocobaltate (II) anion complex occurs concomitantly with dissolution process. Thus, it was supposed that the dissolution of LiCoO_2 in ChCl:EG involves the simultaneous oxidation of ethylene glycol and reduction of cobalt. The most studies using a DESs leaching agent shown that the average duration of process is high (~12h), making it difficult to achieve a large-scale operation.

I.3.5 Salt conversion approach

The principle of this approach is to convert the positive electrode material LMO into a water-soluble product, through the chemical reaction with an inorganic molten salt. Thereafter, the resulting product was subjected to water leaching. The current process includes chlorination, nitration, and sulfation processes. The chlorination process involves heating the positive electrode material with a chlorination agent e.g. NH_4Cl ^{44,45}. The nitration process is about heating the positive electrode with nitration agent such as HNO_3 ⁴⁶, and the sulfation process is based on the thermal treatment of positive electrode material with sulfation agent e.g. NaHSO_4 . In the present study, we will investigate the sulfation process.

The sulfation process involves the conversion of positive electrode material into sulfate product. The key parameters to achieve this conversion are, the annealing temperature and the molar ratio salt/ transition metal. Wang *et al.*^{47,48} reported the first sulfation of LiCoO_2 using $\text{NaHSO}_4 \cdot \text{H}_2\text{O}$ molten salt at 600°C. They showed that the conversion of Co^{III} into soluble Co^{II}

as sulfate product $\text{Na}_6\text{Co}(\text{SO}_4)_4$ or $\text{Na}_2\text{Co}(\text{SO}_4)$ depends on the molar ratio $\text{NaHSO}_4 \cdot \text{H}_2\text{O} / \text{LiCoO}_2$. However, they also found the formation of Co_3O_4 due to the release of SO_3 . To avoid SO_3 emissions, Lin *et al.*^{49,50} used sulfuric acid to convert LiCoO_2 ⁴³ and NMC⁴⁴ into sulfate products. They conclude that, the sulfation of LiCoO_2 with H_2SO_4 (2:1) at 800°C results to the formation of Li_2SO_4 and Co_3O_4 . Thereafter, Tang *et al.*⁵¹ adopted low temperature sulfation to recover 98.5% of valuable metals from NMC 622 material with $(\text{NH}_4)_2\text{SO}_4$ molten salt. The above-mentioned studies have confirmed the ability of molten salt to convert lithium transition metal oxides LMO into salt under a solid-state reaction, thereby providing an alternative approach to the recycling of positive electrode material of SLIBs with molten salt.

To understand the mechanisms involved during the sulfation of LMO, the XRD, TGA, DSC, and XPS measurements were carried out. The process consists of heating the mixture of LMO and molten salt at different temperatures then the resulting products are analyzed. Yang *et al.*⁴⁶ concluded that the conversion of LMO into sulfate product resulted from the reaction of LMO with the SO_3 formed by decomposition of the salt. However, considering the experimental conditions, this mechanism is not acceptable. Since if we consider an air atmosphere, the released SO_x will be evacuated, preventing the conversion of LMO, whereas some studies showed the sulfation of LMO under air. Thereafter, to better understand the mechanism, Chen *et al.*⁴⁵ have performed *in situ* XRD analysis to investigate the sulfation of NMC811 using $\text{NaHSO}_4 \cdot \text{H}_2\text{O}$ molten salt. By *in situ* XRD they observed that “Li was first extracted from the layered structure, while the other elements (Ni, Co, and Mn) existed in the form of polyoxometalates and a trace of $\text{Na}_2\text{Me}(\text{SO}_4)_2$ and $\text{Na}_6\text{Me}(\text{SO}_4)_4$ (Me= Ni and Co)”⁴⁵. Without in-depth analysis, they confirmed that the SO_3 enables the conversion of LMO.

I.4 Conclusion

As the quantity of spent Li-ion batteries increases, recycling becomes essential. Besides the currently used processes of pyrometallurgy, hydrometallurgy and direct recycling, a new approach consisting on the use of molten salts has appeared. It is based on the conversion of the positive electrode into a water-soluble salt, followed by water leaching to recover the targeted elements. Sulfation is kind of salt conversion. It involves the conversion of LMO into sulfates products. Several studies have demonstrated that this approach closes the recycling loop. However, there is still a lack of fundamental understanding of the mechanism involved upon the sulfation of LMO.


The aim of our work, is to deeply understand the reaction mechanism involved during the conversion of transition metal oxide (LMO) into water soluble sulfate-based product. We selected two different salts, hydrogen potassium KHSO_4 and potassium pyrosulfate $\text{K}_2\text{S}_2\text{O}_7$ to convert positive electrode materials of LIBs into soluble sulfate products. In chapter II, the sulfation of LiCoO_2 using KHSO_4 ($T_{\text{mp}}= 200^\circ\text{C}$)⁴ will be investigated in further details, using thermogravimetry differential scanning calorimetry (DSC), variable- temperature XRD, and X-rays absorption spectroscopy (XAS). Thereafter, in chapter III, the sulfation of LiCoO_2 with proton free molten salt $\text{K}_2\text{S}_2\text{O}_7$ ($T_{\text{mp}}= 400^\circ\text{C}$)⁵ will be investigated. To conclude, the results obtained for both salts will be compared.

Chapter II. Investigation of the sulfation conversion of lithiated transition metal oxide using potassium hydrogensulfate

II.1 Introduction

As introduced in the previous chapter, the recycling of spent li-ion batteries is mandatory to overcome the environmental and economic problems encountered due to their accumulation. Several recycling processes have been explored such as pyrometallurgy, hydrometallurgy, direct recycling, and salt conversion. The latter, consists on the conversion of positive electrode material LMO (M= Co, Ni, Mn, and Al) into salt products. The process involves a solid-state reaction between LMO and molten salt. Sulfation is one of the categories of salt conversion. The first sulfation process was introduced by Wang *et al.* in 2016⁴⁷. They showed that reaction parameters such as temperature and molar ratio molten salt/LMO influence the conversion rate. These parameters are well defined for different sulfate salts e.g. NaHSO₄⁴⁷, (NH₄)₂SO₄⁵¹. However, the conversion mechanism involved during the reaction is not deeply understood.

The main goal of this chapter is to understand deeply the conversion mechanism occurred during the solid-state reaction of the positive electrode material LiCoO₂ and potassium hydrogensulfate (KHSO₄) molten salt. The sulfation process includes a solid-state reaction between LiCoO₂ and KHSO₄ yielding the langbeinite K₂M₂(SO₄)₃, KLiSO₄, and K₂SO₄. To carry out this study, the outline below was adopted.

- 
- 1- Determination of the reaction parameters
 - 2- Extension to NMC and NCA electrode materials
 - 3- Investigation of reaction mechanism involved during the sulfation of LiCoO₂, based on *in situ* thermodiffraction, X-ray spectroscopy analyses and DFT calculations.

II.2 Reaction parameters

II.2.1 Reaction stoichiometry

To determine the reactant stoichiometry allowing the complete conversion of oxide to sulfates (sulfation), various LiCoO₂: KHSO₄ [1: *n*] mixtures from *n*=1 to *n*=3 were subjected to heat treatment at 400°C under air. After the heat treatment, the recovered products were analyzed by X-ray diffraction analysis (XRD). **Figure II-1** shows the evolution of XRD patterns as function of *n* KHSO₄ quantity. For LiCoO₂: KHSO₄ [1: 1], the pattern was indexed with K₂Co₂(SO₄)₃ (S.G: P 2₁ 3)⁵⁴, KLiSO₄ (S.G: P 6₃)⁵⁵, K₂SO₄ (S.G: P n a m)⁵⁶, Co₃(SO₄)₂(OH)₂.2H₂O (S.G: P b c m)⁵⁷ and LiCoO₂ layered structure⁵⁸. The LiCoO₂ phase is characterized by the main peak at $2\theta = 18.9^\circ$ assigned to (003) plan. By increasing KHSO₄ quantity (Patterns [1: 1.5] and [1: 2]), the intensity of the (003) plan decreases. In addition, the detection of Co₃O₄ (SG: F d -3 m, peak at $2\theta = 19.1^\circ$)⁵⁹ *i.e.*, Co^{II}Co^{III}₂O₄, indicates an incomplete sulfation. Consequently, the ratio KHSO₄/ LiCoO₂ was set to 3 yielding a complete conversion of oxide to sulfate-based products: K₂Co₂(SO₄)₃, KLiSO₄, K₂SO₄.

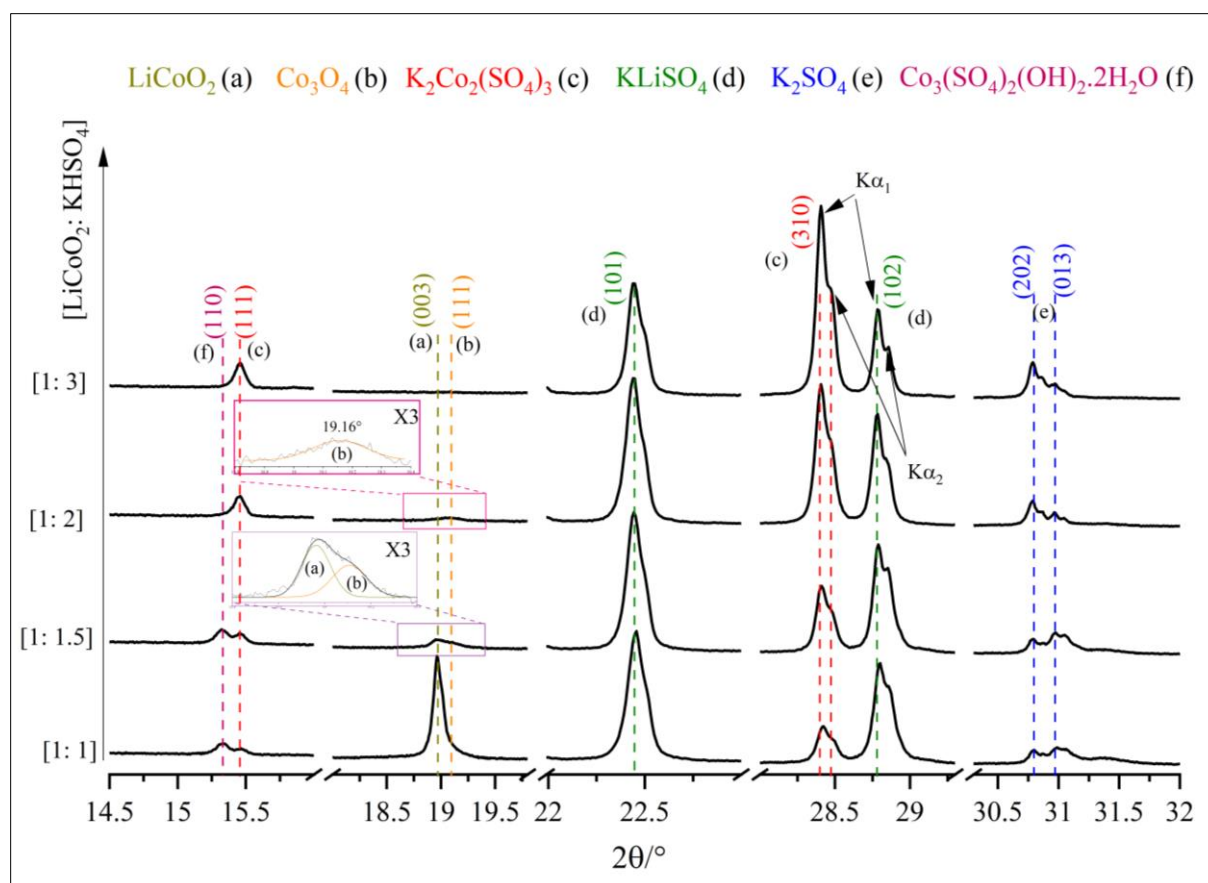


Figure II-1: Evolution of the XRD patterns of LiCoO₂: KHSO₄ [1: n] as a function of n.

II.2.2 Effect of the temperature

To investigate the effect of temperature on the sulfation reaction, solid-state LiCoO₂: KHSO₄ [1: 3] mixtures were heated at 100°C, 200°C, 300°C and 400°C. The colors of the different samples (**Figure II-2**) vary from grey at room temperature to pink at 400°C, which indicate clearly the impact of the temperature on the reactivity. The pink color refers to the formation of Co²⁺ ions in an octahedral configuration⁶⁰. **Figure II-2** shows the evolution of XRD patterns as function of the temperature. Firstly, the obtained product at 100°C contains LiCoO₂ and KHSO₄ phases, showing that, the sulfation reaction does not occurred. At 200°C, the XRD pattern shows the formation of K₄LiH₃(SO₄)₄ (tetragonal, S.G: P4₁)⁶¹, a delithiated phase Li_{0.68}CoO₂, Co₃(SO₄)₂(OH)₂.2H₂O, K₂Co₂(SO₄)₃ and the unreacted LiCoO₂ and KHSO₄. By increasing the temperature to 300°C, the XRD pattern was indexed with K₂Co₂(SO₄)₃, KLiSO₄, K₂Co₂(SO₄)₃, Co₃(SO₄)₂(OH)₂.2H₂O and Co₃O₄. Therefore, the heat treatment at 200°C and 300°C cannot fully convert LiCoO₂ into sulfate-based products. Finally, at 400°C, the

diffraction peaks of LiCoO_2 and Co_3O_4 disappear, thus, the XRD pattern was indexed by $\text{K}_2\text{Co}_2(\text{SO}_4)_3$, KLiSO_4 and K_2SO_4 , consistent with the total sulfation of LiCoO_2 .

By studying the effect of the temperature, some pertinent points related to the reaction mechanism can be underlined:

- The formation of $\text{K}_4\text{LiH}_3(\text{SO}_4)_4$ suggesting that Li^+ ions are de-intercalated from LiCoO_2 yielding a delithiated $\text{H}_x\text{Li}_{1-x}\text{CoO}_2$, where protons are coming from KHSO_4 to compensate the charge induced by lithium removal.
- The mobility of H^+ coming from KHSO_4 is also confirmed by the formation of hydroxide-sulfate compound $\text{Co}_3(\text{SO}_4)_2(\text{OH})_2 \cdot 2\text{H}_2\text{O}$.

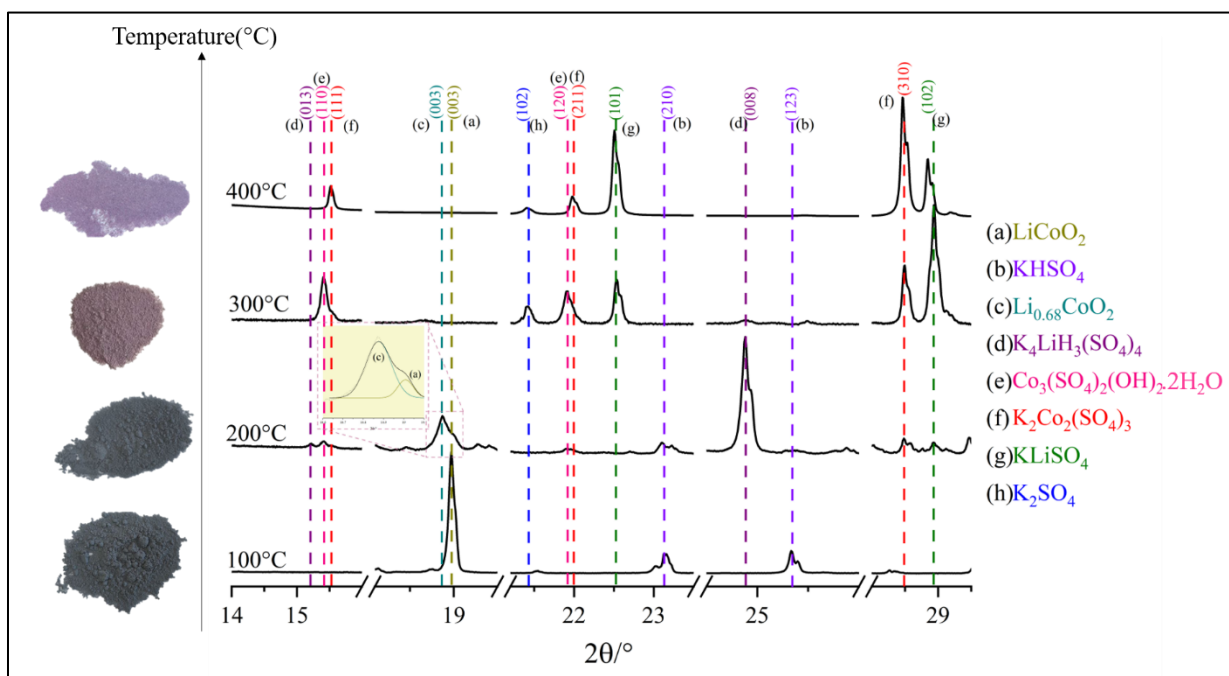


Figure II-2: Evolution of XRD patterns of LiCoO_2 : KHSO_4 [1: 3] mixtures as a function of the heat treatment temperature.

II.2.3 Effect of the atmosphere

The effect of the atmosphere on the sulfation reaction was studied by heating LiCoO_2 : KHSO_4 [1: 3] mixture at 400°C (wherein, the conversion is total) under argon and under vacuum atmospheres. The recovered product under vacuum is black while under argon it is pinkish (represented inside **Figure II-3**), anticipating that the vacuum atmosphere hampers the

completion of the sulfation process. **Figure II-3.a**, and **Figure II-3.b** show the Profile Matching of XRD patterns of the obtained products under argon and vacuum atmospheres, respectively. Under argon, the XRD pattern was indexed with $\text{K}_2\text{Co}_2(\text{SO}_4)_3$, KLiSO_4 and K_2SO_4 , similar to that obtained during the heat treatment under air. This reveals that, the argon does not impact the reactivity. Nevertheless, the XRD pattern of $\text{LiCoO}_2: \text{KHSO}_4$ [1 :3] heat treated under vacuum (**Figure II-3.b**) was indexed with $\text{K}_2\text{Co}_2(\text{SO}_4)_3$, KLiSO_4 , $\text{K}_2\text{S}_2\text{O}_7$ (S.G : C2/c)⁶², $\text{Co}_3(\text{SO}_4)_2(\text{OH})_2 \cdot 2\text{H}_2\text{O}$ (S.G: P b c m)⁵⁷, and Co_3O_4 . It confirms that vacuum prevent the sulfation reaction, also, the formed product is less crystallized ($\chi^2 = 11.3$). The cell parameters obtained during refinement are listed in **Table II-1**, they are close to those published in literature⁵⁴⁻⁵⁷, confirming good attribution of peaks. Under vacuum atmosphere, the presence of $\text{K}_2\text{S}_2\text{O}_7$ can be explained by the dehydration of KHSO_4 according to **Equation II-1**, modifying the reactivity pathway resulting in an incomplete sulfation. The release of H_2O molecules seems to be determinantal to the sulfation reaction, further highlighted the importance of H^+ in the reaction mechanism.

Equation II-1:

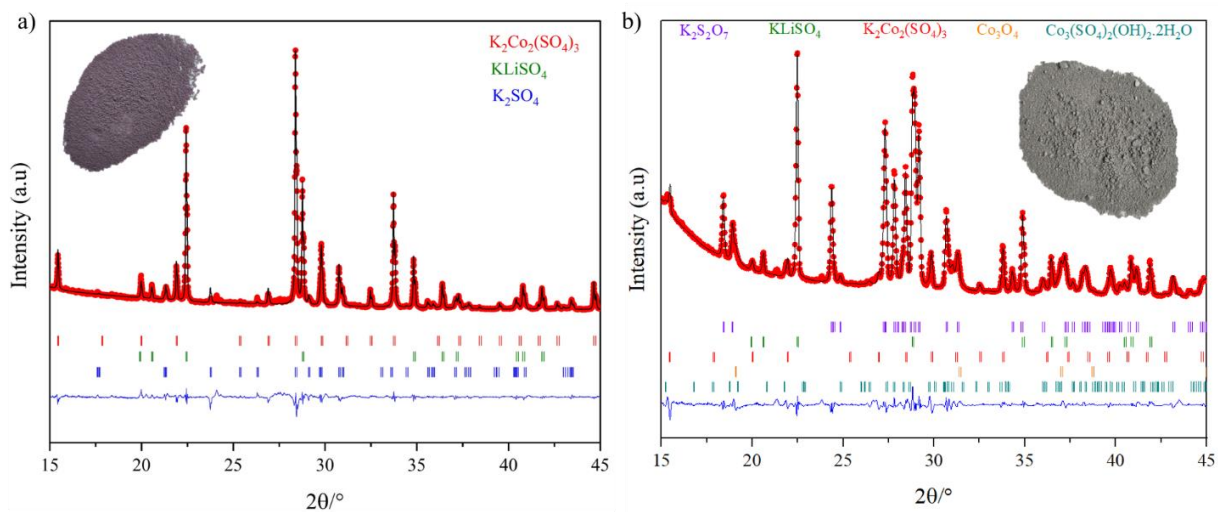


Figure II-3: Profile matching refinements of the XRD patterns of $\text{LiCoO}_2: \text{KHSO}_4$ [1: 3] treated at 400°C (a) under Argon (b) under vacuum atmosphere.

Table II-1: Results of refinements of the obtained product after the heat treatment of LiCoO₂: KHSO₄ [1: 3] under argon and vacuum atmosphere.

Atmosphere	phase	Cell parameters			X ²
		a (Å)	b (Å)	c (Å)	
Argon	K ₂ Co ₂ (SO ₄) ₃	9.9348(3)	9.9348(3)	9.9348(3)	9.14
	KLiSO ₄	5.1482(2)	5.1482(2)	8.632 (5)	
	K ₂ SO ₄	7.487(5)	10.0804(6)	5.7754(4)	
Vacuum	K ₂ Co ₂ (SO ₄) ₃	9.9224 (3)	9.9224 (3)	9.9224 (3)	11.3
	KLiSO ₄	5.1409(2)	5.1409(2)	8.6200(5)	
	K ₂ S ₂ O ₇	12.3545(6)	7.3058(3)	7.2818(3)	
	Co ₃ O ₄	8.0545 (4)	8.0545 (4)	8.0545 (4)	
	Co ₃ (SO ₄) ₂ (OH) ₂ .2H ₂ O	7.1657(9)	9.9394(8)	12.6029(9)	

II.3 Identification of the sulfation equation

Thereafter, we will focus on the establishment of the sulfation equation of LiCoO₂: KHSO₄ [1: 3] heat treated at 400°C under air. The equation will be established by combining, quantitative-phase analysis determined from Rietveld refinement of XRD data and thermogravimetric analysis coupled with mass spectrometry (TGA-MS) performed with the collaboration of LRCS (Matthieu COURTY).

The quantitative-phase analysis was performed by refining the XRD pattern of LiCoO₂: KHSO₄ [1: 3] with Rietveld refinement. The fit was performed using the Thompson-Cox-Hastings pseudo-Voigt function with three-phases refinement: K₂Co₂(SO₄)₄, KLiSO₄ and K₂SO₄ phases. **Figure II-4-a** shows a good agreement between the observed XRD pattern (Y_{obs}) and the theoretical pattern (Y_{calc}). All peaks are assigned, confirming a complete conversion of LiCoO₂ into sulfate-based products. **Table II-2** gathers the reliability parameters (χ² and Bragg R-factor), cell parameters and mass percentage of each phase and structural parameters. Despite the difficulty on the refining of minor phase K₂SO₄ (Bragg R-factor equal to 18%) the overall reliability parameter χ² = 4.69 and Bragg R-factor of K₂Co₂(SO₄)₄ and KLiSO₄ (7.61% and 7% respectively) are lower indicating a suitable refinement. The values of the lattice parameters are very close to those published in the literature⁵⁴⁻⁵⁶. However, the quantitative results can be underrated, especially for K₂Co₂(SO₄)₄ and K₂SO₄ because of the difference of the intensity

between experimental and calculated peaks with $Y_{\text{calc}} < Y_{\text{obs}}$ as observed on the peak framed in Figure II-4, corresponding to the main (130) line of $\text{K}_2\text{Co}_2(\text{SO}_4)_4$.

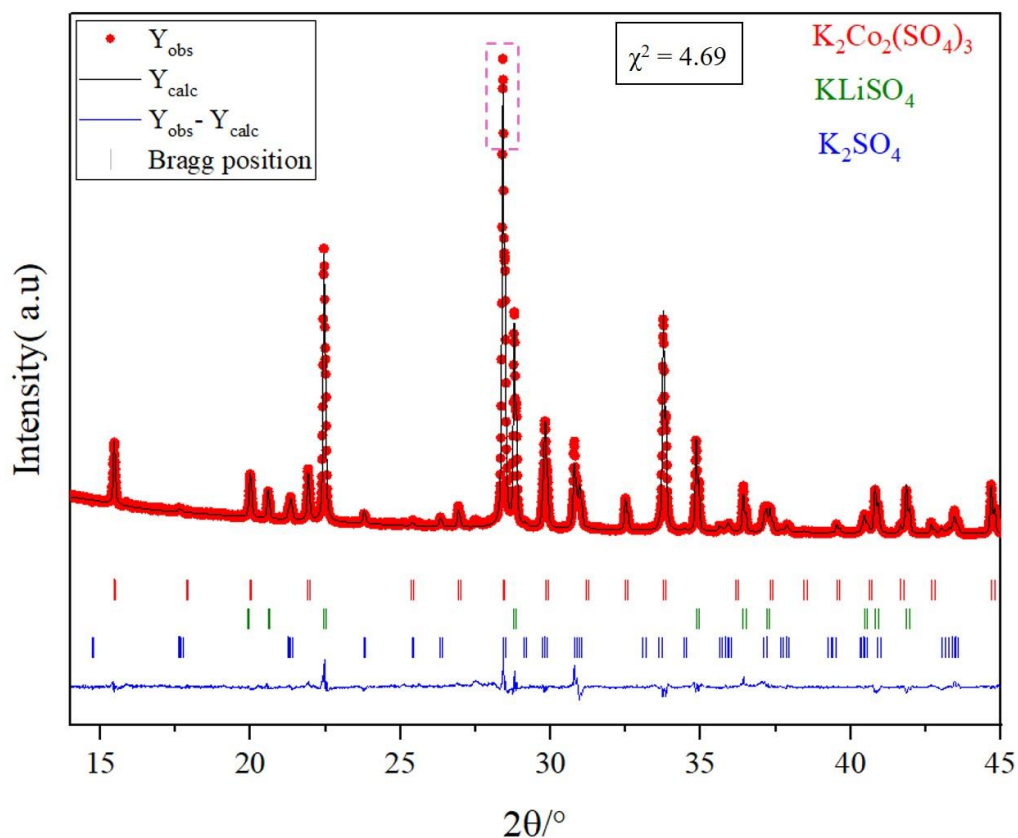


Figure II-4: a) Rietveld refinement of XRD pattern of $\text{LiCoO}_2 : \text{KHSO}_4$ [1: 3] after heat treatment at 400°C under air.

Table II-2: a) Results of the Rietveld refinement of the XRD pattern of $\text{LiCoO}_2 : \text{KHSO}_4$ [1: 3] after heat treatment at 400°C under air.

Phases	a (Å)	b (Å)	c (Å)	Bragg R-factor%	wt. %
$\text{K}_2\text{Co}_2(\text{SO}_4)_3$	9.92590(5)	9.92590(5)	9.92590(5)	7.61	48.67(15)
KLiSO_4	5.14375(3)	5.14375(3)	8.62380(7)	7.00	33.04(13)
K_2SO_4	5.77(14)	10.070(75)	7.47970(14)	18.2	18 (1)

Table II-2: b) Structural parameters for LiCoO₂: KHSO₄ [1: 3] after heat treatment at 400°C obtained from Rietveld refinement of XRD pattern.

Phase	Atoms	x	y	z	B iso	occ	Wyckof f position
K ₂ Co ₂ (SO ₄) ₃	Co1	0.3334(9)	0.3334 (9)	0.3334(9)	0.95(14)	0.333	4 a
	Co2	0.5946(8)	0.5946(8)	0.5946 (8)	0.845	0.333	4 a
	K3	0.814(14)	0.814(14)	0.814(14)	1.17(2)	0.333	4 a
	K4	0.0486 (13)	0.0486(13)	0.0486(13)	1.879	0.333	4 a
	S5	0.2162(13)	0.376 (2)	0.0192(17)	0.692	1	12 b
	O6	0.310(4)	0.276 (3)	0.9528(36)	2.17(3)	1	12 b
	O7	0.084(4)	0.337 (4)	0.0030(3)	1.808	1	12 b
	O8	0.241(3)	0.491 (5)	0.948 (5)	1.70(4)	1	12 b
	O9	0.252(3)	0.403 (4)	0.158 (4)	2.59(4)	1	12 b
KLiSO ₄	O1	0.5958(2)	0.938 (16)	0.947 (9)	1	1	6 c
	S2	0.33333	0.66667	0.892 (7)	1	0.333	2 b
	Li3	0.33333	0.66667	0.513 (0)	1	0.333	2 b
	K4	0.00000	0.00000	0.183 (9)	1	0.333	2 a
	O5	0.33333	0.66667	0.730 (8)	1	0.333	2 b
K ₂ SO ₄	K1	0.2500	0.088 (2)	0.171(18)	1.394	0.5	4 c
	K2	0.2500	0.7878(15)	0.489(3)	1.229	0.5	4 c
	S3	0.2500	0.421(3)	0.239(2)	0.781	0.5	4 c
	O4	0.2500	0.41620	0.03680	2.076	0.5	4 c
	O5	0.2500	0.55850	0.29760	1.537	0.5	4 c
	O6	0.0412	0.35220	0.30170	1.750	1	8 d

Thermogravimetric coupled with mass spectrometry (TGA-MS) analysis was performed on LiCoO_2 : KHSO_4 [1: 3] mixture, which was heated from 40°C to 500°C with a heating rate of $5^\circ\text{C}/\text{min}$. The obtained TGA thermogram (**Figure II-5.a**) shows a large mass loss from 190°C to 500°C (-11.8%). To interpret the result, this figure has been divided in two parts: the first one extends from 40°C to 400°C and the second one from 400 to 500°C . In the first part *i.e.* 40°C to 400°C , the quasi-multiple ion detection (QMDI) indicate the release of H_2O^+ ($m/z = 18$) and O_2^+ ($m/z = 32$). The departure of H_2O is spreaded over a large range of temperature from 190 to 400°C , while the departure of oxygen is marked by a fine and intense peak at 350°C . Comparing this result with the thermal behavior of KHSO_4 (**Figure II-5.b**) which show only departure of water, we suggest that the departure of O_2 can be from the oxidation of the oxide ions of LiCoO_2 . In the second part, from 400°C to 500°C , the release of SO_2^+ ($m/z = 64$) was detected. The departure of SO_2 causes a deficit of sulfate which induces an incomplete sulfation of LiCoO_2 . Thus, the control of temperature is mandatory to fully convert LiCoO_2 into sulfate-based products.

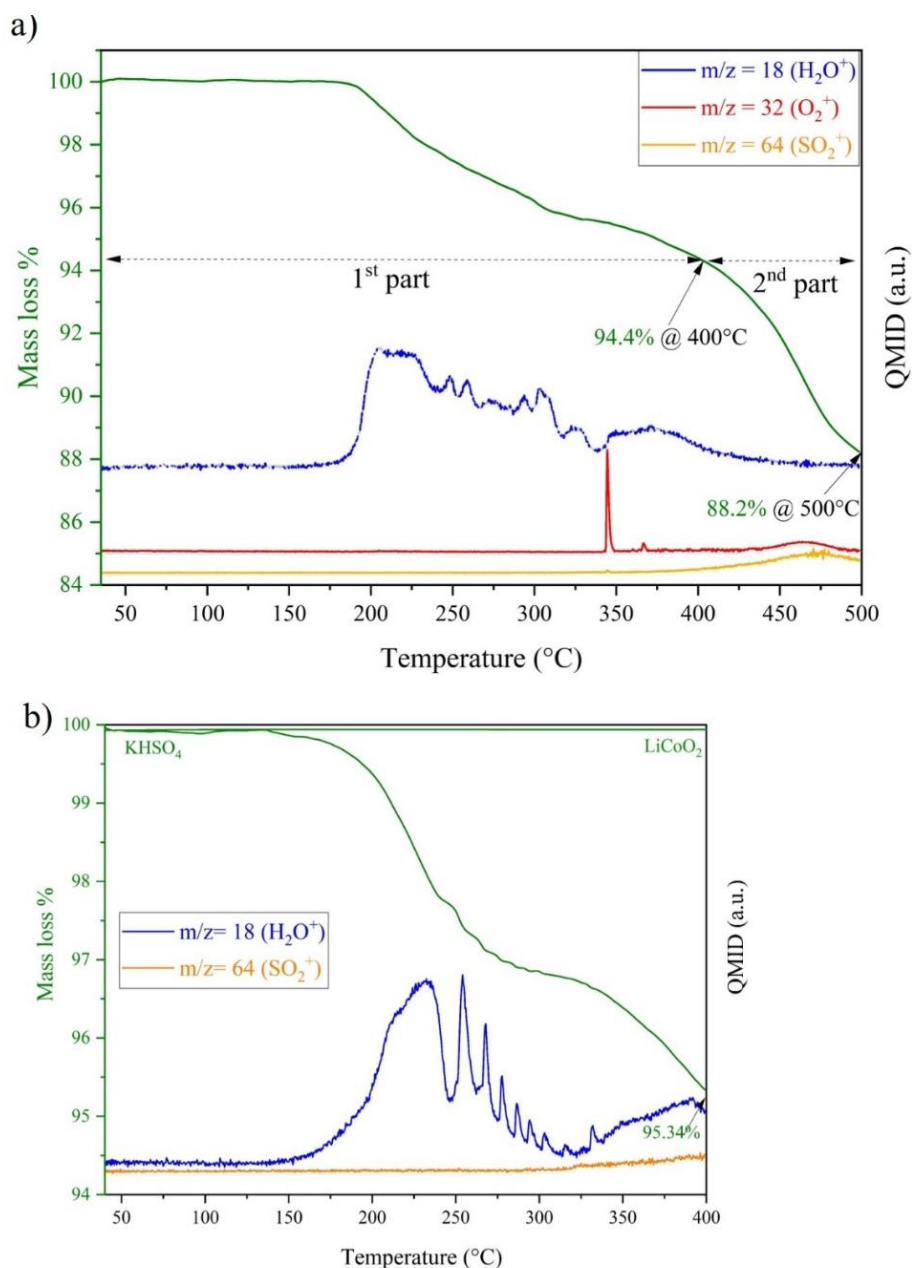
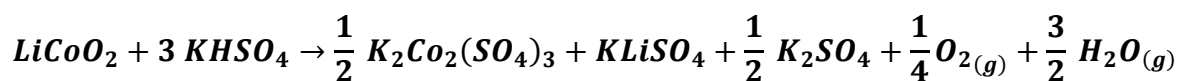


Figure II-5: a) TGA performed on LiCoO₂: KHSO₄ [1:3] heating from 40°C to 500°C. Green line represents TGA analysis, H₂O gas lost blue, O₂ (red), SO₂ (yellow). b) TGA analysis of LiCoO₂ pristine and KHSO₄ pristine heated from 40°C to 400°C.

According to the quantitative-phases analysis determined by Rietveld refinement and the departure of H₂O and O₂, the overall reaction can be written as:

Equation II-2:



Using the **Equation II-2**, we have calculated the theoretical weighted percentage of each phase. **Table II-3** show a good agreement between the calculated and experimental weight percentages determined by Rietveld refinement, confirming the reaction equation. For $K_2Co_2(SO_4)_3$, the theoretical *wt%*. is a little bit higher than the experimental one, which can be due the above mentioned difference in the intensity between experimental and calculated peak as observed on the pic framed in **Figure II-4**.

Table II-3: Experimental and calculated weight % of each phase identified by XRD analysis

	Experimental <i>wt%</i>	Calculated <i>wt%</i>
$K_2Co_2(SO_4)_3$	48.67(15)	51.37
$KLiSO_4$	33.04(13)	30.15
K_2SO_4	18 (1)	18.49

To conclude, to fully convert $LiCoO_2$ into the water-soluble sulfate products it is necessary to: (i) set the stoichiometry $LiCoO_2: KHSO_4$ to [1:3] (ii) use air or argon atmospheres (iii) heat treat the mixture at 400°C. The results of ATG-MS showed that during the thermal treatment, a departure of H_2O and O_2 were detected. The departure of H_2O is due to the decomposition of $KHSO_4$ and the departure of O_2 is due to the decomposition of $LiCoO_2$ during its reactivity with $KHSO_4$. The O_2 result from the oxidation of the O^{2-} ions of the $LiCoO_2$ phase. This oxidation is compensated by the reduction of cobalt III to cobalt II. *i.e.* the formation of the reduced compound $K_2Co_2(SO_4)_3$.

II.4 Extension to NMC and NCA layered positive electrode materials

II.4.1 Crystal structure of Langbeinite $K_2M_2(SO_4)_3$

The sulfation reaction of $LiCoO_2$ leads to the formation of $K_2Co_2(SO_4)_3$, which adopt the Langbeinite type-mineral structure. This family of mineral exist with various metals, $M^{II}=Mg, Ca, Mn, Co, Ni, Zn, Cd, Fe$ ⁶³⁻⁶⁹. It has a cubic symmetry and the space group $P 2_1 3$. The structure (**Figure II-6.a**) is built from isolated MO_6 octahedra (blue) that are connected to six SO_4 tetrahedra (yellow) via their oxygen vertices (red spheres). The K atoms are located in the

large cavities of the $M_2(SO_4)_3$ framework. Speer *et al.*,⁶³ discussed the structural dependence on the nature of M and found that it is only related to the degree of distortion of the MO_6 polyhedra. We confirmed this trend by plotting the cubic unit cell parameter as a function of the M ionic radius and found a linear correlation (**Figure II-6.b**). Hence, we anticipated that whatever the chemical composition of the positive electrode materials, the transition metals of interest (Ni, Co, Mn) can be stabilized in this structure (see next section).

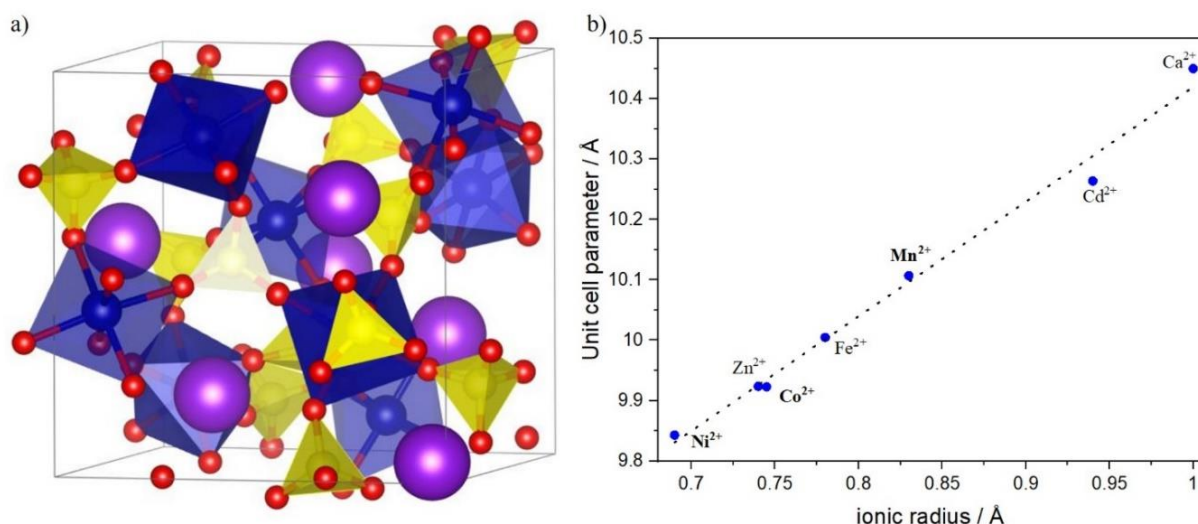


Figure II-6: a) Cubic structure of $K_2M_2(SO_4)_3$ where red and purple spheres refer to oxygen and potassium atoms, respectively. Blue octahedra and yellow tetrahedra refer to MO_6 and SO_4 , respectively. b) Cubic unit cell parameter versus ionic radius of M^{II} .

II.4.2 Extension to NMC and NCA positive electrode materials

To confirm the possible extension of sulfation process to more complex positive electrode materials, we investigated the reaction of $KHSO_4$ with NMC ($LiNi_{1/3}Mn_{1/3}Co_{1/3}O_2$) and NCA ($LiNi_{0.82}Co_{0.15}Al_{0.03}O_2$).

II.4.2.1 Extension to NMC ($LiNi_{1/3}Mn_{1/3}Co_{1/3}O_2$)

To study the extension of the sulfation process into NMC positive electrode material, its reactivity with $KHSO_4$ was investigated. Based on the sulfation conditions determined for $LiCoO_2$ positive electrode material (ratio, temperature and atmosphere), NMC: $KHSO_4$ [1:3] mixture was heat treated at $400^\circ C$ under air and analyzed by XRD analysis. **Figure II-7.a** shows the XRD patterns of sulfation product. All the XRD peaks were indexed with $KLiSO_4$, K_2SO_4

and importantly one single cubic $K_2M_2(SO_4)_3$ phase. This latter suggests that Co, Ni, and Mn form a solid solution with the composition $K_2(Ni_{1/3}Mn_{1/3}Co_{1/3})_2(SO_4)_3$. To ascertain this, three studies were performed. (i) the comparison between the 2θ positions of the XRD peaks of the sulfation product and those of the theoretical $K_2Ni_2(SO_4)_3$, $K_2Co_2(SO_4)_3$ or $K_2Mn_2(SO_4)_3$ phases. (ii) Rietveld refinements of the XRD pattern of sulfation product. (iii) x-ray energy dispersive spectroscopy analysis.

Figure II-7.b shows the XRD of $K_2M_2(SO_4)_3$ obtained through sulfation and the XRD of $K_2Ni_2(SO_4)_3$, $K_2Co_2(SO_4)_3$ or $K_2Mn_2(SO_4)_3$ taken from the inorganic crystal structure database (ICSD). The peaks of $K_2M_2(SO_4)_3$ locate at $2\theta = 15.35^\circ$, 19.86° and 28.27° lies within 2θ of the XRD of Ni, Co and Mn-based products, suggesting the concomitant stabilization of Ni, Co and Mn within the cationic sublattice, and therefore the formation of the solid solution $K_2(Ni_{1/3}Co_{1/3}Mn_{1/3})_2(SO_4)_3$.

The Rietveld refinement of the XRD pattern was performed using the Thompson-Cox-Hastings pseudo-Voigt function with three-phases refinement: $K_2M_2(SO_4)_3$ (note that Co, Ni and Mn display similar x-ray scattering ability and therefore cannot be distinguished), $KLiSO_4$ and K_2SO_4 phases. **Figure II-7.c** shows the Rietveld refinement of the XRD pattern. with a good agreement between the calculated and the experimental patterns. The obtained χ^2 , Bragg R-factors % and cell parameters are listed in Table II-4. The cell parameters of $KLiSO_4$ and K_2SO_4 are close to those found in the literature^{55,56,67}. For the langbeinite $K_2M_2(SO_4)_3$ the calculated cubic cell parameter ($a = 9.9597(2) \text{ \AA}$) is rather higher than theoretical parameter of $K_2Co_2(SO_4)_3$ ($a = 9.9228 \text{ \AA}$). It can be explained by the presence of Mn with higher ionic radius (0.83 \AA) compared to cobalt (0.745 \AA). To confirm the presence of the different cations in the 4a site of the langbeinite type structure, we plotted the unit cell parameters determined by Rietveld analysis as a function of the ionic radius of Ni^{2+} , Co^{2+} and Mn^{2+} (**Figure II-7.d**). The cubic unit cell parameter value 9.9593 \AA lies within $K_2Ni_2(SO_4)_3$ and $K_2Mn_2(SO_4)_3$ indicating the stabilization of Ni, Co and Mn within the cubic structure with an estimated composition $K_2(Ni_{1/3}Co_{1/3}Mn_{1/3})_2(SO_4)_3$.

Moreover, the x-ray energy dispersive spectroscopy (EDS) was performed to confirm the composition of the Langbeinite $K_2(Ni_{1/3}Co_{1/3}Mn_{1/3})_2(SO_4)_3$. **Figure II-7.e** and **Figure II-7.f** represent the EDS spectra of NMC pristine and NMC: $KHSO_4$ heat treated at 400°C under air. The atomic percentages of Co, Ni and Mn are listed inside **Figure II-7.e** and **f**. The **Table II-5** shows the ratio of $\frac{Co}{Ni}$ and $\frac{Mn}{Ni}$ determined from EDS result on the same crystal and that

calculated for typical $K_2(Ni_{1/3}Mn_{1/3}Co_{1/3})_2(SO_4)_3$, the ratio value are similar confirming the stabilization of $K_2(Ni_{1/3}Mn_{1/3}Co_{1/3})_2(SO_4)_3$.

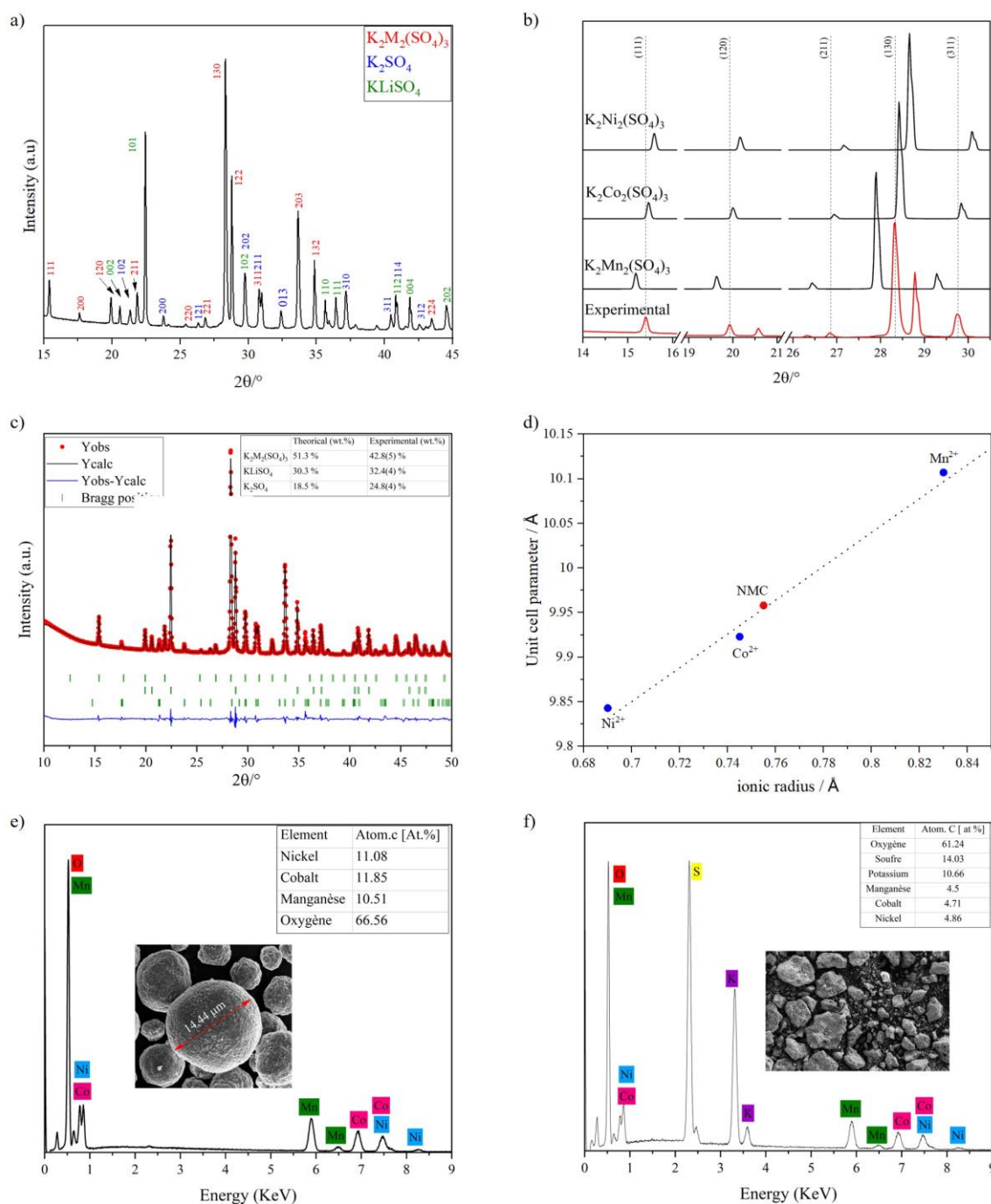


Figure II-7: a) XRD pattern of NMC: KHSO₄ [1: 3] heat treated at 400°C under air. b) XRD peaks of K₂M₂(SO₄)₃ after heat treatment of NMC with KHSO₄, compared to that of K₂Mn₂(SO₄)₃, K₂Co₂(SO₄)₃ and K₂Ni₂(SO₄)₃. c) Rietveld refinements of XRD pattern of NMC after heat treatment with KHSO₄. d) Unit cell parameters of K₂Ni₂(SO₄)₃, K₂Co₂(SO₄)₃, K₂Mn₂(SO₄)₃ and NMC treated with KHSO₄ versus ionic radius of M with M= Ni²⁺, Co²⁺, Mn²⁺. e) X-ray energy dispersive spectroscopy of NMC pristine and (f) NMC treated with KHSO₄ at 400°C under air.

Table II-4: Results of the Rietveld refinement of NMC: KHSO₄ [1: 3] heat treated at 400°C under air.

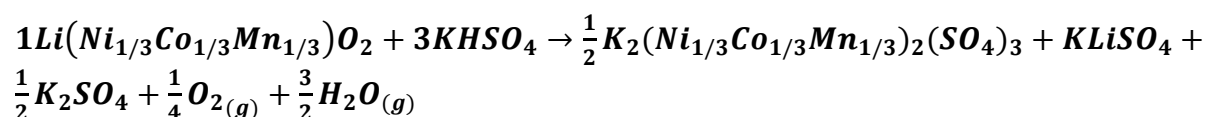
Phases	a (Å)	b (Å)	c (Å)	Bragg R-factor%	wt. %
K ₂ Co ₂ (SO ₄) ₃	9.9597(2)	9.9597(2)	9.9597(2)	6.72	42.86(48)
KLiSO ₄	5.1452(2)	5.1452(2)	8.62825(4)	6.62	32.36(38)
K ₂ SO ₄	7.482(9)	10.072(9)	5.771(6)	21.7	24.78(42)

Table II-5: Experimental (EDS) and calculated cationic ratio.

Cationic ratio	Experimental (EDS)	Calculated
$\frac{Co}{Ni}$	$\frac{1.73}{1.7} = 1.01$	$\frac{0.33}{0.33} = 1$
$\frac{Mn}{Ni}$	$\frac{1.56}{1.7} = 0.92$	$\frac{0.33}{0.33} = 1$

Based on the above results, **Equation II-3** was proposed for NMC, which was further confirmed by quantitative-phase analyses obtained by Rietveld refinements (**Table II-4**).

Equation II-3:



II.4.2.2 Extension to NCA (LiNi_{0.82}Co_{0.15}Al_{0.03}O₂)

In the same way, the reactivity of NCA cathode material with KHSO₄ was studied. The NCA: KHSO₄ [1: 3] mixture was heated at 400°C under air and analyzed by XRD analysis. The XRD pattern (**Figure II-8.a**) was indexed with: KLiSO₄, K₂SO₄, K₂M₂(SO₄)₃ and small peaks located at 12.25°; 27.53°; 32.65°; 41.29° and 58.71° identified as K₃Al(SO₄)₃, which the structure has not been solved yet. **Figure II-8.b** represent the experimental XRD peaks of the K₂M₂(SO₄)₃ phase and those of the theoretical phases K₂Ni₂(SO₄)₃ and K₂Co₂(SO₄)₃. It shows that the experimental peaks are within the two theoretical phases and close to K₂Ni₂(SO₄)₃. Therefore, the Rietveld refinement of the XRD pattern was performed with KLiSO₄, K₂SO₄, and

$\text{K}_2\text{Ni}_2(\text{SO}_4)_3$. **Figure II-8.c** indicates suitable refinement except for the peak located at 27.53° identified as $\text{K}_3\text{Al}(\text{SO}_4)_3$. The obtained χ^2 , Bragg R-factors %, and cell parameters are listed in **Table II-6**. The unit cell parameter of experimental $\text{K}_2\text{Ni}_2(\text{SO}_4)_3$ (9.854(1) Å) is closer to the theoretical parameter of $\text{K}_2\text{Ni}_2(\text{SO}_4)_3$ (9.843 Å) due to the large cointent of nickel, $\frac{\text{Ni}^{2+}}{\text{Co}^{2+}} = 5.67$.

To confirm the presence of cobalt in the 4a site of the langbeinite type structure, X-ray energy dispersive spectroscopy was performed. **Figure II-8.e** and **Figure II-8.f** represent the EDS spectra of NCA pristine and NCA: KHSO_4 [1: 3] heat treated at 400°C under air. The atomic ratio of $\frac{\text{Ni}^{2+}}{\text{Co}^{2+}} = 5.61$ on the same crystal from sulfate-based products is similar to the ratio $\frac{\text{Ni}^{2+}}{\text{Co}^{2+}} = 5.67$ of NCA pristine. It confirms the stabilization of cobalt and nickel in the langbeinite, *i.e.* the formation of $\text{K}_2(\text{Ni}_{0.85}\text{Co}_{0.15})_2(\text{SO}_4)_3$.

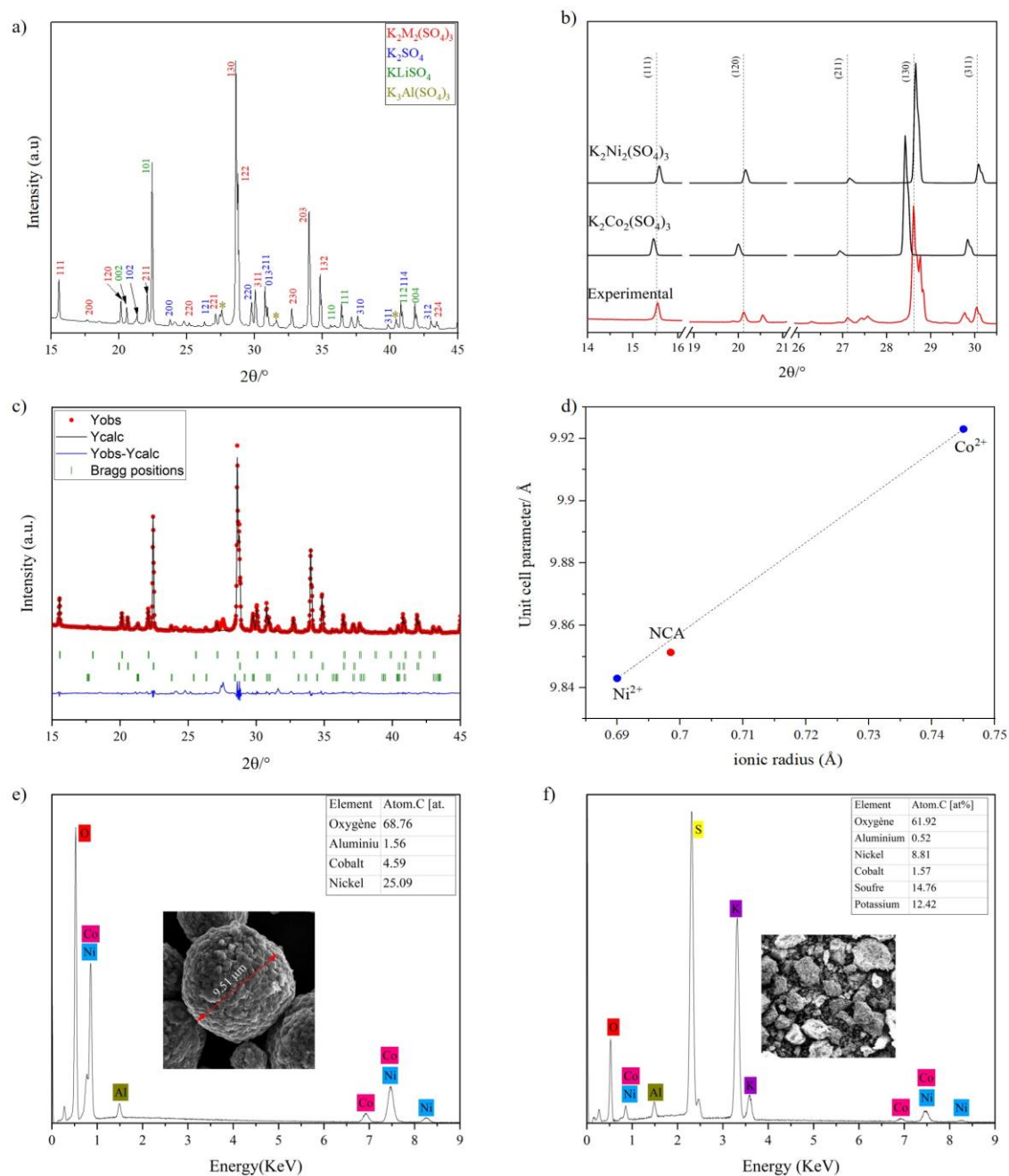


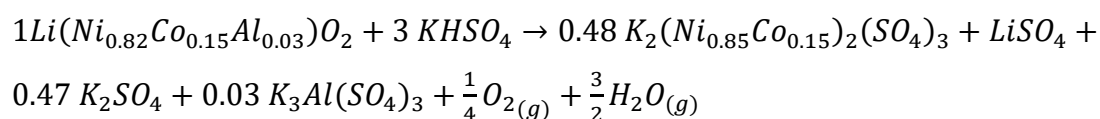
Figure II-8: **a)** XRD pattern of sulfate product obtained by heat treatment of NCA: KHSO_4 [1: 3] at 400°C under air. **b)** Comparison of XRD peaks of NCA after heat treatment with KHSO_4 , and $\text{K}_2\text{Ni}_2(\text{SO}_4)_3$ and $\text{K}_2\text{Co}_2(\text{SO}_4)_3$. **c)** Rietveld refinements of XRD pattern of NCA after thermal treatment with KHSO_4 . **d)** Unit cell parameters of $\text{K}_2\text{Ni}_2(\text{SO}_4)_3$, $\text{K}_2\text{Co}_2(\text{SO}_4)_3$, and NCA treated with KHSO_4 versus ionic radius of M with $\text{M} = \text{Ni}^{2+}, \text{Co}^{2+}, \text{Mn}^{2+}$. **e)** X-ray energy dispersive spectroscopy of NCA prictine and **(f)** NCA: KHSO_4 [1: 3] at 400°C under air.

Table II-6: Result of Rietveld refinement of NCA: KHSO₄ [1: 3] heat treated at 400°C under air.

Phases	a (Å)	b (Å)	c (Å)	Bragg factor%	R-	wt. %
K ₂ Co ₂ (SO ₄) ₃	9.854(2)	9.9597(2)	9.9597(2)	10.5		47 (2)
KLiSO ₄	5.145(3)	5.145(3)	8.631(6)	5.39		36 (1)
K ₂ SO ₄	7.480(2)	10.077(3)	5.772(2)	17.9		16 (1)

Based on the above results, **Equation II-4** was proposed for the sulfation of NCA positive electrode material using KHSO₄ molten salt.

Equation II-4:



II.4.3 Conclusion

The extension of sulfation process to NMC and NCA positive electrode materials was established with the same reaction parameters to those obtained for LiCoO₂ *i.e.* stoichiometry, temperature and atmosphere. The XRD and the X-ray energy dispersive spectroscopy analyses indicate the formation of a solid solution Ni, Co, and Mn in the (4a) site of the langbeinite crystal. However, the Al⁺³ from NCA was stabilized in K₃Al(SO₄)₃ structure.

Table II-7, shows the variation of *a* cell parameter of langbeinite K₂M₂(SO₄)₃ with the nature of M. The cell parameter of langbeinite K₂M₂(SO₄)₃ is higher for NCA compared to LCO due to the presence of Mn⁺² with higher ionic radius (0.83Å). While, for NMC the *a* cell parameter is lower due to the presence of Ni⁺² (0.69Å). This result confirms the stability and flexibility of langbeinite crystal, allowing the extension of the sulfation process to NMC and NCA type chemistry.

Table II-7: Comparison of cell parameters of sulfate-based product obtained upon the heat treatment of LCO, NMC, and NCA with KHSO₄ molten salt.

		LiCoO ₂	NMC	NCA
Cell parameters	K ₂ M ₂ (SO ₄) ₃ (Å)	9.92590(5)	9.9597(2)	9.854(2)

II.5 Mechanistic investigation

II.5.1 Differential scanning calorimetry

The sulfation reaction was first characterized by Differential Scanning Calorimetry study (DSC) performed with the collaboration of LRCS (Matthieu COURTY). First, the pristine KHSO_4 was analyzed. During the DSC measurement, KHSO_4 was heat treated from 30 to 400°C under argon. The DSC curve (**Figure II-9.a**) shows three endothermic peaks: one at 187°C, another one at 213°C and third one at 317°C. Moreover, the TGA measurement (represented by green line in **Figure II-9**) shows a small weight loss ($\sim 0.53\%$) at around 195°C, followed by an important loss of water (determined by MS in **Figure II-5**). According to the literature, the first endothermic peak at 187°C corresponds to a solid-solid phase transition⁷⁰. The second peak *i.e.* main peak observed at 213°C was assigned to the melting of KHSO_4 ⁷⁰⁻⁷². The last broad peak is assigned to the decomposition of KHSO_4 .

In order to confirm the phase transition of KHSO_4 occurring at 187°C, variable-temperature X-ray diffraction analysis was performed. During the analysis, KHSO_4 was heated from 30 °C to 200°C with a heat rate of 5°C/min. The collected XRD patterns at 30°C, 60°C and 180°C were represented in **Figure II-9.b**. At 30°C and 60°C, the XRD pattern ($\text{KHSO}_4 @ 30^\circ\text{C} @ 60$) were indexed with the pristine KHSO_4 (orthorhombic, SG: P b c a). When the temperature reaches 180°C ($\text{KHSO}_4 @ 180^\circ\text{C}$ shown in **Figure II-9.b**), a phase transition occurs confirming the literature assignment⁷³.

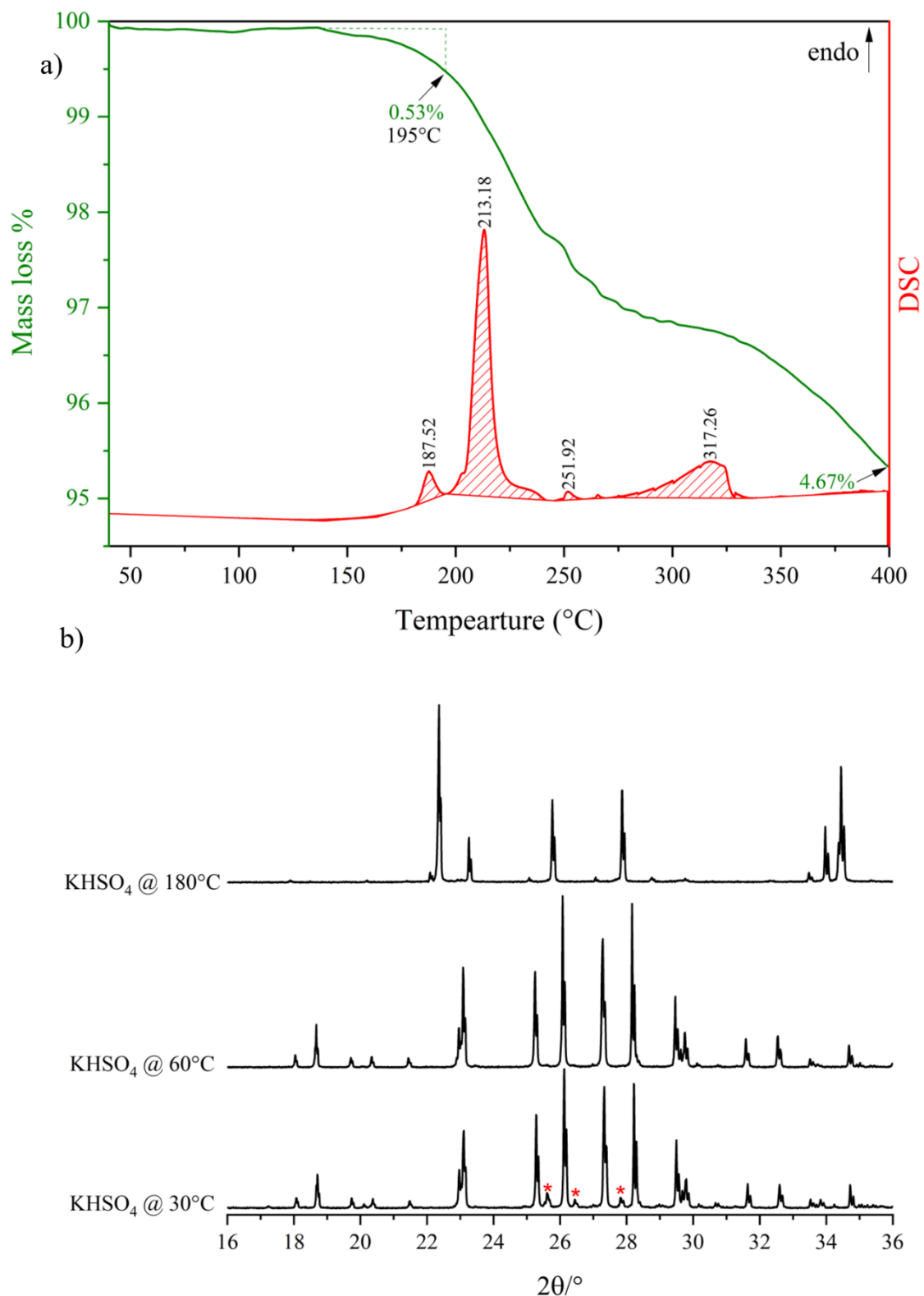


Figure II-9: a) Differential Scanning Calorimetry of KHSO_4 heat treated from 40 to 400 $^{\circ}\text{C}$ with heating rate of 5 $^{\circ}\text{C}/\text{min}$ (red line) and TGA (green line). b) XRD patterns extracted at 30 $^{\circ}\text{C}$, 60 $^{\circ}\text{C}$ and 180 $^{\circ}\text{C}$ upon variable-temperature XRD experiment of KHSO_4 . * unidentified peaks.

Thereafter the sulfation reaction was investigated. The LiCoO_2 : KHSO_4 [1: 3] mixture was heated from 30°C to 400°C with heat rate of $5^\circ\text{C}/\text{min}$. The DSC thermogram **Figure II-10** is marked by two endothermic peaks at 183°C and at 203°C , and by two exothermic peaks at 212°C and 302°C . Compared to the KHSO_4 DSC result, the first endothermic peak (at 183°C) was assigned to the phase transition of KHSO_4 and the endothermic peak at 203°C correspond to the melting of KHSO_4 salt^{70,72}. This was confirmed by SEM imaging of a sample treated at 200°C showing the coating of LiCoO_2 particles by melted KHSO_4 (@200 inside **Figure II-10**). The exothermic peaks at 212 and 302°C result from the reaction of LiCoO_2 with KHSO_4 yielding the destruction of the pristine and the formation of small irregular particles with size between $4\ \mu\text{m}$ and $8\ \mu\text{m}$ (**Figure II-10**).

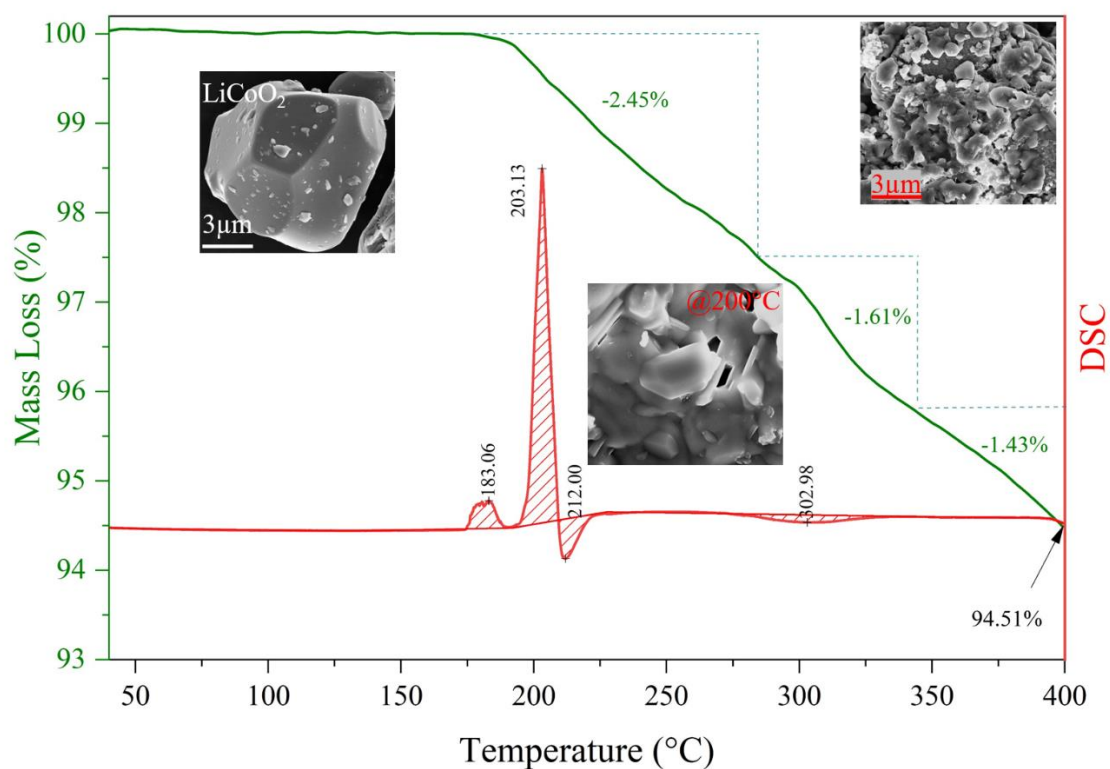


Figure II-10: Thermal analyses of LiCoO_2 : KHSO_4 [1: 3] mixture heat treated under argon atmosphere from 30°C to 400°C , DSC thermogram is represented by red line (endo up) and TGA represented by green line. Scanning electron microscopy (SEM) of pristine LiCoO_2 before (LiCoO_2) and after ex situ thermal treatment with KHSO_4 at 200°C (@200) and 400°C (@400).

II.5.2 Variable-temperature XRD analysis

To investigate the conversion mechanism, variable-temperature XRD analysis was performed, in reflection mode. During the analysis, LiCoO_2 : KHSO_4 [1:3] mixture was heated from 30°C

to 200°C, with a heating rate of 5°C/min. The final temperature was set before the melting point of KHSO₄, which leads to the loss of XRD signal with diffuse scattering. The XRD patterns were collected every 5°C step with a 30 min acquisition time. **Figure II-11.a** shows the evolution of XRD peaks as function of the temperature. From 30°C to 180°C, all the LiCoO₂ and KHSO₄ peaks shift slightly to lower angles, consistent with unit cells expansion. At 180°C, we observed the expected phase transition of KHSO₄, and remarkably the formation of a new phase indexed to K₄LiH₃(SO₄)₄ (tetragonal, S.G: P4₁)⁶¹. Such a formation indicates a H⁺/Li⁺ ionic exchange reaction. In this range of temperature, KHSO₄ has been shown to become a super-ionic conductor with proton conductivity of around 10⁻¹ S/cm (T=178 °C)⁷⁴. Therefore, the proton mobility is suggested to drive the H⁺/Li⁺ ionic exchange between LiCoO₂ and KHSO₄.

To capture the delithiation of LiCoO₂, a zoom of the (003) Bragg reflexion as a function of the temperature is shown in **Figure II-11.b**. It shows that the Bragg peak shifted to lower 2θ values as the temperature increases. This can be interpreted by an increase of the *c*-parameter due to the repulsive force between facing oxide ions induced by removal of layered Li⁺ ions. In addition, it is expected that the thermal expansion of the crystal structure also contributes to the increase of the *c*-parameter. To distinct these two effects, the evolution of the *c*-parameter, determined by profile matching, was monitored for the pristine LiCoO₂ as a function of the temperature (**Figure II-12.a**). The result shows a linear increase upon heating. Concerning the mixture LiCoO₂: KHSO₄ [1: 3] we observed a deviation from this linear increase at around 180°C, which correspond to the temperature where K₄LiH₃(SO₄)₄ started to appear (**Figure II-12.a**). Such a difference is hence related to the delithiation of the layered structure and the increasing repulsive effect of faced oxide ions. By considering that the delithiation of LiCoO₂ is characterized by a Vegard Law, *i.e.*, a quasi linear variation of the *c*-parameter as a function of *x* in Li_{1-x}CoO₂ (**Figure II-12.b**), it is possible to assess the number of Li⁺ ions remaining within the layered structure. Moreover, it is assumed that the lithium removal is counterbalanced by the intercalation of H⁺ yielding to the general chemical formula H_xLi_{1-x}CoO₂. The assessed chemical formulae were added in **Figure II-12.a** reaching up to H_{0.17}Li_{0.83}CoO₂ at 200 °C. Hence, variable-temperature XRD experiment revealed the formation of a solid solution H_xLi_{1-x}CoO₂ as an intermediate phase during the sulfation reaction. Deeper insights into the existence of this phase will be assessed by using x-ray absorption spectroscopy (see next section).

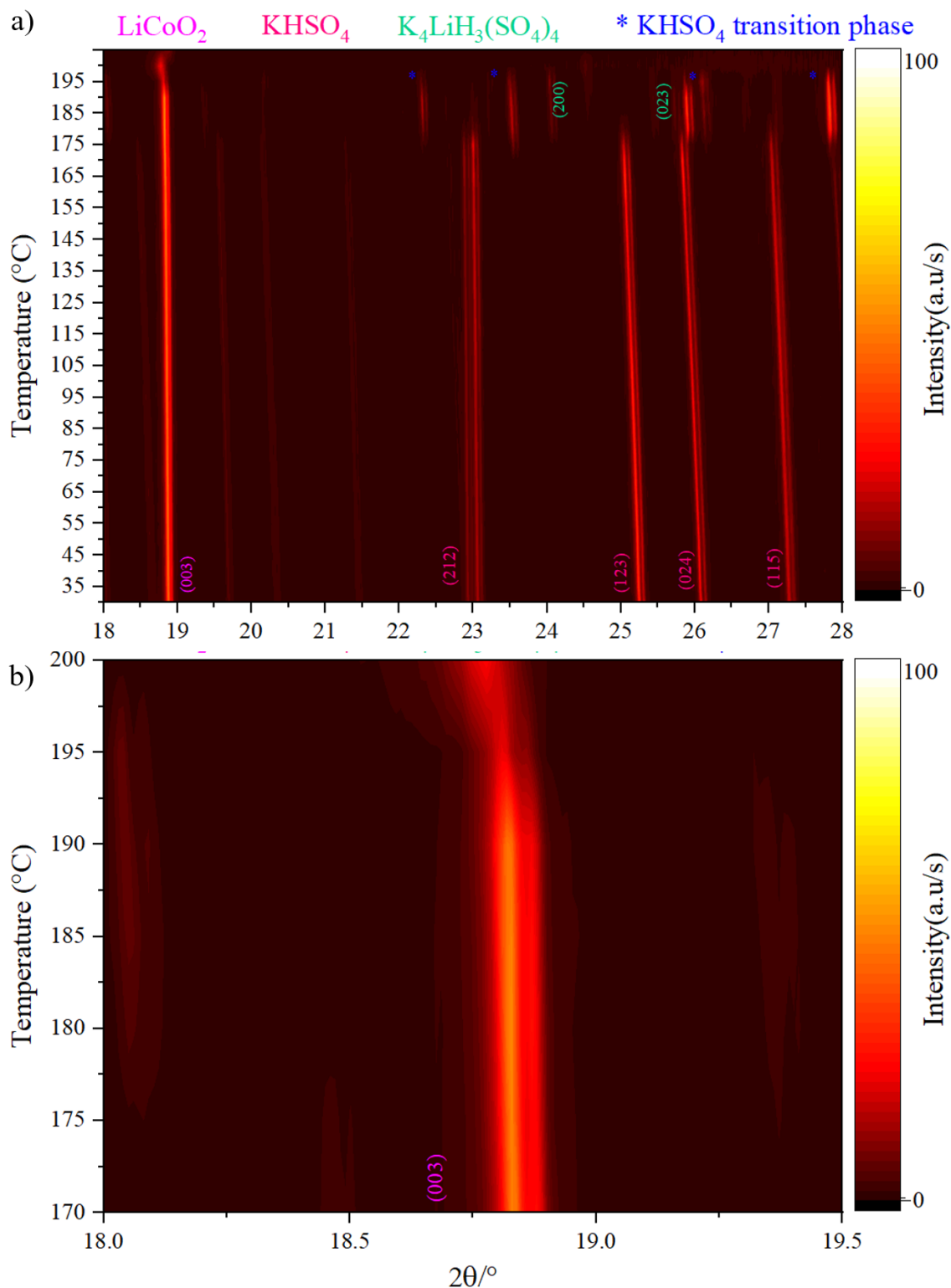


Figure II-11: a) contour plot of XRD patterns collected upon in situ thermogravimetric analysis of LiCoO_2 : KHSO_4 [1:3] from 30°C to 400°C with heating rate of 5°C/min. **b)** zoom of (003) plan of LiCoO_2 as function of temperature.

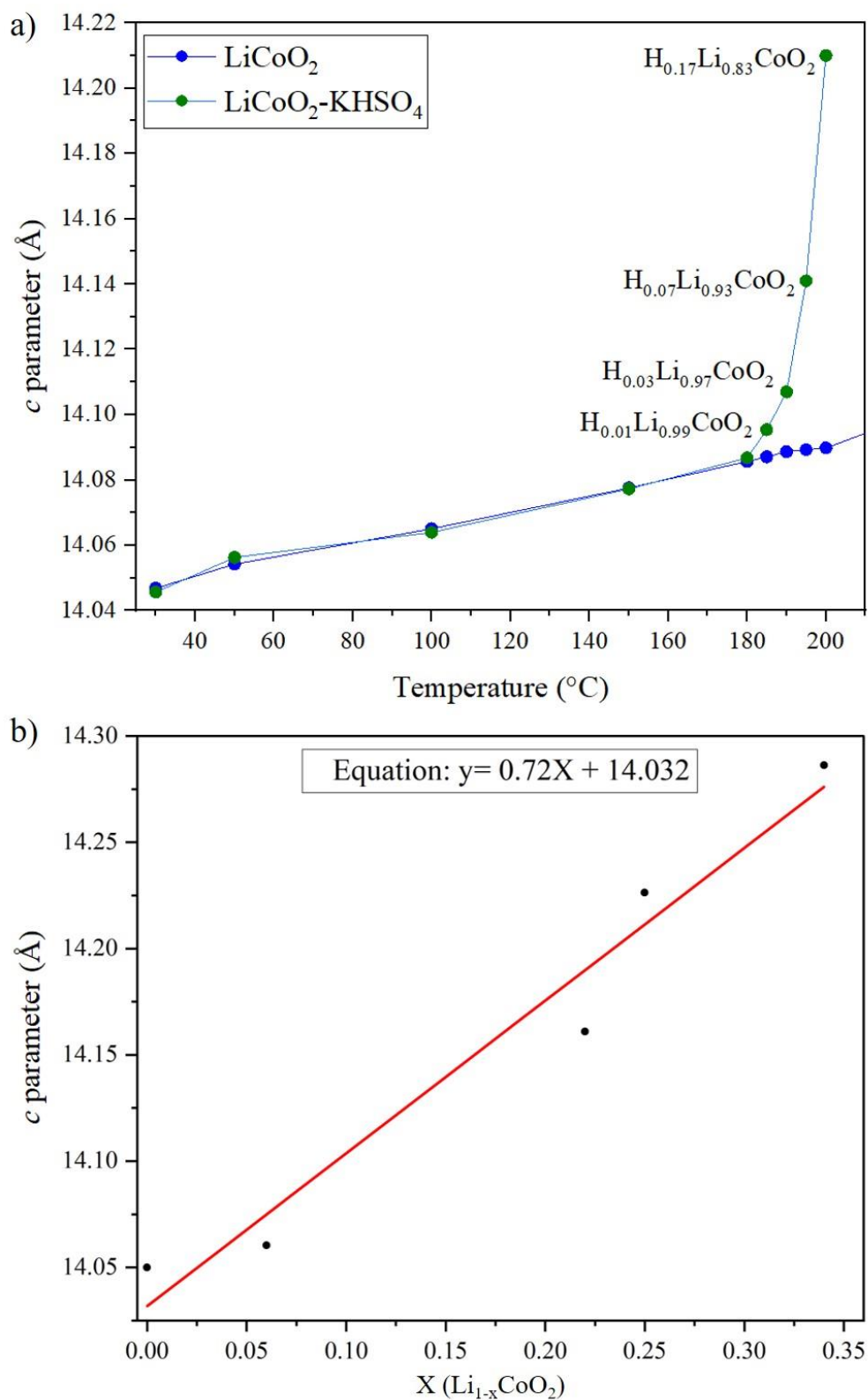


Figure II-12: (a) Evolution of c parameter of LiCoO₂ pristine (bleu) and c parameter of LiCoO₂ during the sulfation process as function of temperature. (b) Evolution of c parameter as function of the X (Li_{1-x}CoO₂).

II.5.3 X-ray absorption spectroscopy

II.5.3.1 Principle

X-ray Absorption Spectroscopy is mainly used to investigate atomic local structure and electronic states of atoms. It consists in the measurement of the quantity of energy absorbed by the matter to eject one electron, from the core electronic states of the metal into the excited electronic states and the continuum⁷⁵. Each element has its specific energy, thus the control of the X-ray energy is mandatory to probe the specific element.

The collected XAS spectrum represent the variation of the absorption coefficient (μ) as function of the incident energy E (eV). with:

$$\mu = \ln \frac{I_0}{I}$$

where I_0 and I are the intensities of the incident and the transmitted beam.

The XAS spectrum (**Figure II-13**) is divided in two regions: the X-ray absorption near-edge structure (XANES)^{75,76} and the extended X-ray absorption fine structure (EXAFS)^{75,76}. The XANES part includes the transitions of the electron from the core electronic states of the metal to empty electronic state. While, the EXAFS part is related to interaction of ejected electron with neighboring atoms. The two parts give complementary structural information. The XANES spectra assesses the electronic structure and the symmetry of the probed atom. The EXAFS reports the numbers, the types, and the distances to neighboring atoms from the absorbing element.

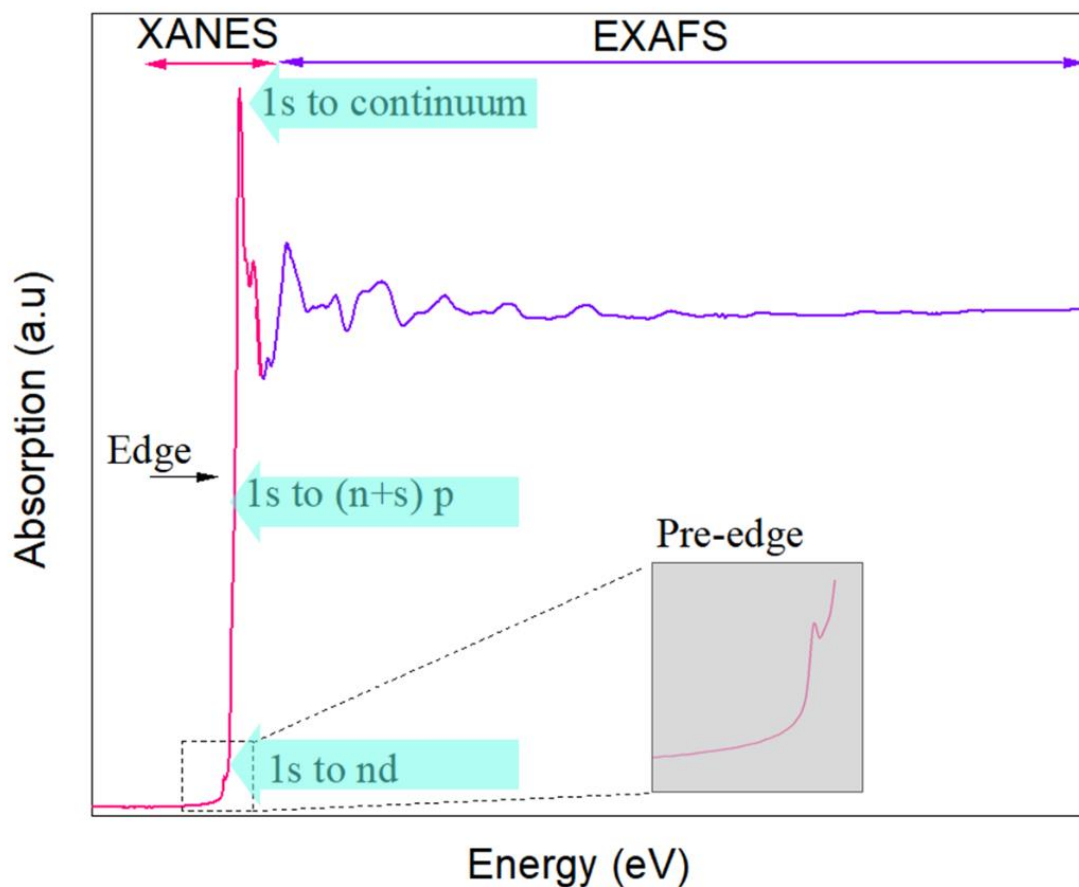


Figure II-13: Illustration of XAS spectrum with XANES and EXAFS regions

II.5.3.2 EXAFS oscillation

The EXAFS oscillations result from the interference between the outgoing photoelectron wave, caused by ejection of core electron to continuum, and the backscattered wave of neighboring atoms. **Figure II-14** illustrates the concept of interference in the EXAFS part. The EXAFS oscillation in the k domain $\chi(k)$ is described by the well-known equation⁷⁷ mentioned below (**Equation II-5**). $\chi(k)$ is the summation of all possible photoelectron scattering paths. The terms $F_i(k)$, $\delta_i(k)$, and $\lambda(k)$ are the scattering amplitude, the phase shift, and the mean free path of the photoelectron, respectively. These terms are related to the scattering properties that depend only on the nature of the neighboring atoms. It is important to know that these terms are not affected by distance or coordination number changes caused during the experiment. This applies also to S_0^2 , the amplitude of waves backscattering to the central atom. However, the terms N_i (coordination number of identical paths), R_i (half path length), E_0 (energy), and σ^2

(Debye–Waller factor) are the structural parameters, which are largely affected during the experimental changes.

Equation II-5:

$$\chi(k) = \sum_i \frac{(N_i S_0^2) F_i(k)}{k R_i^2} \sin[2k R_i + \delta_i(k)] e^{-2\sigma_i^2 k^2} e^{-\frac{2R_i}{\lambda(k)}}$$

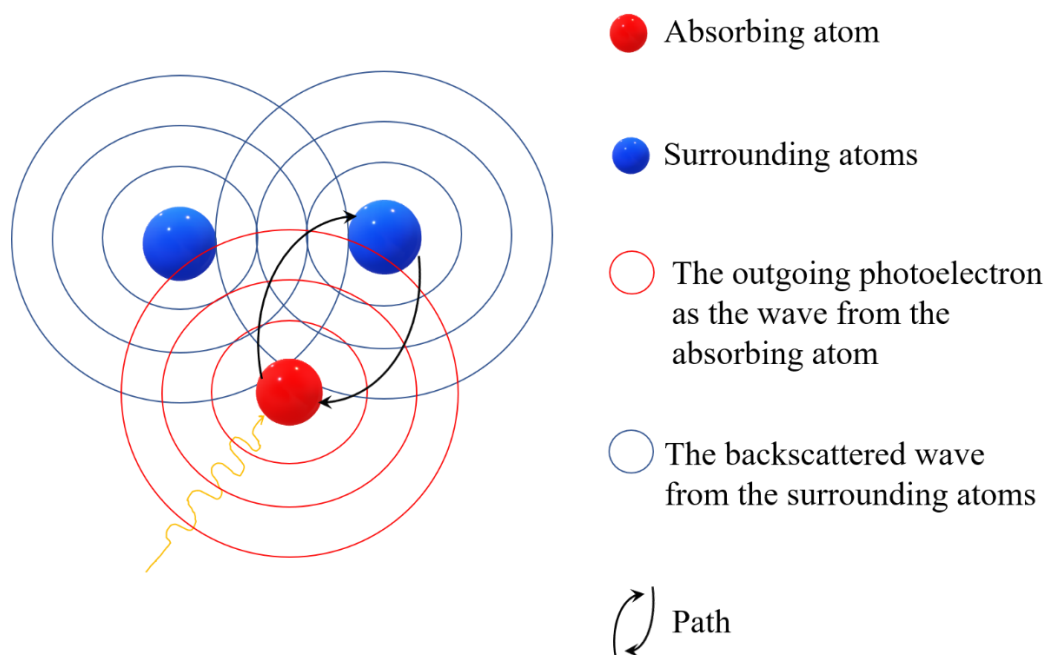


Figure II-14: A schematic representation of the outgoing and backscattered photoelectron wave, which illustrates the concept of interference in EXAFS.

To get more fine details about the local structure of the probed atom, the EXAFS oscillations are refined, using theoretical standards computed by the popular FEFF calculated^{77,78} for all scattering paths of the ejected electron. This means that values of the parametric terms S_0^2 , E_0 , N , R and σ^2 must be specified for each path included in the fit. The path means the way taken by electron from the ejection until the return to the probed atom. Note that S_0^2 is determined from the fit of the reference and depend on the molar concentration of the probed atom. The obtained result shows the FT-EXAFS spectra which are calculated according to the equations below.

$$|\chi(R)| = \sqrt{(Re[\chi(R)])^2 + (Im[\chi(R)])^2}$$

And

$$\chi(R) = \int_{k_i}^{k_f} W(k)k^n \chi(k) [\cos(2\pi kR) + i \sin(2\pi kR)] dk$$

where $W(k)$ is a window function which dampens the extremes of $\chi(k)$ and k^n is the k -weighting. $\chi(R)$ contains both real ($\text{Re}[\chi(R)]$) and imaginary ($\text{Im}[\chi(R)]$) parts, which are combined to calculate the magnitude of $\chi(R)$ affording an envelope of the real and imaginary parts.

II.5.3.3 XAS experiment

To probe the atomic changes occurring during the sulfation, the reaction process was monitored by a temperature-controlled *in situ* X-ray absorption spectroscopy (XAS), including X-ray absorption near edge structure (XANES) and Extended X-Ray Absorption Fine Structure (EXAFS). During the study, a mixture of LiCoO_2 and 3 KHSO_4 was placed in home-made Boron nitride cell developed in PHENIX laboratory by Anne-Laure ROLLET *et al*⁷⁹ as detailed below.

Specific setups represented in **Figure II-15.a** (Cell, heating device and chamber) are developed to carry out high temperature XAS experiment in molten salt. The setups operate in transmission mode, at temperature up to 500°C with stability of $\pm 2^\circ\text{C}$ and under controlled atmosphere. The system is composed by an aluminum chamber, ceramic chamber, heating device and cell. All setup elements contain the measurement zone represented by the orange frame inside **Figure II-15.a**. The cell was sandwiched inside heating device, which is placed inside ceramic chamber and placed on the aluminum chamber. The ceramic chamber allowing the atmosphere control around the cell and the heating element. Finally, the aluminum chamber adapted for fast mounting on the ROCK beamline and allows high control of atmosphere. Below, only the cell is detailed.

- Cell

The cell has been designed to be non-leaking and inert to both molten salts and transition metals. HP grade boron nitride was selected because of its low thermal expansion, high-temperature stability (melting point 2600°C), non-wetting by molten metals, and chemical inertness. In addition, for materials containing elements with atomic numbers between 20-50, in this case $\text{Co}=27$, the sample thickness will be between 20 and $100\mu\text{m}$ ⁸⁰. **Figure II-15.b** shows a scheme of our designed cell. The cell is composed by two BN cuboids of 1 cm thick. In the first cuboid, a cavity of $100\mu\text{m}$ in depth, was drilled for receiving the LiCoO_2 : KHSO_4 mixture introduced as a pellet in the measurement zone *i.e.* where X-ray beam will pass. To increase the X-ray

transmission at the measurement zone, the lengths of both BN cuboids (Sample holder and lid) were hollowed to 300 μm .

- Cell preparation

To prepare the XAS measurement, 100 mg of LiCoO_2 and 3 KHSO_4 was placed as pellet (100 μm) in the first cuboid of cell (**Figure II-15.c**). Then the two parts of the cell are closed together with an alumina ceramic glue. Finally, the cell was placed in the other elements as describe in the **Figure 15**

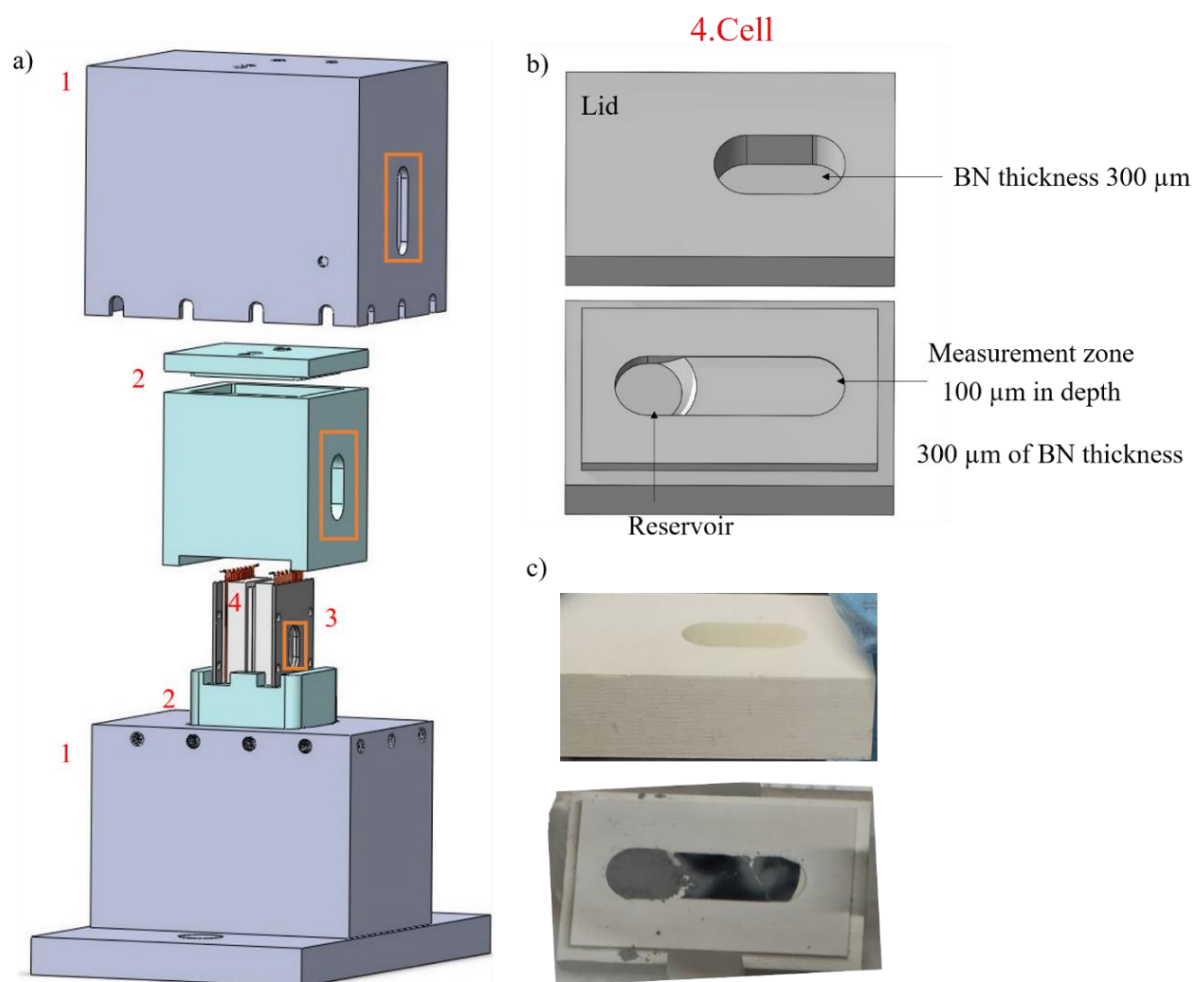


Figure II-15: XAS setup (a) view of total designed setup: 1- aluminum chamber, 2- ceramic chamber, 3 heating device and 4- cell. (b) scheme of the boron nitride cell (c) image of cell containing $\text{LiCoO}_2/\text{KHSO}_4$ mixture.

- XAS measurements:

X-ray absorption spectroscopy experiments were carried out on the ROCK beamline of SOLEIL synchrotron (France) with (Valérie BRIOIS). The XAS was performed in transmission mode at the K-edge of cobalt *i.e.* 7709 eV. This energy corresponds to the required energy to eject a core electron of the cobalt atom. During the study, the cell was heated from room temperature (30°C) to 400°C with a heating rate of 5°C/min, followed by an isotherm step at 400°C. The collected spectra were investigated to determine the evolution of the oxidation state of cobalt (XANES spectra), and to identify the reaction mechanism by chemometric analysis MCR-ALS of EXAFS spectra.

II.5.3.4 Cobalt oxidation state

The collected XANES spectra during the heat treatment of LiCoO_2 : KHSO_4 [1:3] are gathered in **Figure II-16**. The spectra reveal a systematic change in the local electronic structure of cobalt. Upon heat treatment, a progressive shift of the absorption edge, from 7724 eV toward lower energy 7720eV was observed, consistent with the progressive reduction of cobalt III to cobalt II. The change observed on the pre-peak, white line, and the edge peaks are discussed below. In addition, at energies higher than 7730 eV, the spectra show also a strong changes related to phase transitions.

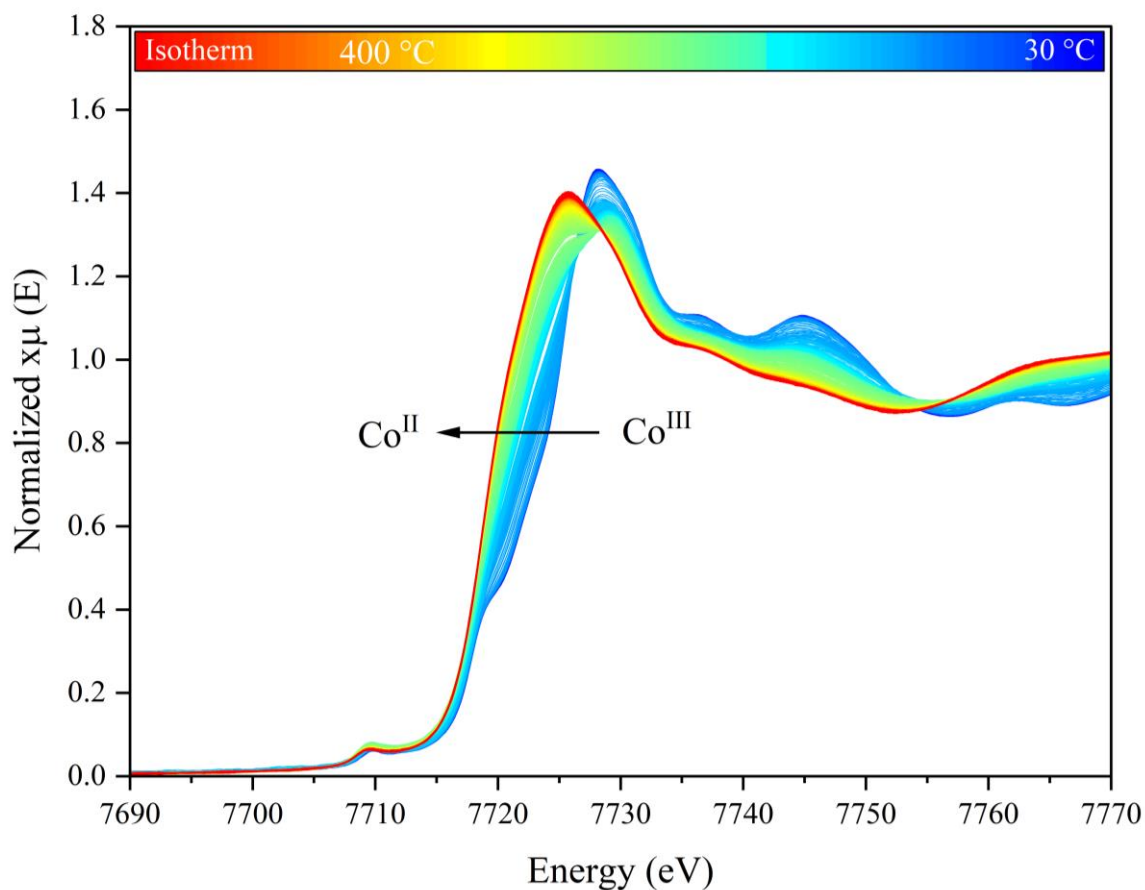


Figure II-16: XAS spectra collected during the thermal treatment of LiCoO₂: KHSO₄ [1: 3] from RT (blue) to 400°C (red).

II.5.3.5 Characterization of reaction mechanism:

To better understand the structural change occurring upon the sulfation of LiCoO₂, the evolution of XANES and EXAFS spectra as function of temperature have been investigated. The evolution of spectra shows the presence of three main temperature area.

- 1- From 30°C to 200°C
- 2- From 200°C to 220°C
- 3- Over 220°C

1. Evolution of XANES spectra collected from 30°C to 200°C

Figure II-17, shows the XANES spectra of LiCoO₂: KHSO₄ [1: 3] mixture collected upon heating from 30°C to 198°C. These spectra are similar to theoretical spectrum of O3 layered rock-salt LiCoO₂ with rhombohedral symmetry^{81,82}. The spectra show the presence of five main features located at 7709.7 eV, 7718.7 eV, 7722.4 eV, 7728.2 eV, and 7730.9 eV. The pre-edge peak at 7709.7 eV represent the electric dipole-forbidden transition of a 1s electron to an unoccupied 3d orbital of the low-spin state ($t_{2g}^6 e_g^0$) in the Co³⁺ ion⁸³. The shoulders (B1, B2) located at 7718.7 eV and 7722.4 eV are formed due to the dipole-allowed 1s → 4p transition, leading to the final state ($1s^1 3d^7 L 4p^1$), with a shakedown process caused by charge transfer from ligand to metal, where L is a ligand hole. The C1 and C2 peaks located at 7728.2 eV and 7730.9 eV, were assigned to the purely dipole-allowed 1s→4p transition leading to the final state ($1s^1 3d^6 4p^1$). The presence of double peak B1, B2 and C1, C2 in white line and edge peak, respectively, is because the layered rock-salt LiCoO₂ is not a cubic system, thus the orientation impacts the XANES spectra⁸¹. Overall, in this temperature range, the XANES spectra showed only minor changes.

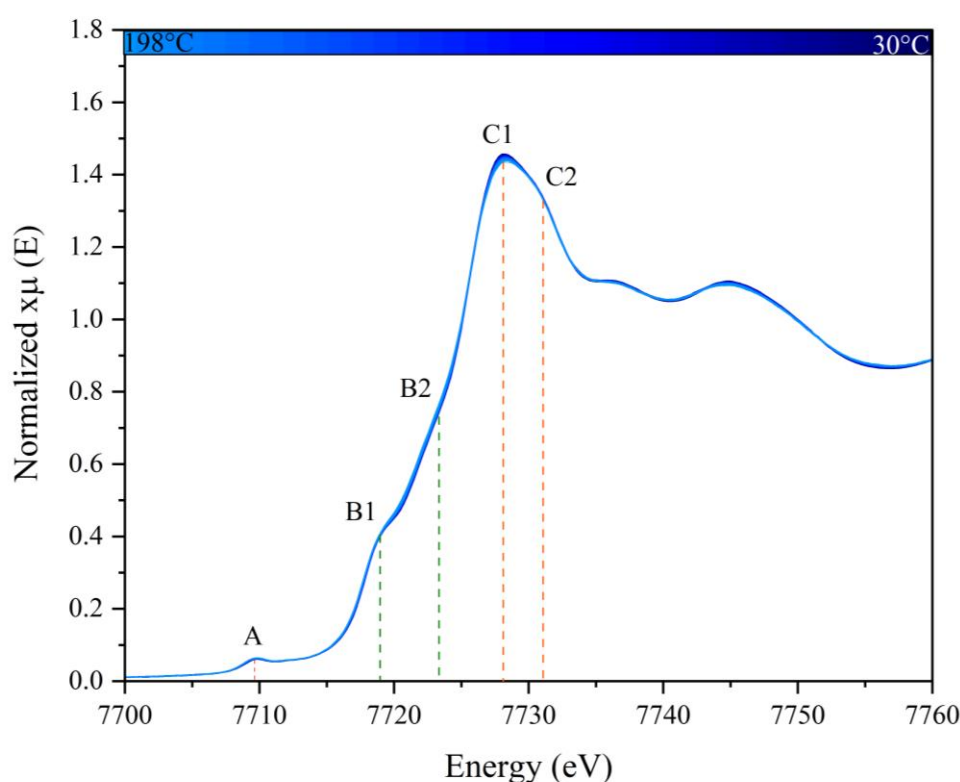


Figure II-17: XANES part of XAS spectra collected from 30°C to 198°C during the heat treatment of LiCoO₂ and KHSO₄ mixture

- Refinement of EXAFS spectra

To confirm the structural stability of CoO_6 octahedra upon heating, the refinement of the EXAFS oscillations of the collected spectra between 30°C and 190°C was carried out. **Figure II-18** shows magnitude of Fourier transformation of k^3 weighted EXAFS oscillations, $|\chi(\text{R})|$, for LiCoO_2 reference and spectra collected at 30°C , 180°C , and 190°C and their fits. The calculated data reproduce well the experimental data, and low R-factor are obtained. For all the $|\chi(\text{R})|$, from 0 to 4 Å, the $|\chi(\text{R})|$ display two peaks, the first one corresponds to six Co-O (1.91Å) distances, and second peak represent Co-Co (2.83Å) distances. **Table II-8** list the refinement results including the N (coordination number), S_0^2 (amplitude), σ^2 (Debye Waller factor), distance obtained from LiCoO_2 reference (R reference), the calculated distance from the experimental data (R), and the R-factor. As observed, the Co-O distances remains constant confirming the stability of LiCoO_2 structure. While, the σ^2 increase due with a temperature *i.e.* Debye Waller effect.

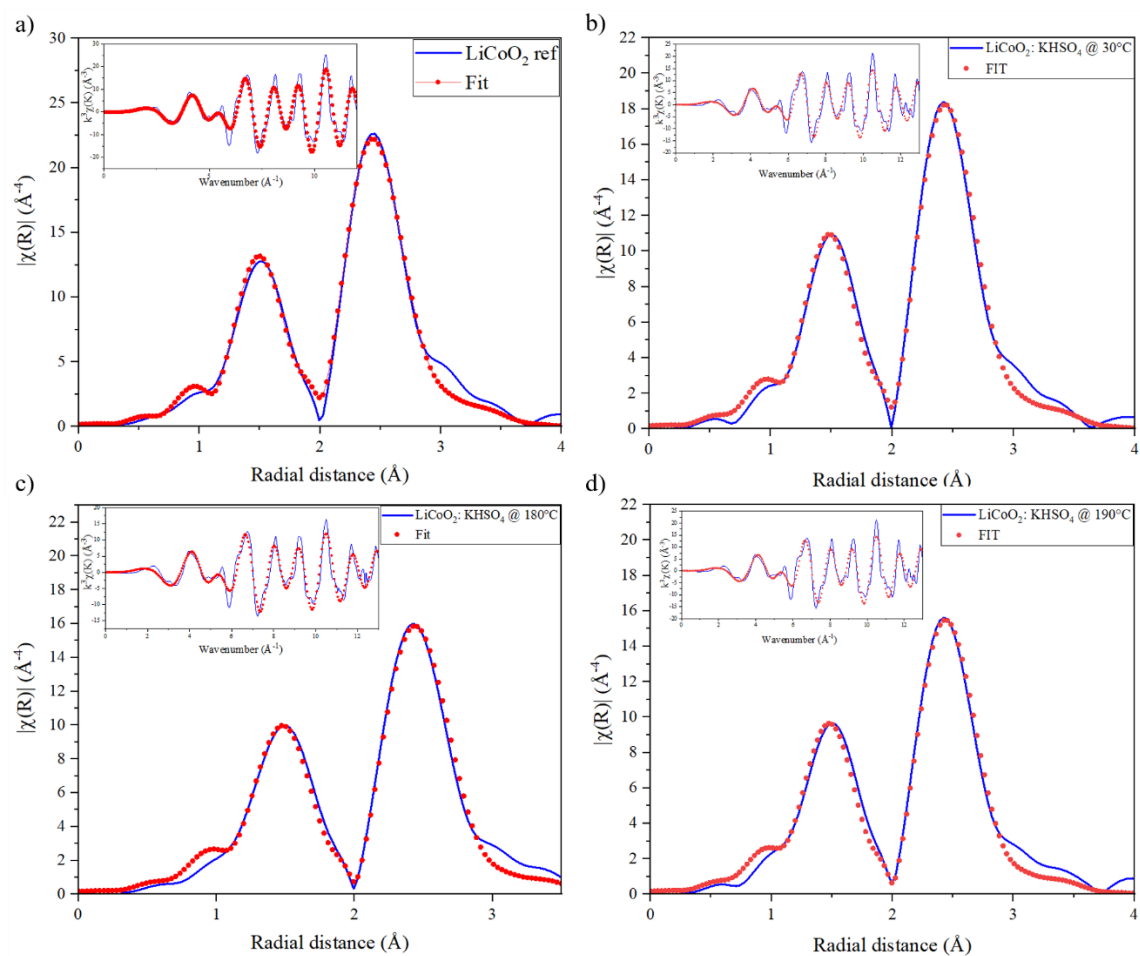


Figure II-18: Magnitude of Fourier transformation of k^3 weighted EXAFS oscillations for LiCoO₂ (a) and those collected at 30°C (b), 180°C (c) and 190°C (d), along with fitting result. Insets show the quality of fit in k-space.

Table II-8: Results of refinement of the EXAFS oscillations for LiCoO₂ reference and those collected at 30°C, at 180°C, 190°C.

Temperature	Name	N	σ^2	E_0	R ref	R	R-factor
LiCoO ₂ reference	Co - O	6	0.00118	-5.28	1.92	1.89	0.014
	Co - Co	6	0.00142	-5.28	2.82	2.82	
30°C	Co - O	6	0.00218	-5.450	1.92	1.91	0.013
	Co - Co	6	0.00142	-5.450	2.82	2.81	
180°C	Co - O	6	0.00290	-5.480	1.92	1.91	0.016
	Co - Co	6	0.00229	-5.480	2.82	2.82	

190°C	Co - O	6	0.00327	-5.480	1.92	1.91	0.014
	Co - Co	6	0.00246	-5.480	2.82	2.83	

2. Evolution of XANES spectra collected from 200 °C to 220°C

Thereafter, upon the heat treatment from 200°C to 220°C (**Figure II-19**), the changes on the shape and position of XANES peaks was observed. The pre-edge peaks growth and shift slightly to higher energies. In the same way, the intensity of *B1* (7718.7 eV) and *B2* (7722.4 eV) peaks increase. Nevertheless, it was observed that the intensity of edge peak located at 7728.2 (*C1*) eV and 7730.9 eV (*C2*) decrease. The changes in the pre-edge and edge peaks reveal distortion of cobalt octahedra. In addition, the increase on the intensities of the shoulder peaks *B1* and *B2* suggest a change in the iono-covalent character of the Co and ligand bonds.

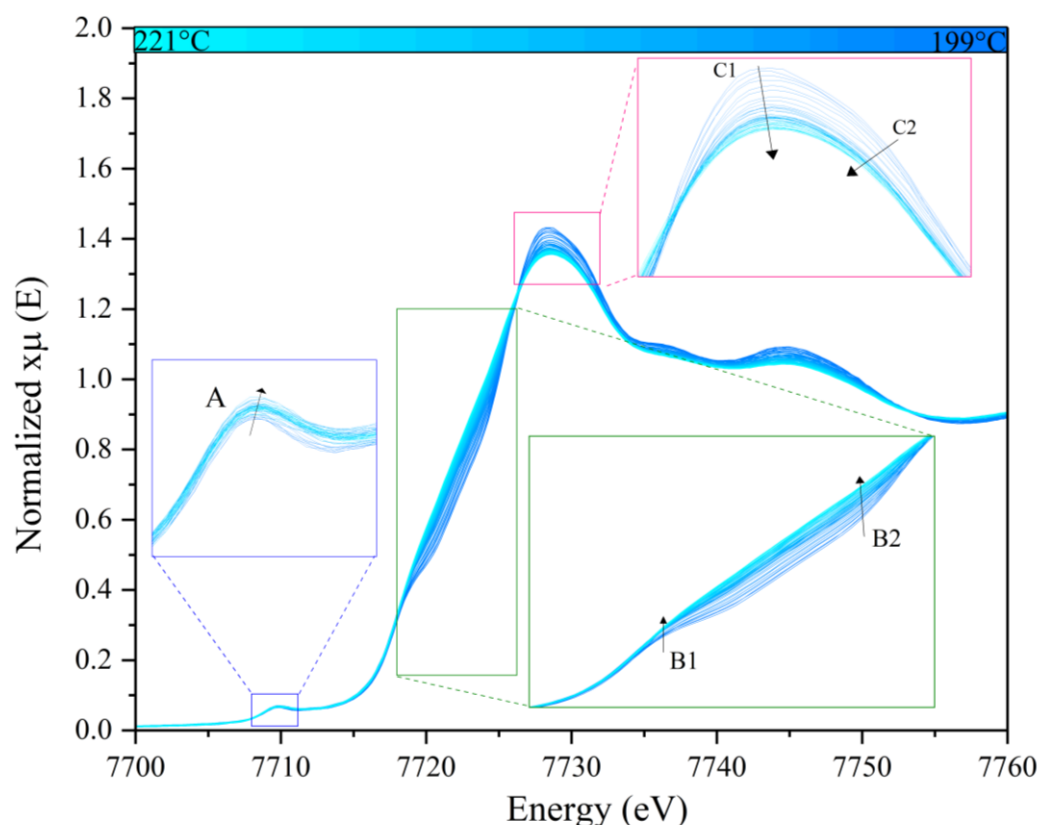


Figure II-19: XANES part of XAS spectra collected from 199°C to 221°C during the heat treatment of $\text{LiCoO}_2: \text{KHSO}_4$ mixture. Insets evolution of pre-edge peak (A), the B1 and B2 from the white line, and edge peak (C1 and C2)

- Refinement of EXAFS spectra

The $|\chi(R)|$ of spectra collected between 200 and 220 °C features two main peaks, the first one corresponding to CoO_6 octahedra (first shell) and a second peak corresponding to the Co-Co distances. Above 200°C, the first peak showed some changes, so the refinement using a regular CoO_6 octahedra cannot reproduce the experimental data. An example is shown for in **Figure II-20**. The refinement of $|\chi(R)|$ of EXAFS oscillations collected at 200°C with regular CoO_6 octahedra *i.e.* six Co-O (1.91Å) gives an R-factor= 0.024. While, the distortion of one Co-O distance improves refinement with R-factor = 0.0098. Thus, a distortion of the CoO_6 octahedra was introduced within the structural model and **Figure II-21** shows the corresponding fits obtained for selected spectra. **Table II-10** resumes the fit results. At 200°C, the fit highlights a distortion of the CoO_6 octahedra with one Co-O bond at 2.40 Å and 5 regular Co-O bond distances at 1.90 Å. Such a distortion, which evidences a 5-fold coordination, is also observed at 205 °C. At 210°C and 220°C, the refinements evidenced the occurrence of a [4+2] coordination mode with two long Co-O distances, resulting from ionic exchange *i.e.* formation of solid-solution $\text{H}_x\text{Li}_{1-x}\text{CoO}_2$.

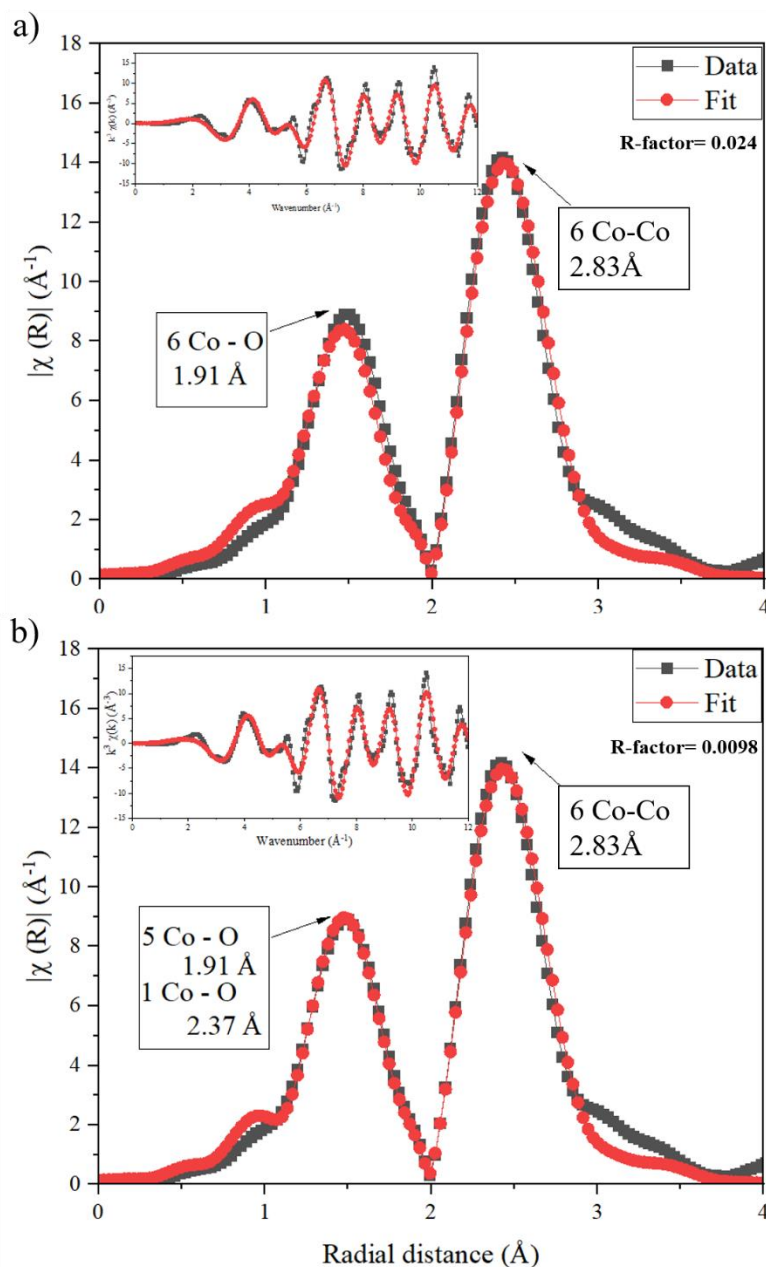


Figure II-20: Magnitude of Fourier transformation of k^3 weighted EXAFS oscillations collected at 205°C refined with (a) regular CoO_6 octahedra and (b) distortion one Co-O distance. Insets show the quality of fit in k -space.

Table II-9: Results of refinement of the EXAFS oscillations collected at 205°C with regular CoO₆ octahedra and distortion one Co-O distance. Insets show the quality of fit in k-space.

	Name	N	σ^2	E_0	R ref	R	R-factor
LiCoO ₂	Co- O	6	0.00440	-5.198	1.92	1.91	0.014
	Co- Co	6	0.00314	-5.198	2.82	2.83	
LiCoO ₂	Co- O	5	0.00228	-5.198	1.92	1.91	0.0098
	Co-O ₂	1	0.00810	-5.198	1.92	2.37	
	Co- Co	6	0.00319	-5.198	2.82	2.83	

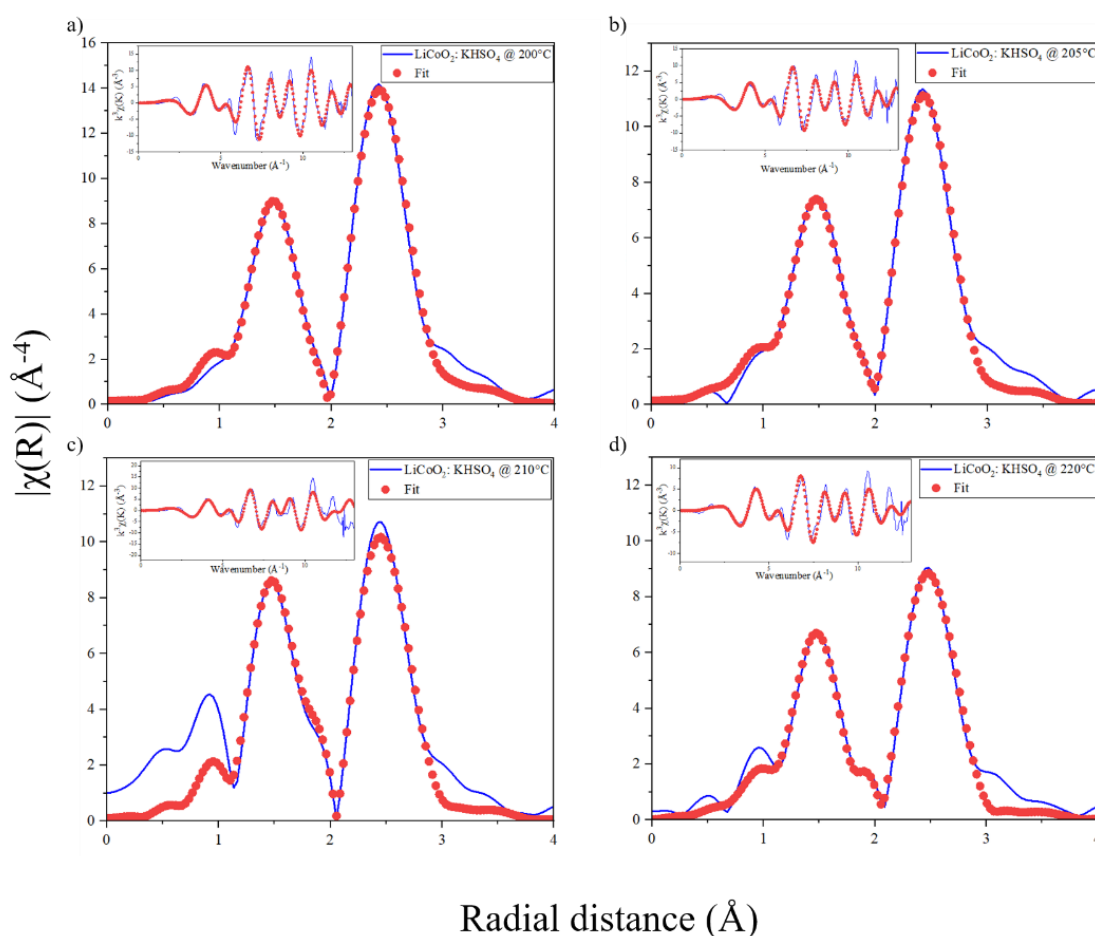


Figure II-21: Magnitude of Fourier transformation of k^3 weighted EXAFS oscillations collected at 200°C (a), 205°C (b), 210°C (c) and 220°C (d) along with fitting result. Insets show the quality of fit in k-space.

Table II-10: Evolution of structural parameters of LiCoO₂ upon the sulfation process obtained from EXAFS refinement for data collected at 200°C, at 205°C, 210°C, and 220°C

Temperature	Name	N	σ^2	E ₀	R ref	R	R-factor
200°C	Co - O	5	0.00232	-5.198	1.92	1.91	0.009
	Co-O	1	0.01540	-5.198	1.92	2.39	
	Co - Co	6	0.00317	-5.198	2.82	2.83	
205°C	Co - O	5	0.00378	-5.461	1.92130	1.90892	0.009
	Co-O	1	0.01178	-5.461	1.92130	2.33248	
	Co - Co	6	0.00470	-5.461	2.81610	2.82727	
210°C	Co - O	4	0.00409	-4.141	1.92	1.91	0.013
	Co-O	2	0.01490	-4.141	1.92	2.19	
	Co - Co	6	0.00516	-4.141	2.82	2.85	
220°C	Co - O	4	0.00378	-1.119	1.92	1.89	0.020
	Co-O	2	0.01811	-1.119	1.92	2.49	
	Co - Co	6	0.0058	-1.119	2.82	2.81	

3. Evolution of XANES spectra collected from 221 °C to 400 °C

Following the previous section which showed that the solid-solution H_xLi_{1-x}CoO₂ is characterized by a local distortion of the cobalt coordination mode up to 220 °C, beyond this temperature, the EXAFS cannot be refined using a layered type structure. In the following, the evolution of the XANES spectra was described to 400 °C.

Upon heating, from 220 to 250°C **Figure II-22.a**, the pre-edge growth and edge peaks intensities decrease, indicating a further CoO₆ distortion. Although, by increasing temperature above 250°C (**Figure II-22.b**), the intensity a pre-edge peak decreases continuously, consistent with formation of regular CoO₆. In addition, the absorption edge (white line B1 and B2 peaks)

shift to lower energies, confirming reduction of cobalt. When temperature reach 400°C and during the isotherm step (**Figure II-22.c**), the pre-edge and edge peak further evolves, indicating formation of more regular cobalt.

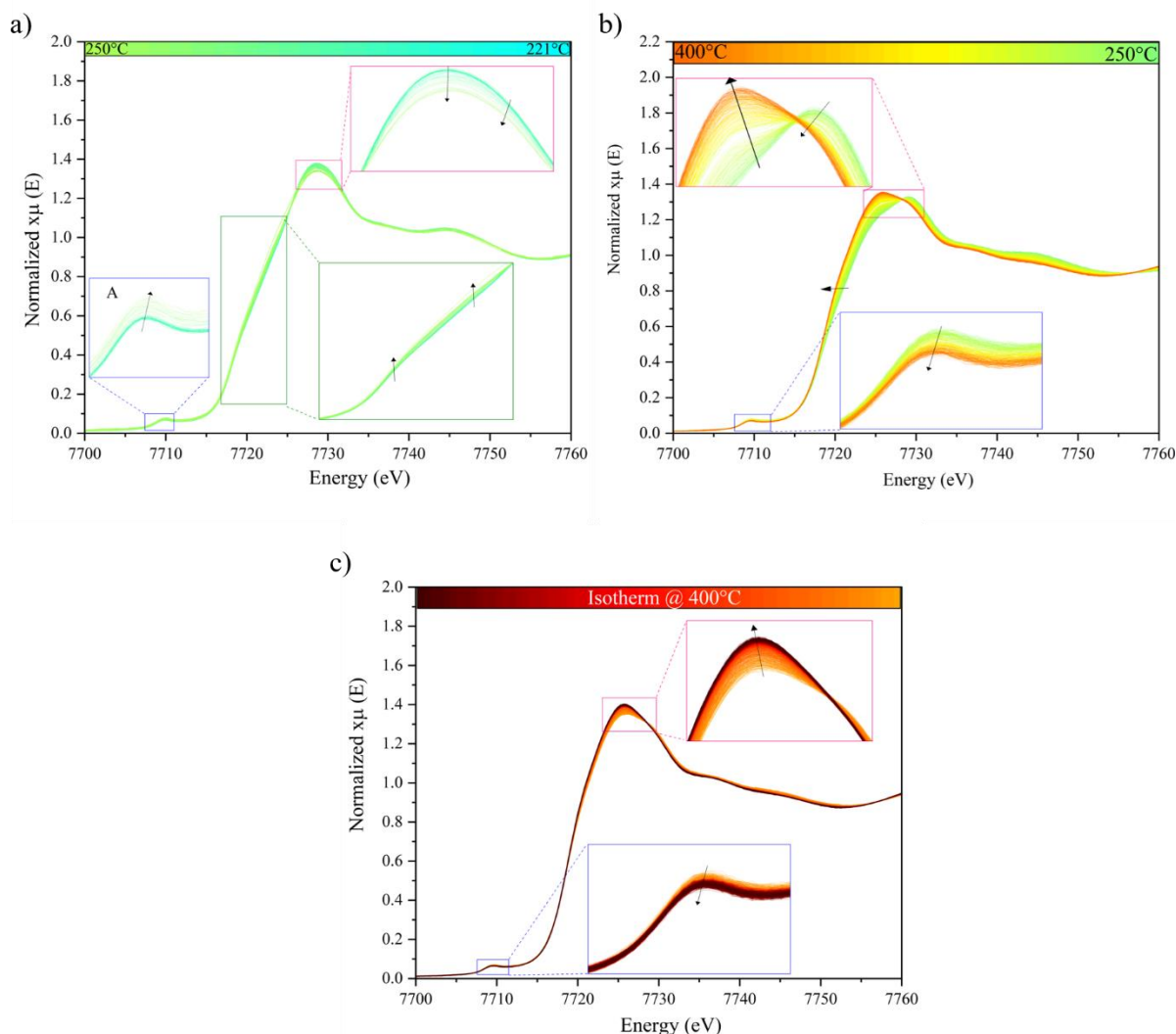


Figure II-22: XANES part of XAS spectra collected during the heat treatment of LiCoO_2 : KHSO_4 [1: 3] mixture **(a)** from 221°C to 250°C, **(b)** from 250 °C to 400°C, and **(c)** during the isotherm step.

II.5.3.6 Chemometric analysis:

To better understand the reaction mechanism, the XAS spectral evolution during the reaction was further exploited using chemometric methods allowing (i) the determination of the number of species involved in the reaction, (ii) the concentration evolution and XAS spectra of each species and (iii) the identification of the species.

A principal component analysis (PCA) of the *in situ* XAS data was first performed to assess the number of independently varying components involved during the reaction⁸⁴. This multivariable statistical method allows treating a large set of volume data without any prior consideration of structural models. The so-called scree plot displaying the eigenvalues determined by Singular Value Decomposition (SVD) (**Figure II-23**), yielded four components allowing to explain most of the variance of the data set.

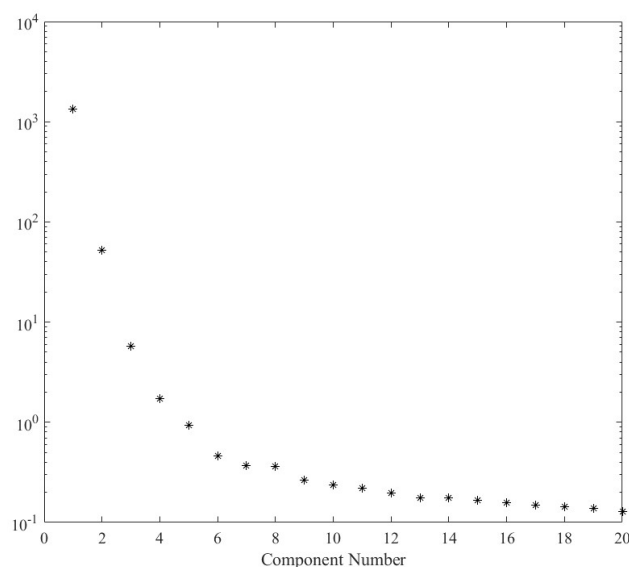


Figure II-23: Scree plot of eigenvalues determined by SVD.

The Multivariate Curve Resolution with Alternating Least Square (MCR-ALS) fitting analysis was subsequently used to assess the XAS spectra (**Figure II-24**) of the four MCR components (hereafter denoted MCR-Cp) involved during the reaction including the starting LiCoO_2 and the end product $\text{K}_2\text{Co}_2(\text{SO}_4)_3$. The second and third components were assigned to $\text{H}_x\text{Li}_{1-x}\text{CoO}_2$ (MCR-Cp2) and $\text{Co}_3(\text{SO}_4)_2(\text{OH})_2$ (MCR-Cp3) according to the *ex situ* XRD result. **Figure II-24** shows the XANES part of XAS spectra of the four components. The edge absorption shifts progressively to lower energies from MCR-Cp1 to MCR-Cp4, consistent with reduction of Co^{III} . In addition, intensity of the edge peaks decreases due to distortion of CoO_6 octahedra.

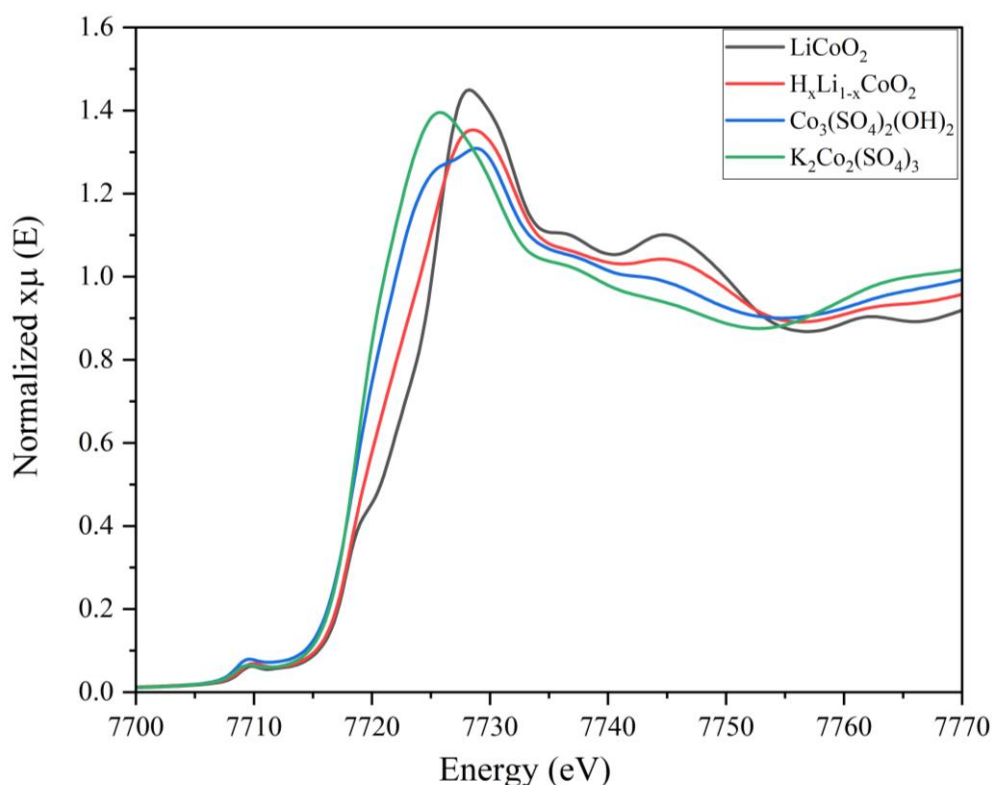


Figure II-24: The evolution of Co K-edge XANES spectra for the four components.

To ensure the reliability of the MCR-ALS method, the XANES and EXAFS spectra of the four components were investigated. **Figure II-25** shows the Fourier transformation of the k^3 weighted EXAFS oscillations $|\chi(R)|$ of MCR-Cp2 and MCR-Cp1 which is LiCoO_2 . The first peak assigned to Co-O distance within CoO_6 polyhedral is much broader and has lower intensity in $\text{H}_x\text{Li}_{1-x}\text{CoO}_2$ compared to LiCoO_2 , agreeing with the higher atomic disorder on Co-O environment in $\text{H}_x\text{Li}_{1-x}\text{CoO}_2$. To better assess these changes, the refinement of the EXAFS oscillations of LiCoO_2 and $\text{Li}_{1-x}\text{CoO}_2$ were carried out. **Figure II-26** shows the $|\chi(R)|$ and their refinement for MCR-Cp2 and LiCoO_2 . For LiCoO_2 , the first peak of $|\chi(R)|$ corresponds to six Co-O (1.91\AA) distances and the second peak represents six Co-Co (2.82\AA) and six Co-Li (2.85\AA) distances. To refine the EXAFS oscillations of $\text{H}_x\text{Li}_{1-x}\text{CoO}_2$, first the LiCoO_2 structure was considered. The first peak was refined in the beginning by six oxygen atoms at equivalent distance, but, the resulted refinement does not reproduce the experimental data with $R=0.033$ (**Figure II-27.a**). Thus, to obtain a good fit a distortion on the cobalt octahedra with the occurrence of two Co-O distances was introduced, the obtained R-factor is small 0.00784 confirming the good quality of the fit (**Figure II-27.b**). **Table II-11** list the XAS refinement result of LiCoO_2 and $\text{H}_x\text{Li}_{1-x}\text{CoO}_2$ spectra and **Table II-12** list the XAS refinement result of MCR-Cp1 with regular CoO_6 and with distortion of two Co-O distances.

The refined EXAFS of the second component evidenced a distortion of the cobalt coordination mode. Such a distortion is, however, averaged by the MCR-ALS method which should precludes the use of the determination of concentration profile.

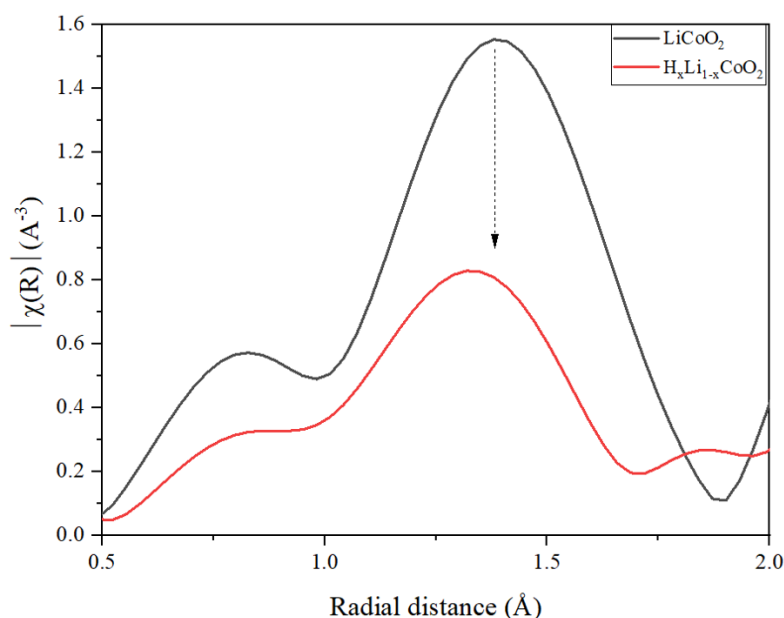


Figure II-25: Magnitude of Fourier transformation of k^3 weighted EXAFS oscillations for MCR-Cp (LiCoO_2) and MCR-Cp2 ($\text{Li}_{1-x}\text{CoO}_2$).

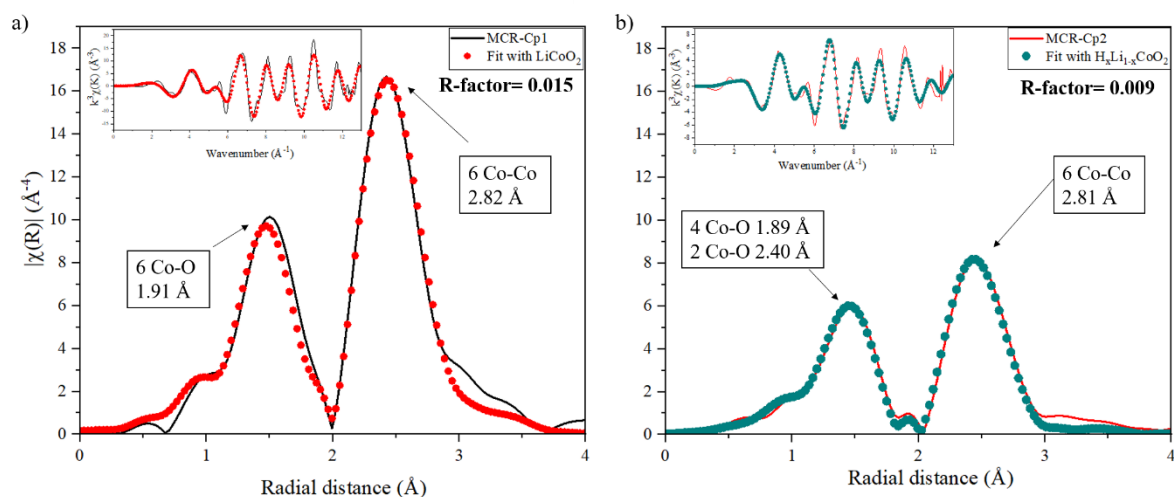


Figure II-26: Magnitude of Fourier transformation of k^3 weighted EXAFS oscillations for (a) MCR-Cp1 (LiCoO_2) and (b) MCR-Cp2 ($\text{Li}_{1-x}\text{CoO}_2$). Insets show the quality of fit in k-space.

Table II-11: Structural parameters of LiCoO_2 and $\text{Li}_{1-x}\text{CoO}_2$ obtained from refinement of EXAFS oscillation of MCR-Cp1 and MCR-Cp2.

Components	name	N	σ^2	E_0	R ref	R
MCR-Cp1 LiCoO_2	Co-O	6	0.00273	-5.318	1.92	1.91
	Co-Co	6	0.00205	-5.318	2.82	2.82
MCR-Cp2 $\text{Li}_{1-x}\text{CoO}_2$	Co- O	4	0.00448	-1.847	1.92	1.89
	Co- O	2	0.01381	-1.847	1.92	2.40
	Co- Co	6	0.00736	-1.847	2.81	2.81

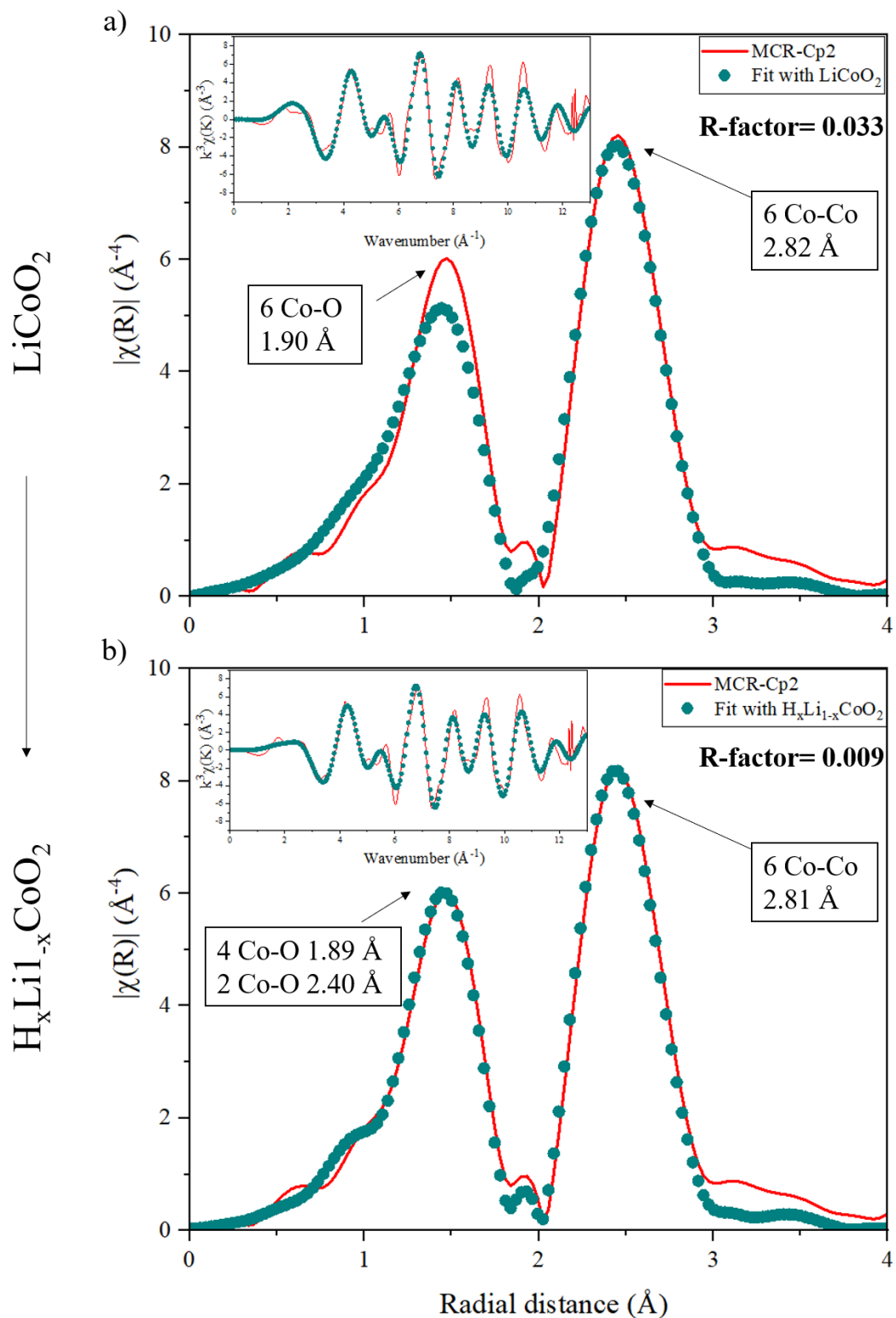


Figure II-27: Magnitude of Fourier transformation of k^3 weighted EXAFS oscillations for MCR-Cp2 refined with (a) regular CoO_6 octahedra and (b) distortion two Co-O distances. Insets show the quality of fit in k -space.

Table II-12: Results of refinement of the EXAFS oscillations for MCR-Cp2 with regular CoO_6 octahedra and distortion two Co-O distances.

	Name	N	σ^2	E_0	R ref	R
MCR-Cp2	Co- O	6	0.01048	-0.186	1.92	1.90
	Co- Co	6	0.00742	-0.186	2.82	2.82
MCR-Cp2	Co- O	4	0.00448	-1.847	1.92	1.89
	Co- O	2	0.01381	-1.847	1.92	2.40
	Co- Co	6	0.00736	-1.847	2.81	2.81

To confirm the assignment of the MCR-Cp3 to $\text{Co}_3(\text{SO}_4)_2(\text{OH})_2$, the EXAFS oscillations data were refined. The refinement results **Figure II-28** confirms the formation of hydroxide cobalt phase. As $\text{Co}_3(\text{SO}_4)_2(\text{OH})_2$ contain partial occupancy on cobalt, to run FEFF calculate it was mandatory to create new CIF without partial occupancy on cobalt. The calculated data with $\text{Co}_3(\text{SO}_4)_2(\text{OH})_2$ reproduce well the experimental data ($R=$). **Table II-13** list the structural parameters of $\text{Co}_3(\text{SO}_4)_2(\text{OH})_2$ obtained from EXAFS refinement of MCR-Cp3. The σ^2 of Co-O (0.00716) is higher compared to that obtained for LiCoO_2 (0.00273) and MCR-Cp2 (0.00441) due to the temperature effect. However, the obtained Co-O are slightly different from those of the $\text{Co}_3(\text{SO}_4)_2(\text{OH})_2$ reference. This can be related to the temperature effect. Indeed, σ^2 and the R (interatomic distance) parameters are correlated.

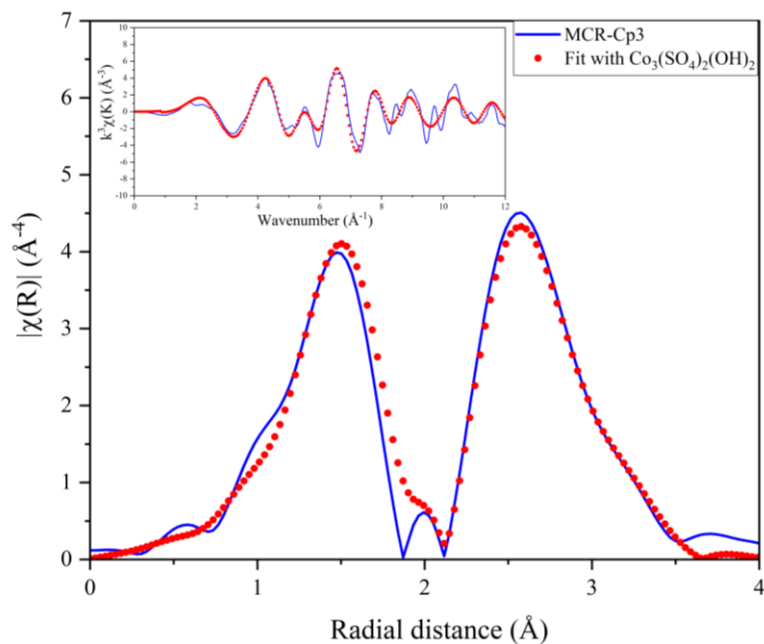


Figure II-28: Magnitude of Fourier transforms of k^3 weighted EXAFS oscillations for the MCR-Cp3 along with fitting result. Insets show the quality of fit in k -space.

Table II-13: Structural parameters for $\text{Co}_3(\text{SO}_4)_2(\text{OH})_2$ obtained from EXAFS refinement of MCR-Cp3.

Component	Name	N	S_0^2	σ^2	E0	R ref	R
$\text{Co}_3(\text{SO}_4)_2(\text{OH})_2$	Co- O	2	0.610	0.00416	-1.252	2.08	1.99
	Co- O	4	0.610	0.01920	-1.252	2.12	2.03
	Co- Co	2	0.610	0.00373	-1.252	2.65	2.87
	Co- S	4	0.610	0.00687	-1.252	3.37	3.21
	Co-O-Co	8	0.610	0.00115	-1.252	3.44	3.32
	Co-O-S	8	0.610	0.00115	-1.252	3.47	3.33
	Co-O ₂	4	0.610	0.00942	-1.252	3.71	3.39
	Co-Co ₂	2	0.610	0.00416	-1.252	2.08	1.98

In the same way, the MCR-Cp4 was refined with $K_2Co_2(SO_4)_3$. During the refinement only one site of cobalt was considered. **Figure II-29** shows the obtained refinement. The refinement was difficult due to impact of high temperature. The obtained R-factor was 0.03119. In addition, the Co-O distance (2\AA) are lower to those of $K_2Co_2(SO_4)_3$ crystal. The obtained results are listed in **Table II-14**. To confirm the formation of $K_2Co_2(SO_4)_3$, the XRD analysis was performed on the product recovered after XAS analysis (**Fig.A. 2**). The XRD confirm the conversion of $LiCoO_2$ into $K_2Co_2(SO_4)_3$. Nevertheless, the XRD shows further the formation of Co_3O_4 . This latter can be related to the incomplete conversion because of short reaction time (2h instead of 4h).

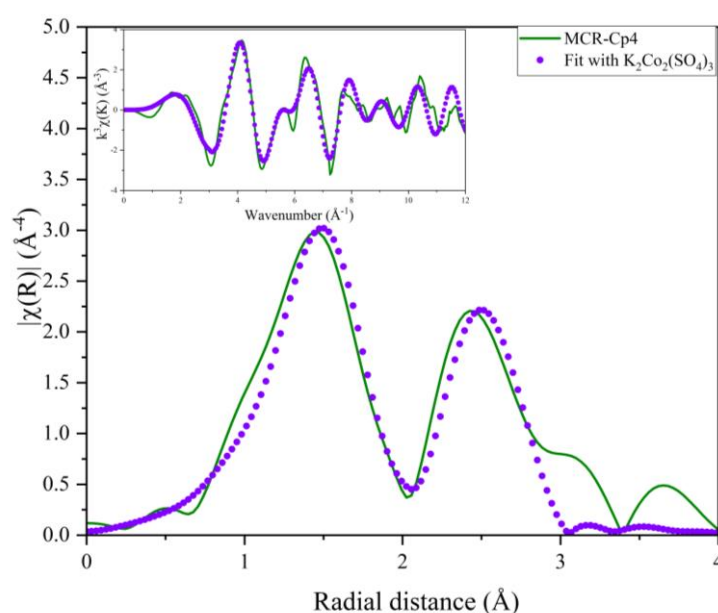


Figure II-29: Magnitude of Fourier transforms of k^3 weighted EXAFS oscillations for the MCR-Cp4 along with fitting result. Insets show the quality of fit in k-space.

Table II-14: Structural parameters for $K_2Co_2(SO_4)_3$ obtained from EXAFS refinement of MCR-Cp4.

Component	Name	N	σ^2	E_0	R reference	R
$K_2Co_2(SO_4)_3$	Co- O	3	0.01050	-1.727	2.079	1.99
	Co- S	1.5	0.00168	-1.727	3.379	3.50
	Co- O	3	0.01608	-1.727	2.090	2.01
	Co- S	1.5	0.00177	-1.727	3.214	2.99

Overall, x-ray absorption spectroscopy enabled to better capture the structural features induced by the Li^+/H^+ ionic exchange reaction between LiCoO_2 and KHSO_4 . The formation of a solid solution $\text{H}_x\text{Li}_{1-x}\text{CoO}_2$ was characterized by the distortion of the local environment of cobalt, which can be primarily assigned to the formation of hydroxyl groups. The temperature range of existence of the solid solution, however, extends to the melting of KHSO_4 adding to the complexity of the reaction pathway. The dynamic of the structural features of $\text{H}_x\text{Li}_{1-x}\text{CoO}_2$ limits the use of the MCR-ALS method, particularly the evolution of the concentration profile of each component. It has, nevertheless, enabled to confirm the involvement of a hydroxide-sulfate phase.

To better understand the ionic exchange between LiCoO_2 and KHSO_4 , DFT-calculations were considered, as shown in the next section.

II.6 DFT-calculations

To understand the reaction mechanism of LiCoO_2 with KHSO_4 , electronic structure calculations based on density functional theory (DFT) were performed with the collaboration of ICGM (Marie-Liesse Doublet and Clara Robert). The aim of this theoretical study was to investigate the impact of the Li^+/H^+ substitution on the crystal and the electronic structure of the $\text{Li}_{1-x}\text{H}_x\text{CoO}_2$ phases. The results are compared with previous XRD and spectroscopic (XAS) data. The calculations were performed with the VASP calculation code^{85,86} using PAW pseudopotentials⁸⁷ and the PBE exchange and correlation functional⁸⁸. The DFT+U formalism as developed by Dudarev⁸⁹ was then chosen to better describe the strongly correlated character of the 3d electrons of cobalt.

II.6.1 Electronic structure of LiCoO_2

According to the experiment, the LiCoO_2 phase is characterized by a diamagnetic electronic state. As shown in **Figure II-30**, the calculated spin-polarized density of states projected on Li, Co and O atoms exhibits a band gap around the Fermi level ($E_F = 0$ eV) and no spin polarization (DOS spin-up = DOS spin-down). The non-magnetic LiCoO_2 is confirmed for all $U(\text{Co})$ values ranging from 0 to 5 eV (**Table II-15**).

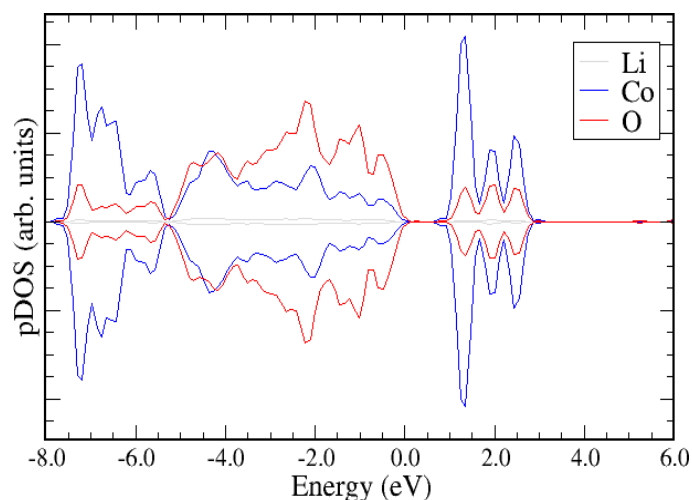


Figure II-30: Density of states calculated in DFT+U for a value of $U_{\text{eff}}(\text{Co}) = 4$ eV by imposing a total zero spin on the cell and projected on the Li, Co and O atoms (spin-up: positive pDOS; spin-down: negative pDOS).

Table II-15: Energy (E in eV per form unit) and local magnetic moment on Co^{III} ions ($\mu_{\text{B}}(\text{Co})$) calculated for the LiCoO_2 phase as a function of the value of U_{eff} used for cobalt and the magnetic arrangement considered (AFM: antiferromagnetic, FM: ferromagnetic, ND0: total zero spin imposed in the calculation).

S.G.	U_{eff} (eV)	Mag	E (eV/FU)	$\mu_{\text{B}}(\text{Co})$
R-3m	U2	AFM	-22.85698	3.026
R-3m	U2	FM	-22.74322	3.026
R-3m	U2	ND0	-23.49693	0
R-3m	U3	AFM	-22.57673	$3.075 \cdot 2 / 0.011$
R-3m	U3	FM	-22.46248	3.015
R-3m	U3	ND0	-22.92048	0
R-3m	U3.32	FM	-22.31942	3.094
R-3m	U3.32	ND0	-22.74067	0
R-3m	U4	FM	-22.09679	3.128
R-3m	U4	ND0	-22.36536	0

II.6.2 Substitutions Li^+/H^+

To understand the structural features of the observed solid solution $\text{H}_x\text{Li}_{1-x}\text{CoO}_2$, H^+/Li^+ substitutions were studied in a super cell consisting of 12 or 24 lithium atoms, and for H ratio of 1 to 4 for 12 Li. Later, these compositions will be noted as $n\text{H}/(12-n)$ Li. Different H/Li distributions were also considered depending on whether hydrogen atoms replace lithium atoms, from the same layer (Alt structures) or from different layers (Mix structures). As shown in **Figure II-31** on the 2H/10Li example, Alt substitutions (**Figure II-31.a**) lead to a migration of adjacent Li^+ ions from their initial octahedral site to the nearest tetrahedral site of the layer. In Mix structures (**Figure II-31.b**), Li^+ ions move from their initial octahedral site to a distorted LiO_5 environment with loss of a Li-O interaction. Whatever the substitution rate, the Mix structures show a slightly higher thermodynamic stability than the Alt structures, even if the energy gap between the two types of structures remains small (a few tens of meV per form unit).

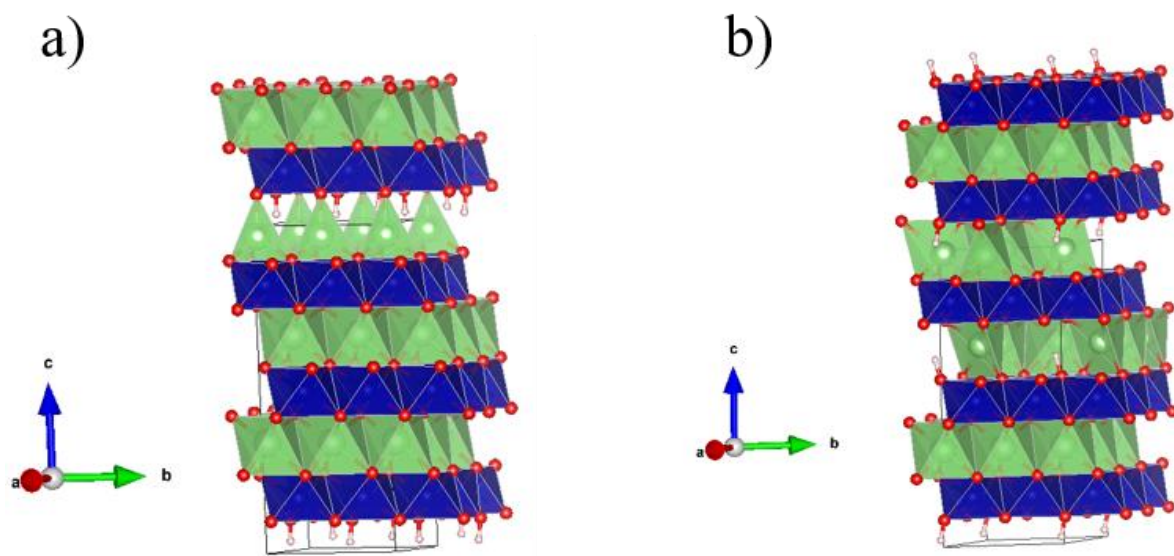


Figure II-31: Relaxed structures for a H^+/Li^+ substitution rate of 2H/12Li considering different distributions: **(a)** the two H substitute Li from different layers: Alt structure. **(b)** the two H substitute Li from the same layer: Mix. In this case, the Li present in the substituted layer migrate to the tetrahedral site.

As expected, the H^+/Li^+ substitution leads to the formation of a hydroxyl ligand $-\text{OH}-$ that coordinates to the transition metal, in contrast to Li^+ ions that are not bonded to the metal. Since each oxygen is connected to three Co^{III} metals in the starting LiCoO_2 structure, thus, the formation of O-H covalent bonds leads to local symmetry breaking around the hydroxyl ion as

shown in **Figure II-32**. An inductive effect of hydrogen on the Co-O interaction then induced an elongation of the bond and an oxidation of the Co^{III} ion, confirmed by the calculations.

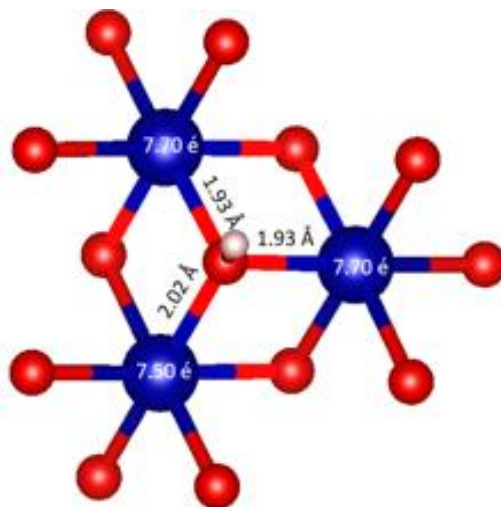


Figure II-32: Representation of the local environment of the hydroxyl ion in the 2H/10Li Mix-type structure showing the Co-OH bond distances and the Bader electron population per Co²⁺ ion. The elongation of one of the three Co-OH bonds is associated with an oxidation of the metal, in accordance with the inductive effect created by the formation of an O-H covalent bond that weakens the Co-O bond.

It is interesting to notice that for H⁺/Li⁺ compositions higher than 2H/10Li, some configurations lead to the spontaneous formation of water molecules in the structure upon structural relaxation. These structures, of which an example is given in **Figure II-33**, are mainly obtained when hydrogen atoms are substituted to Li in the same layer (Alt type), *i.e.* when the hydrogen content in the same layer is high. While some of these molecules seem to be completely disconnected from the host structure (**Figure II-33.a**), and therefore not very involved in the thermodynamic stability of the host structure, the structural relaxations performed on the dehydrated phases show an important structural reorganization with in particular a partial migration of the Co^{II} ions in the layers from which the water molecules have been extracted. For all these structures, the dehydration enthalpy is very favorable, demonstrating the ability of H_xLi_{1-x}CoO₂ structures to dehydrate. Nevertheless, the formation of water in the medium does not seem to be a thermally activated process since our DFT calculations at T=0K allow us to observe it spontaneously under certain conditions: when the rate of H per sheet is higher than the rate of Li and when the hydrogen atoms are placed on neighboring prime sites. Thus, we believe that the temperature has the effect of promoting the diffusion of hydrogens in these structures via a

thermally activated O-H---O O---H-O exchange mechanism and of creating the necessary conditions to stabilize water molecules and dehydrate the starting phase.

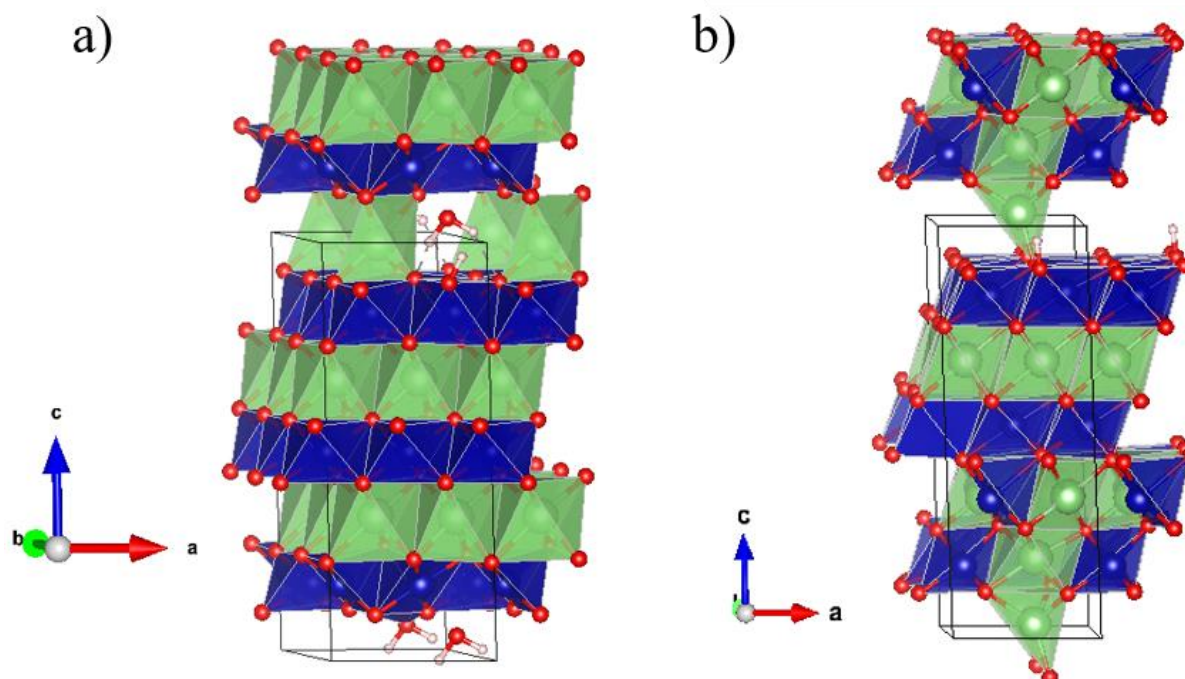


Figure II-33: (a) Structure of the relaxed phase of composition $\text{H}_{0.25}\text{Li}_{0.75}\text{CoO}_2$ showing the spontaneous formation of a water molecule in the Li/H interlayer. (b) Relaxed structure of the phase after release of a water molecule showing a strong reorganization of the structure with the migration of a cobalt in the interlayer space.

The electronic structure study of the hydrated and dehydrated phases (cf. **Figure II-34**) shows a notable modification of the density of states above the Fermi level which is expected to allow the interpretation of the changes observed in the XAS spectra as a function of temperature, in particular on the intensity ratios of the different XAS peaks. A study is in progress to simulate the theoretical spectra on the different structures obtained and to compare them with our experimental results.

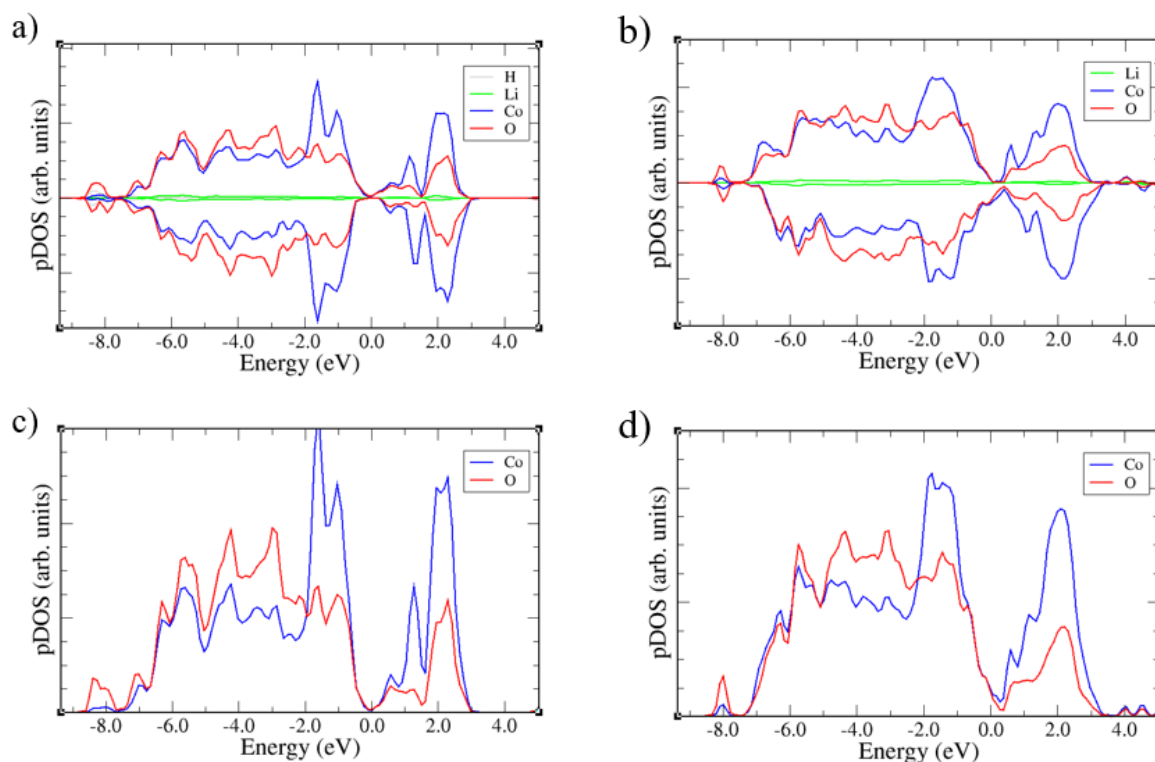


Figure II-34: Spin-polarized (a-b) and non-polarized (c-d) densities of states of the hydrated $\text{H}_{3/12}\text{Li}_{9/12}\text{CoO}_2$ phase (a and c) and its dehydrated counterpart (b and d) corresponding to the structures shown **Figure II-33**. Li and H are not shown on the spin-unpolarized pDOS (unnecessary).

II.7 Conclusion

In this chapter, we have demonstrated the recycling of positive electrode material of spent Li-ion batterie using molten salt KHSO_4 . The solid-state reaction between LMO and KHSO_4 lead the formation of soluble sulfate product KLiSO_4 , K_2SO_4 and langbeinite $\text{K}_2\text{M}_2(\text{SO}_4)_3$. ($\text{M} = \text{Co}$, Ni , Mn).

Firstly, the effect of the reaction parameters such as temperature, molar ratio, and atmosphere on the sulfation process were studied. For LiCoO_2 , the suitable conditions are: the temperature of $400\text{ }^\circ\text{C}$, molar ratio $\text{LiCoO}_2 : \text{KHSO}_4$ (1: 3), and air or argon atmospheres. These conditions were then applied for NMC and NCA materials. Thus, the reaction of NMC and NCA with KHSO_4 yielding formation of KLiSO_4 , K_2SO_4 and solid solution $\text{K}_2\text{Ni}_{0.33}\text{Co}_{0.33}\text{Mn}_{0.33}(\text{SO}_4)_3$ (in case of NMC) and $\text{K}_2\text{Ni}_{0.83}\text{Co}_{0.15}\text{Al}_{0.33}(\text{SO}_4)_3$ (in case of NCA). The sulfate products are soluble in water, thereby, water leaching process can be performed to recovers targeted elements such as Li, Co, Ni.

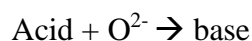
Thereafter, the sulfation reaction mechanism was investigated, by coupling variable-temperature XRD, XAS, and DFT results. The variable-temperature XRD results reveal presence of an ionic H^+/Li^+ exchange leading formation of $K_4LiH_3(SO_4)_4$ and $H_xLi_{1-x}CoO_2$ as intermediate phase. The refinement of EXAFS oscillations reveals that the ionic exchange induce change in the local environment of Co. Indeed, the refinement of EXAFS oscillations indicate elongation of two Co-O distances (2.40 Å). The DFT calculation confirms that $H_xLi_{1-x}CoO_2$ is thermodynamically favorable and the formed OH bond cause an elongation of Co-O bonds. At higher H^+/Li^+ substitution, water molecules are spontaneously formed. Due to temperature effect, the $H_xLi_{1-x}CoO_2$ dehydrated yielding formation of reactive Co^{2+} site, allowing the formation of $Co_3(SO_4)_2(OH)_2$. Further heating, $Co_3(SO_4)_2(OH)_2$ is converted to $K_2Co_2(SO_4)_3$.

Chapter III. Lux-Flood concept applied to sulfation of lithiated transition metal oxides

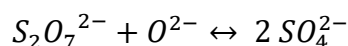
III.1 Introduction

In the scope of dissolution of ore to extract valuable metals, potassium pyrosulfate ($K_2S_2O_7$) has been investigated for its ability to solubilize a wide variety of compounds⁹⁰⁻⁹⁴. The dissolutions of ores were performed in excess of solvent $K_2S_2O_7$, at temperature higher than its melting point ($T_m=400^\circ C$). The reaction of $S_2O_7^{2-}$ with oxides (MO_x) occurs according to the acid-base Lux-Flood theory^{6,7}, in which the acid is an O^{2-} acceptor (oxoacid) and the base is the O^{2-} donor (**Equation III-1**). Thus, the $S_2O_7^{2-}$ are oxoacid with ability to accept O^{2-} from MO_x , result in: (i) the formation of K_2SO_4 and $M(SO_4)$ (**Equation III-2** and **Equation III-3**). Or (ii) the formation of double salt $K_xM_y(SO_4)_z$. For example, Berg *et al*⁹¹ showed that the dissolution of ZnO in $K_2S_2O_7$ leads the formation of $K_2Zn(SO_4)_2$ compound.

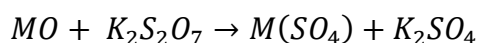
Equation III-1



Equation III-2:

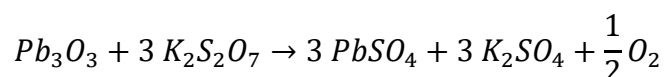


Equation III-3



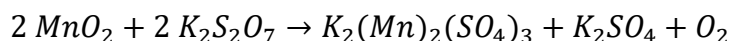
Moreover, in some cases, a reaction of an oxide with $K_2S_2O_7$ solvent is accompanied by reduction of transition metal e.g. reaction of Pb_3O_4 with $K_2S_2O_7$ yielded to $PbSO_4$ ⁹⁵, reaction equation is as follow:

Equation III-4:



Other studies have demonstrated the solid-state reaction between the transition metal oxide (MO_x) and $\text{K}_2\text{S}_2\text{O}_7$ in stoichiometric quantities. Guo *et al.*⁹⁴ investigate the $\text{K}_2\text{S}_2\text{O}_7$ calcining method to extract alumina from coal fly ash (CFA), they explained that the reaction of $\text{K}_2\text{S}_2\text{O}_7$: Al_2O_3 (3.55:1) at $T > 220^\circ\text{C}$ for 3h yielding the formation of double salt $\text{K}_3\text{Al}(\text{SO}_4)_3$. Also, Al-Shukry *et al.*⁹² reported the reduction of Mn^{VI} (MnO_2) to Mn^{II} stabilized in $\text{K}_2\text{Mn}_2(\text{SO}_4)_3$, upon its reaction with $\text{K}_2\text{S}_2\text{O}_7$ (**Equation III-5**).

Equation III-5:



Following the above approach, in this study, the $\text{K}_2\text{S}_2\text{O}_7$ will be used to convert the lithiated transition metal oxide LMO ($\text{M}=\text{Co}$) into soluble sulfate product through the solid-state reaction (sulfation reaction). First, the sulfation conditions including: (i) molar ratio LiCoO_2 : $\text{K}_2\text{S}_2\text{O}_7$ (ii) annealing temperature, and (iii) atmosphere are optimized. The results and key points of the impact of the synthesis parameters has been summarized below. Thereafter, the reaction mechanism has been toughly investigated.



- 1- Determination of the reaction conditions
- 2- Investigation of reaction mechanism involved during the sulfation of LiCoO_2 , using:
 - (i) Variable temperature XRD
 - (ii) X-ray absorption spectroscopy (XAS)

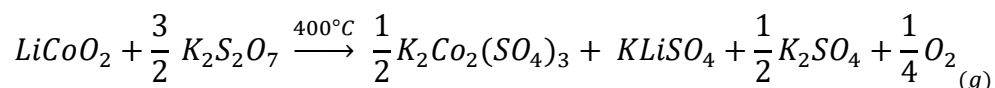
III.2 Reaction conditions

The reactivity of $K_2S_2O_7$ with lithiated transition metal oxide was investigated by tuning different parameters including the annealing temperature, the molar ratio of $K_2S_2O_7$: LMO, the atmosphere. These parameters were tuned in seeking completion of the sulfation of $LiCoO_2$ as a case study. The experimental procedures are detailed below.

- Synthesis temperature: Differential scanning calorimetry (**Figure III-1.a**) performed on $K_2S_2O_7$ shows that it melts at $418^\circ C$. Such value is in good agreement with literature⁵, though a spread of the melting point⁹⁶ has been observed probably due to the hygroscopic nature of this compound. In addition, TGA coupled MS revealed that the melting is accompanied with a slight decomposition with the detection of SO_3 at $415^\circ C$ (**Figure III-1.b**). The reaction temperature was set to $400^\circ C$ to ensure the complete sulfation reaction of $LiCoO_2$.
- Due to the high hygroscopicity of $K_2S_2O_7$ ⁹⁷ the argon atmosphere was selected to carry out the sulfation process.
- To determine the molar ratio, mixture of $K_2S_2O_7$ and $LiCoO_2$ of [n: 1] with n vary from 1 to 2 mol have been treated at $400^\circ C$ under argon atmosphere. **Figure III-2.a** shows the evolution of XRD patterns of sulfation product as function of molar ratio. When ratio of $LiCoO_2$: $K_2S_2O_7$ was [1:1], the diffraction peaks of $KLiSO_4$, K_2SO_4 , and $K_2Co_2(SO_4)_3$ were detected. Likewise, the XRD patterns shows the formation of Co_3O_4 indicating an incomplete sulfation. When molar amount of $K_2S_2O_7$ increase continuously, the diffraction peaks of Co_3O_4 decrease gradually, indicating that the excess of $K_2S_2O_7$ react with Co_3O_4 to form $K_2Co_2(SO_4)_3$, the optimal molar ratio of $LiCoO_2$: $K_2S_2O_7$ was set to [1:1.5].

According to Rietveld analysis (**Figure III-2.b**) of the sample $LiCoO_2$: $K_2S_2O_7$ [1: 1.5] and the thermal analysis, the corresponding reaction was established:

Equation III-6



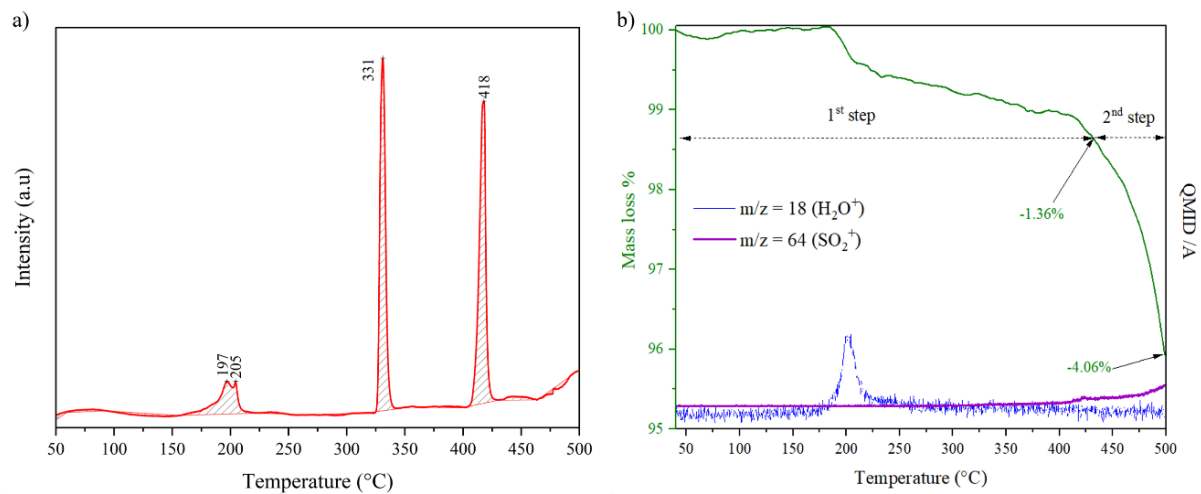


Figure III-1: Thermal analyses of $K_2S_2O_7$ a) Differential scanning calorimetry DSC b) Thermogravimetric analysis coupled with mass spectroscopy TGA-MS.

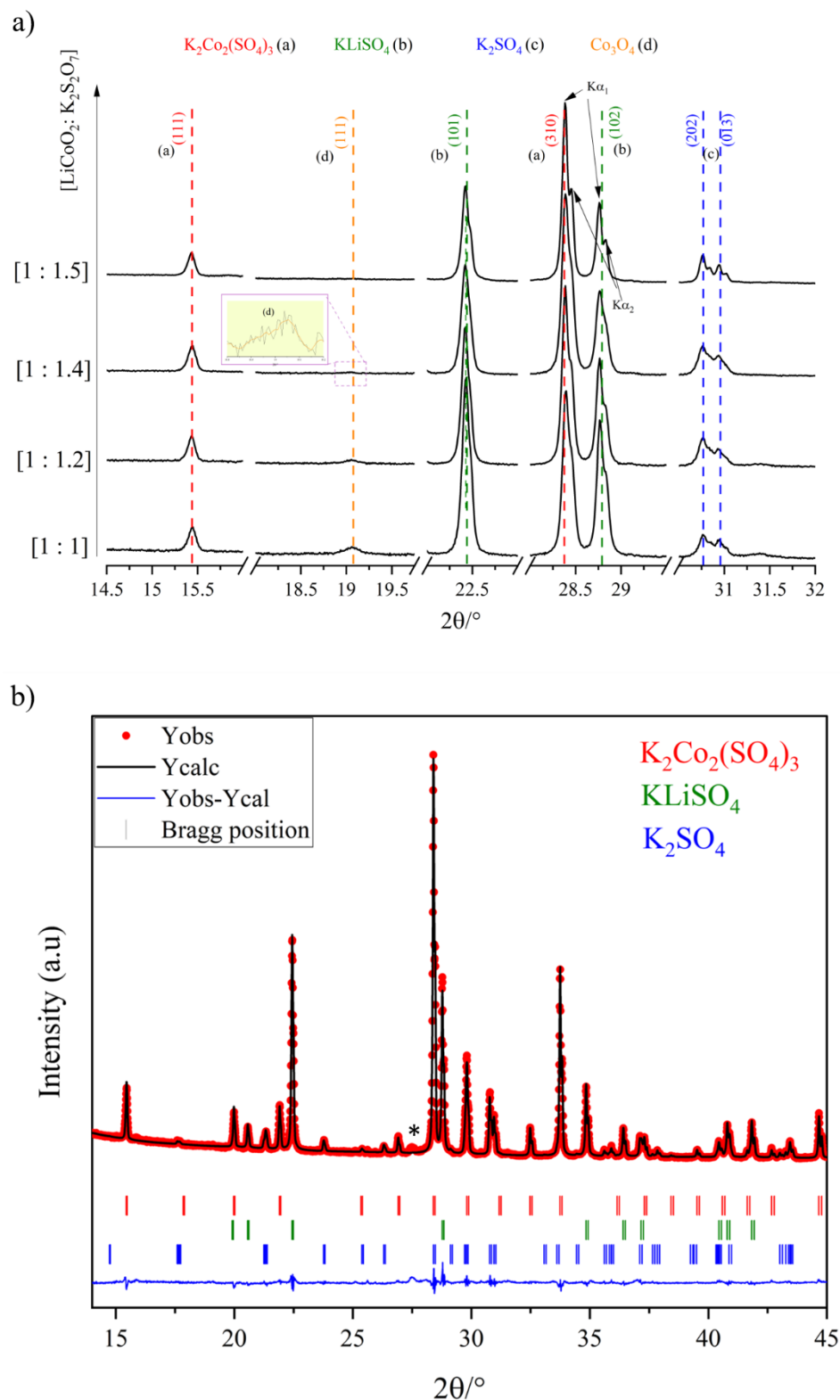


Figure III-2: a) evolution of XRD patterns of $\text{LiCoO}_2:\text{K}_2\text{S}_2\text{O}_7$ [1: n] as function of n. b) Rietveld refinement of $\text{LiCoO}_2:\text{K}_2\text{S}_2\text{O}_7$ [1: 1.5] heat treated at 400°C under argon atmosphere. * is impurity.

Table III-1: Result of the Rietveld refinement of the XRD pattern $\text{LiCoO}_2\text{:K}_2\text{S}_2\text{O}_7$ [1: 1.5] heat treated at 400°C under argon atmosphere.

Phases	a (Å)	b (Å)	c (Å)	Bragg R-factor%	wt. %
$\text{K}_2\text{Co}_2(\text{SO}_4)_3$	9.9314(1)	9.9314(1)	9.9314(1)	6.84	48.48(13)
KLiSO_4	5.1461(1)	5.1461(1)	8.6319(3)	6.73	33.52(11)
K_2SO_4	5.773(5)	10.076(3)	7.481(4)	12.9	18 (1)

III.3 From oxide to sulfate: transformation mechanism

III.3.1 Variable temperature XRD analysis

The phase evolution of mixture $\text{LiCoO}_2\text{:K}_2\text{S}_2\text{O}_7$ [1: 1.5] upon heating was first examined by variable-temperature X-ray diffraction. **Figure III-3** shows a contour-plot of the collected variable-temperature XRD patterns from RT to 400°C. Noticeable changes first occur at ~ 200°C, with the detection of KLiSO_4 compound (**Figure III-4.e**). Concomitantly, a small peak assigned to the (003) Bragg reflexion of the layered structure was detected at a lower 2θ value (~ 18.5° - 18.7°) then the pristine (18.85°-18.8°) as shown in **Figure III-4.d** and **Figure III-4.b**, respectively. This trend agrees with a delithiation process *i.e.* increase of c parameter due to repulsive effect of the facing oxide ions, and the formation of KLiSO_4 . Note that the latter implies the reaction with oxide ion to form sulfate from the peroxosulfate anion ($\text{S}_2\text{O}_7^{2-}$). Hence, it can be anticipated that the delithiation occurs via the concomitant O^{2-} ion diffusion from the layered structure according to $\text{Li}_{1-2x}\text{CoO}_{2-x}\square_x$, where \square represent a vacancy. Such a phase seems to be formed until around 280°C where it started to be transformed. From 280°C to 320°C, a Bragg peak characteristic of spinel Co_3O_4 was detected along with a net increase of the (101) peak of KLiSO_4 and the appearance of the phase $\text{K}_2\text{Co}_2(\text{SO}_4)_3$ (**Figure III-5**). Upon further heating, the expected phase KLiSO_4 , K_2SO_4 , and $\text{K}_2\text{Co}_2(\text{SO}_4)_3$ concomitantly growth (**Figure III-6**). Beyond 380°C, the XRD patterns feature diffuse scattering probably due to the progressive melting of $\text{K}_2\text{S}_2\text{O}_7$ preventing the analysis.

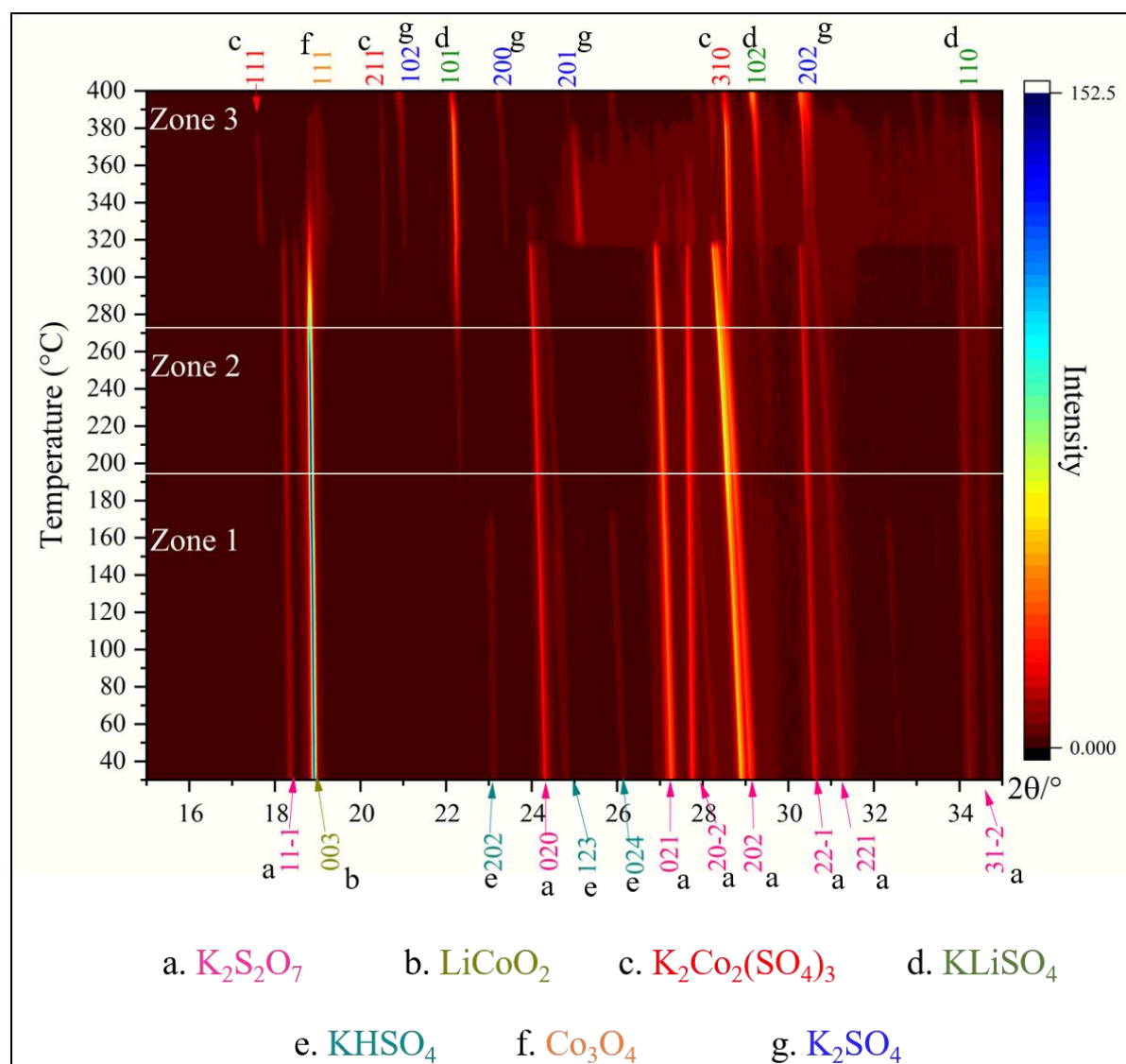


Figure III-3: Contour plot of the XRD patterns collected upon the sulfation of $LiCoO_2: K_2S_2O_7$ [1: 1.5], from 30°C to 400°C, with heating rate of 5 °C/min under argon atmosphere. Note that a small amount of $KHSO_4$ was detected at $\sim 23^\circ(2\theta)$ probably due to the water contamination occurring during the sample transfer.

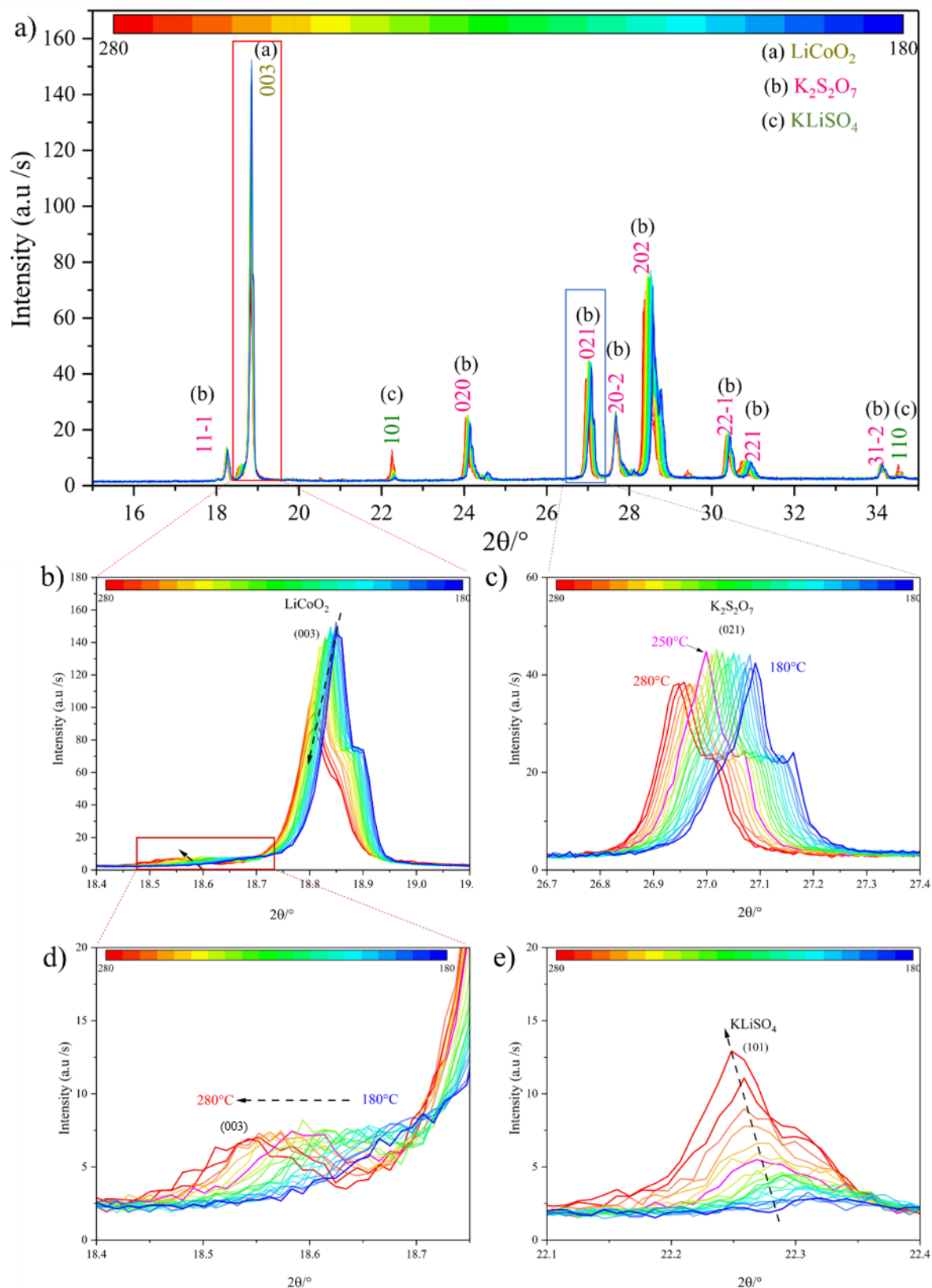


Figure III-4: a) XRD pattern collected from 180 °C to 280 °C. b) zoom on the main plan (003) of LiCoO_2 . c) evolution of (021) plan of $\text{K}_2\text{S}_2\text{O}_7$ as function of temperature. d) zoom on the formed $\text{Li}_{1-2x}\text{CoO}_{2-x}\square_x$ (18.5° - 18.7°). e) evolution of (101) plan of the formed KLiSO_4 .

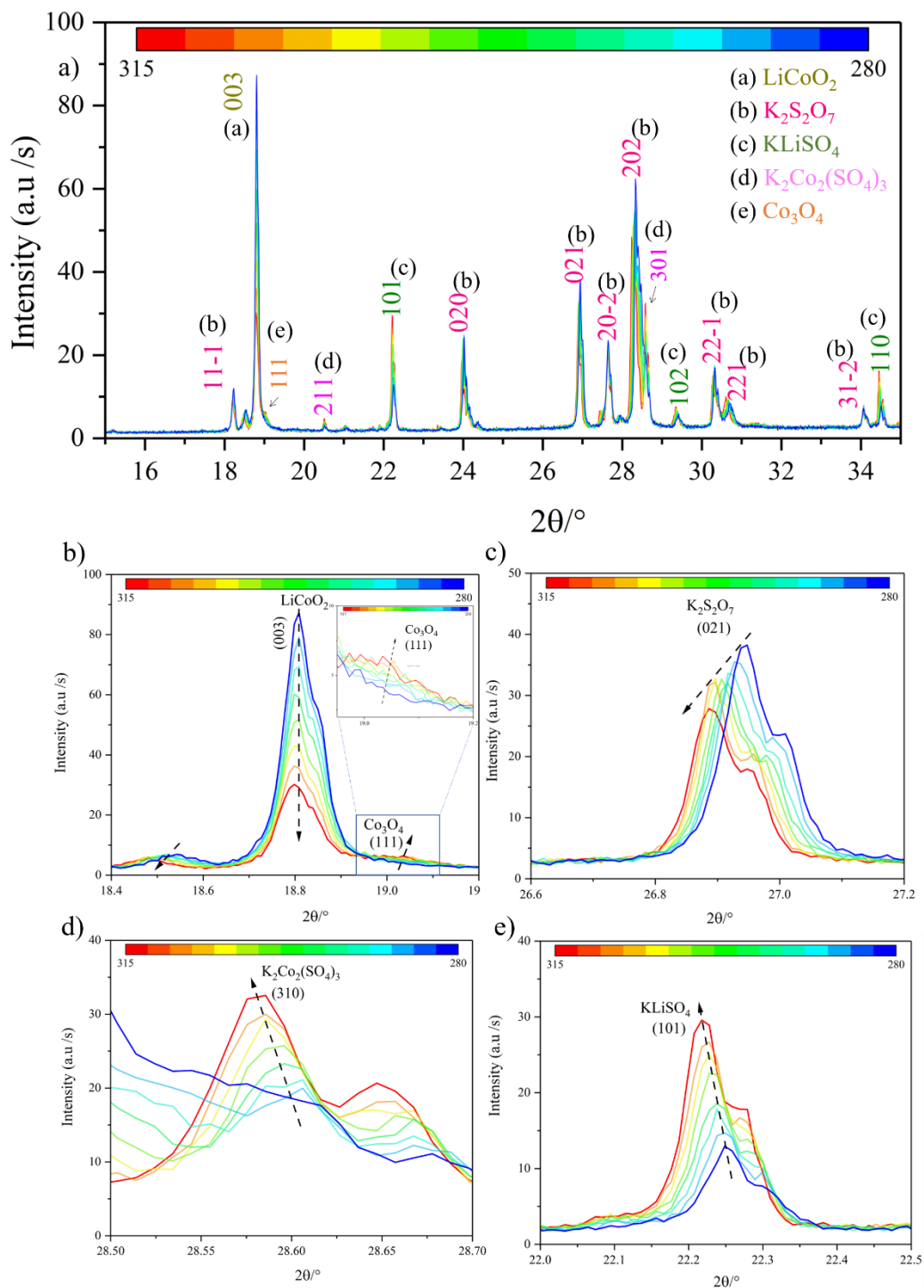


Figure III-5: **a)** XRD pattern collected from 280 °C to 315°C. **b)** zoom on the main plan (003) of LiCoO₂ and formed Co₃O₄. **c)** evolution of (021) plan of K₂S₂O₇ as function of temperature. **d)** Formation and evolution of K₂Co₂(SO₄)₃ peak at (28.55° -28.65°) corresponding to (310) plan. **e)** evolution of (101) plan of the formed KLiSO₄.

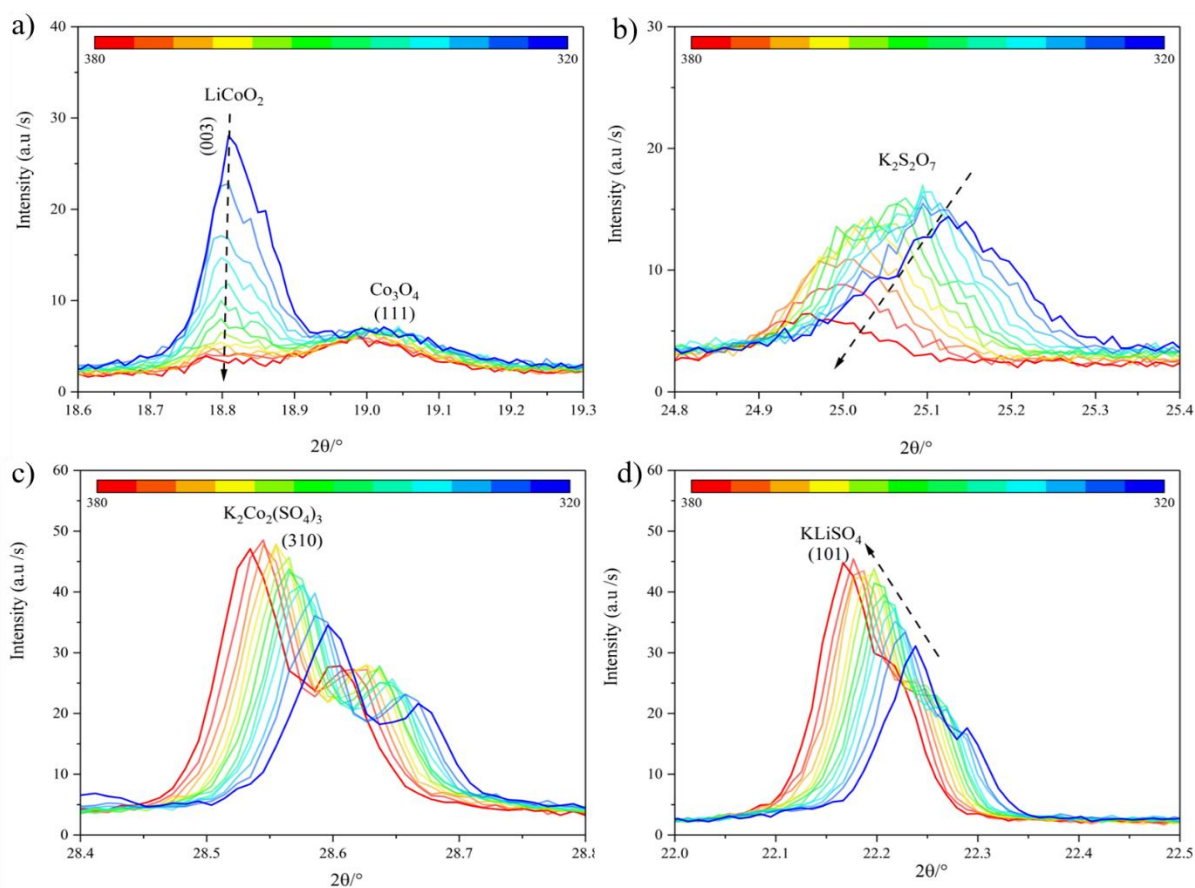


Figure III-6: Evolution of plan (a) (003) of LiCoO_2 and (111) of Co_3O_4 . b) $\text{K}_2\text{S}_2\text{O}_7$. c) $\text{K}_2\text{Co}_2(\text{SO}_4)_3$. and d) KLiSO_4 .

III.3.2 X-ray absorption spectroscopy

To clarify the phase evolution, controlled temperature X-ray absorption spectroscopy was performed at the Co K-edge, upon heating the sample from RT to 400°C , following by a plateau region. The collected XAS spectra were investigated to track the evolution of the electronic state of cobalt as well as its local structure.

III.3.2.1 Cobalt oxidation state

The collected XANES spectra during the heating and isotherm step are gathered in **Figure III-7.a**. The evolution of the spectra reveals a progressive shift of the absorption edge to lower energy by around 4 eV, consistent with reduction of Co^{III} to Co^{II} . Moreover, the evolution of edge peak situated at (7722 eV- 7734eV) was inspected. The energies of maximum of the absorption peaks were determined and represented in **Figure III-7.b** and **Figure III-7.c**. Upon

the heating (**Figure III-7.b**) the edge peaks shift slightly from 7728.2 to 7729.4 eV (+1.2 eV). However, when temperature was set at 400°C (**Figure III-7.c**), the peaks shift significantly to lower energies, *i.e.* from 7729.2 eV to 7726 eV (-3.2 eV). Hence signifying a reduction of Co^{III} to Co^{II} .

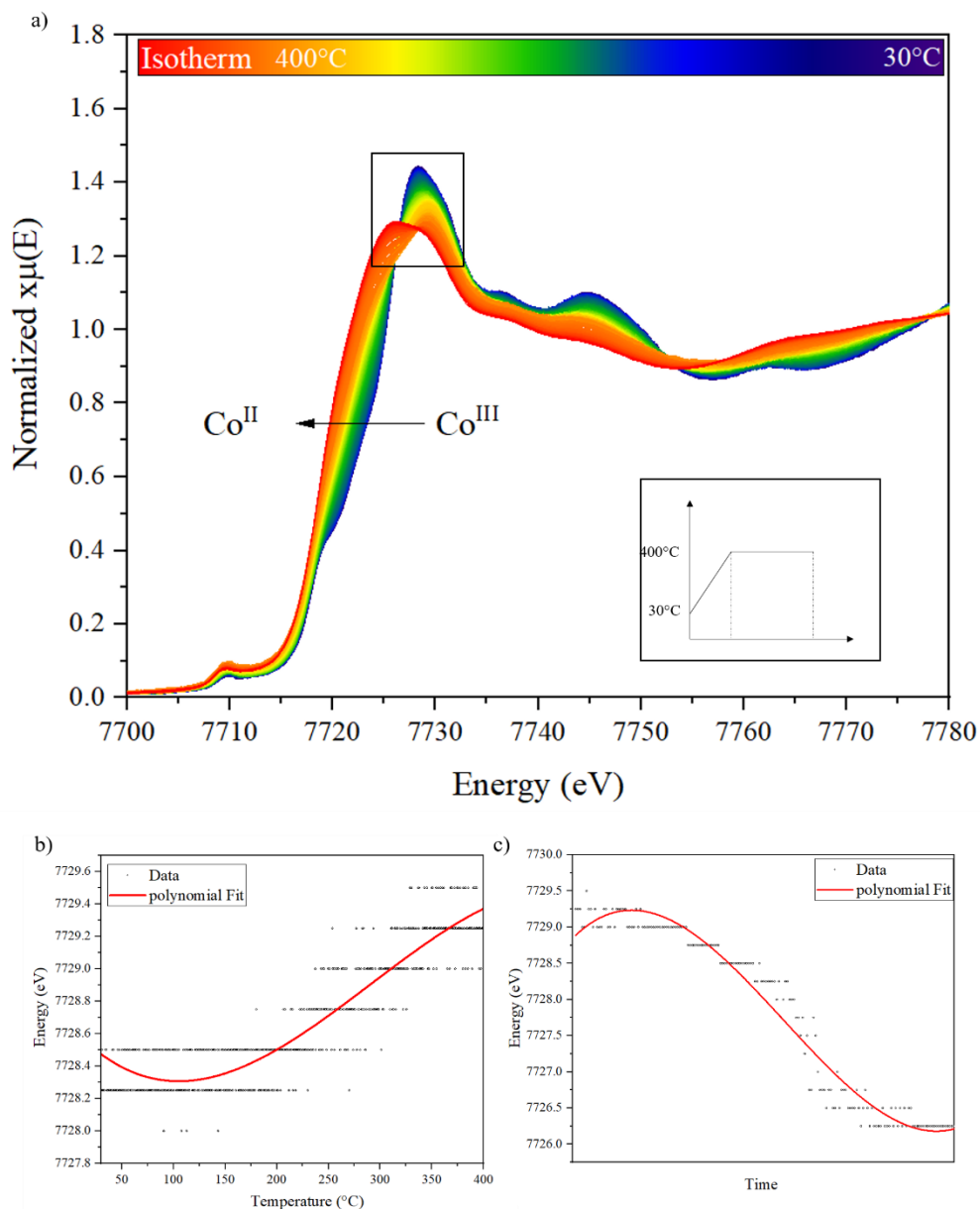


Figure III-7: **a)** XANES spectra collected during heat treatment of $\text{LiCoO}_2: \text{K}_2\text{S}_2\text{O}_7$ [1:1.5] mixture from RT to 400°C with 5°C/min. insets the heating profile. **b)** Evolution of energy value of edge peak obtained upon the heating of LiCoO_2 and $\text{K}_2\text{S}_2\text{O}_7$ mixture from RT to 400°C and during the isotherm step for 2h at 400°C **(c)**.

III.3.2.2 EXAFS analysis: phase evolution

The XAS spectra evolution was analyzed using the principal component analysis (PCA) along with Multivariate Curve Resolution-alternating Least Squares (MCR-ALS). Four components were identified (**Figure III-8**) and their corresponding Co K-edge XANES and magnitude of Fourier transformation (FT) of the EXAFS oscillation are presented in **Figure III-9.a** and **Figure III-9.b** respectively. The XANES region of the four component (**Figure III-9.a**) shows an edge shift to low energies upon the transition from MCR-Cp1 (LiCoO₂) to MCR-Cp4 across MCR-Cp2 and MCR-Cp3 respectively, consistent with reduction of Co. In addition, the intensities pre-edge increase from MCR-Cp1 (0.053) to MCR-Cp2 (0.065) to MCR-Cp3 (0.09) (figure inside **Figure III-9.a**). The significant increase on the pre-edge peak of the MCR-Cp3 result on the distortion of CoO₆ octahedral and an eventual formation of Co in tetrahedral symmetry. Further heating, the MCR-Cp4 with regular Co^{II}O₆ is formed.

Figure III-9.b show the magnitude of Fourier transformation (FT) of k³- weighted EXAFS oscillations $|\chi(R)|$. The $|\chi(R)|$ of the pristine LiCoO₂ has two peaks. The first one corresponds to CoO₆ octahedron *i.e.* Co is coordinated to six oxygen ($R_{\text{Co-O}} = 1.91 \text{ \AA}$), and the second peak corresponds to the second shell CoCo₆ and CoLi₆. The heating of LiCoO₂: K₂S₂O₇ [1:1.5] leads first the formation of MCR-Cp2. The $|\chi(R)|$ of MCR-Cp2, shows that the shape and position of the two peaks remain identic to that of pristine LiCoO₂. However, the peaks intensities along with the relative intensity decrease, allowing to anticipated that MCR-Cp2 is an isostructural of LiCoO₂ with small local change. The $|\chi(R)|$ of MCR-Cp3 is different from LiCoO₂ and MCR-Cp2, since three peaks feature in its $|\chi(R)|$ reveal the change of the structural motif. According to *in situ* XRD results, MCR-Cp3 was assigned to Co₃O₄. Therefore, the first peak of $|\chi(R)|$ corresponds Co-O distances. The second peak represents the Co_{octa}-Co distances, and the third peak appears due to the presence of Co on tetrahedral symmetry and it characterizes Co_{tetra}-Co distances. The intensities the peaks shrinking, agreeing with disorder of Co environments. The $|\chi(R)|$ of MCR-Cp4 has two broader peaks with low intensities, agrees with high atomic disorder at high temperature.

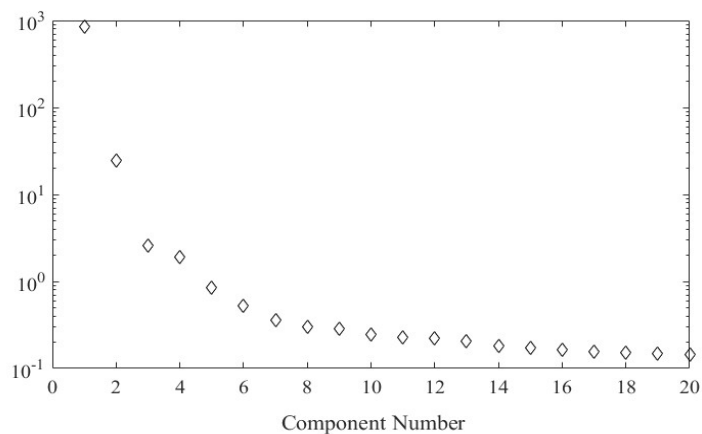


Figure III-8: Scree plot of $\text{LiCoO}_2: \text{K}_2\text{S}_2\text{O}_7$ [1:1.5] determined by PCA analysis.

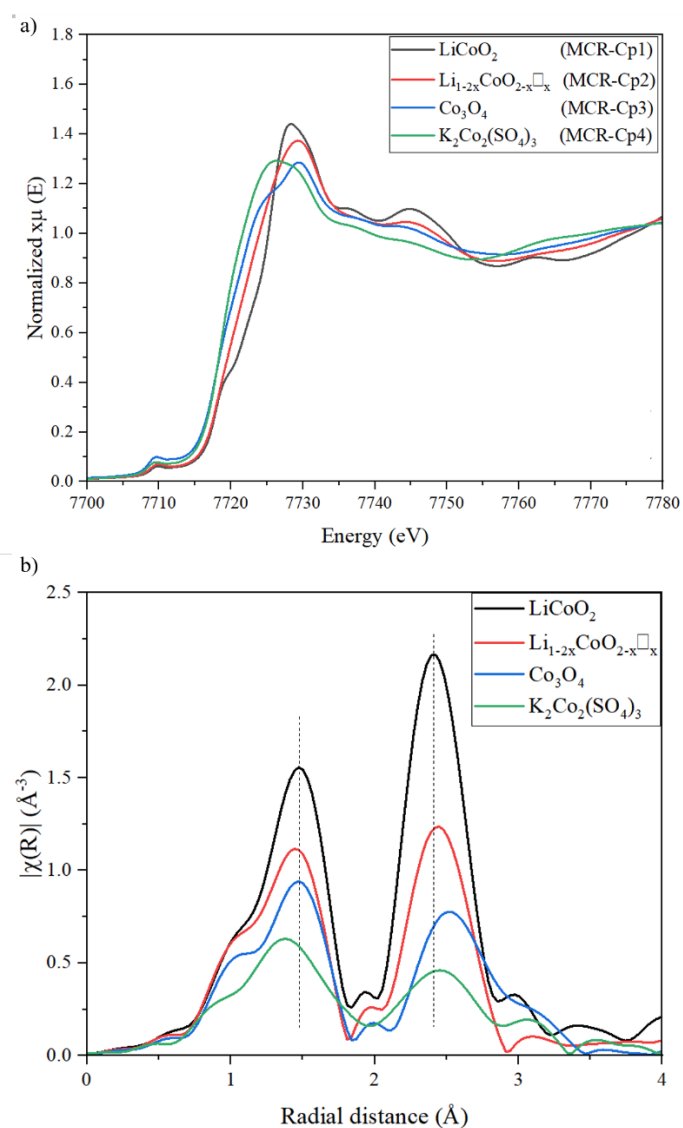


Figure III-9: a) Co K-edge XANES spectra of components calculated via MCR-ALS. b) Fourier transformation of k^3 weighted EXAFS oscillation for the four components.

To identify the MCR-Cp2 and MCR-Cp3, a refinement of EXAFS was performed based on the structural model detected from XRD analysis. Accordingly, the structural model for the MCR-Cp2 was $\text{Li}_{1-2x}\text{CoO}_{2-x}\square_x$. The refinement was first performed starting from the stoichiometric LiCoO_2 yielding a reliable factor of 0.0321 (**Figure III-10.a**). The introduction of anionic vacancies significantly improves the fit, with R-factor = 0.0102 (**Figure III-10.b**). In addition, to respect electroneutrality, the content of lithium was adjusted to the concentration of oxide vacancies. The fit only slightly improved yielding to R= 0.007 (**Figure III-10.c**), which is due to the lightweight of Li^+ ions. The deduced composition was $\text{Li}_{0.66}\text{CoO}_{1.83}\square_{0.17}$.

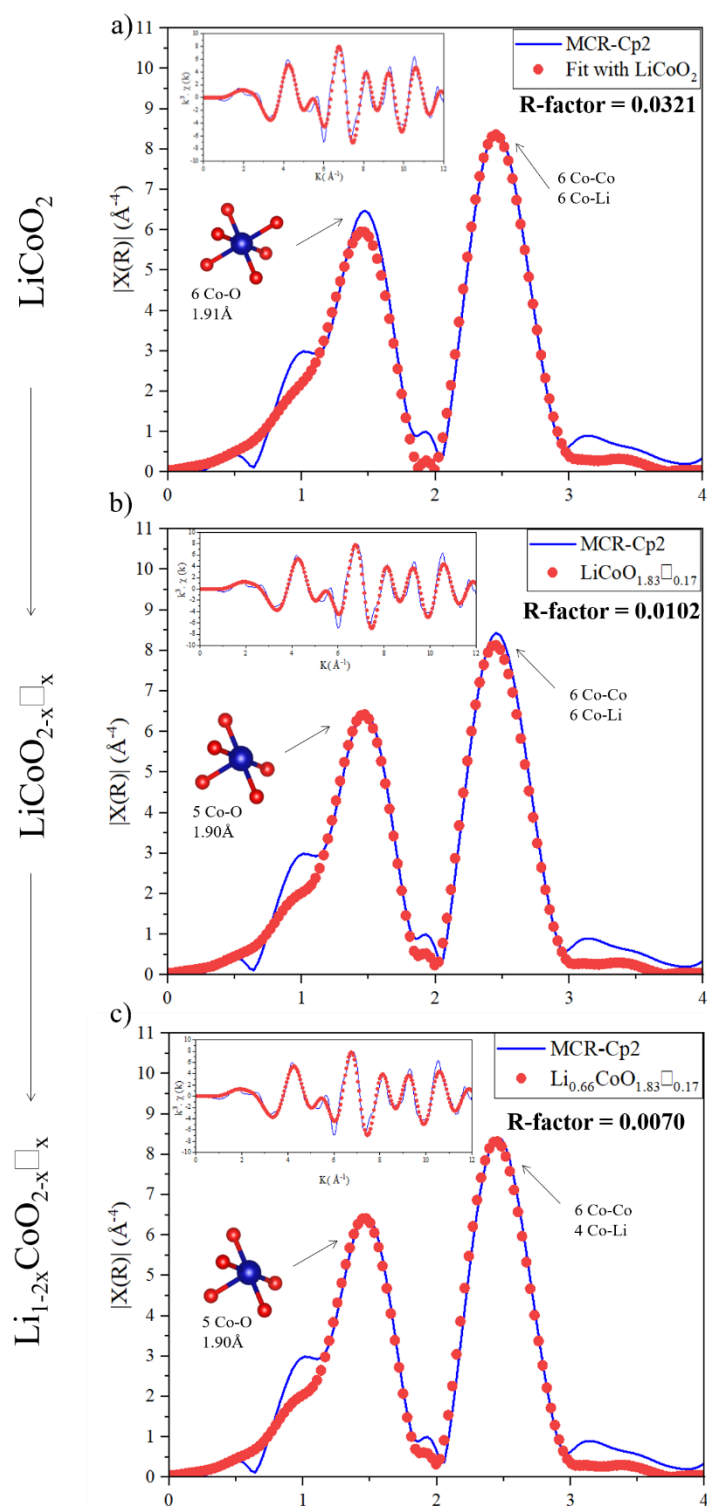


Figure III-10: Magnitude of Fourier transforms of k^3 weighted EXAFS oscillations for MCR-Cp2 along with their fitting results with (a) LiCoO_2 . b) $\text{LiCoO}_{2-x}\square_x$. c) $\text{Li}_{1-2x}\text{CoO}_{2-x}\square_x$. Insets show the quality of fits in the k -space.

Table III-2: Results of the refinement of the EXAFS oscillations for MCR-Cp2 with LiCoO_2 , $\text{LiCoO}_{2-x}\square_x$ and $\text{Li}_{1-2x}\text{CoO}_{2-x}\square_x$.

		N	σ^2	E_0	R ref	R
LiCoO ₂	Co- O	6	0.00847	-1.490	1.92	1.91
	Co- Co	6	0.00671	-1.490	2.82	2.82
	Co- Li	6	0.00154	-1.490	2.85	2.84
LiCoO _{2-x} □ _x	Co- O	5	0.00576	-1.490	1.92	1.90
	Co- Co	6	0.00671	-1.490	2.82	2.82
	Co- Li	6	0.00154	-1.490	2.85	2.84
Li _{1-2x} CoO _{2-x} □ _x	Co- O	5	0.00584	-1.490	1.92	1.90
	Co- Co	6	0.00671	-1.490	2.82	2.82
	Co- Li	4	0.00154	-1.490	2.85	2.84

To study the local structure of MCR-Cp3, the EXAFS oscillations was refined with Co_3O_4 . The Co_3O_4 has spinel structure with $2/3$ of Co^{III} in the octahedral site and $1/3$ of Co^{II} in the tetrahedral site. **Figure III-11** shows the $|\chi(R)|$ of MCR-Cp3 with it fit. The EXAFS fit was performed considering the concentration of Co^{III} and Co^{II} . Therefore, the S_0^2 of each Co has been calculated. **Table III-3** summarize the result of the refinement. The quality of fit is good (R-factor = 0.015) and the distances match with those of Co_3O_4 reference. The first peak represents six Co-O (1.90Å) and four Co-O (1.93Å) and the second peak corresponds to 6 Co-Co (2.85Å) and 12 Co-Co (3.30Å).

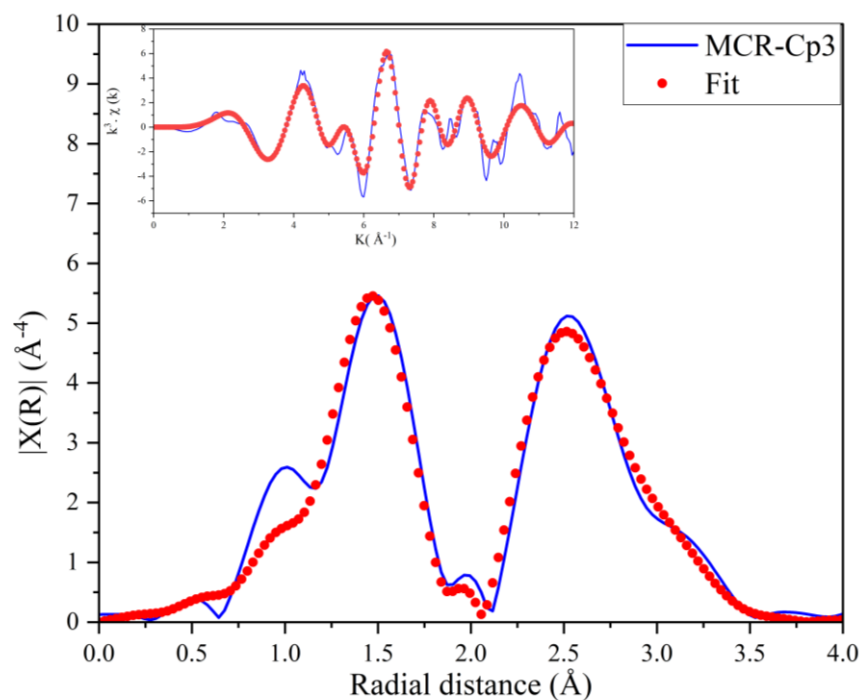


Figure III-11: Magnitude of Fourier transforms of k^3 weighted EXAFS oscillations for MCR-Cp3 along with its fitting results. Inset shows the quality of fits in the k -space.

Table III-3: Result of EXAFS refinement of the MCR-Cp3 with Co_3O_4 model.

		N	S02	σ^2	E_0	R ref	R
MCR-Cp3	$\text{Co}_1\text{-O}$	6	0.410	0.01088	-1.078	1.917	1.896
	$\text{Co}_2\text{-O}$	4	0.200	0.00120	-1.078	1.942	1.928
	$\text{Co}_1\text{-Co}$	6	0.410	0.00937	-1.078	2.858	2.854
	$\text{Co}_2\text{-Co}$	12	0.200	0.00984	-1.078	3.351	3.301

Moreover, the evolution of the relative concentration of the four components as function of the temperature is represented in **Figure III-12**. The sulfation process begins at temperatures well below the melting temperature of $\text{K}_2\text{S}_2\text{O}_7$, the LiCoO_2 was converted into $\text{Li}_{1-2x}\square_{2x}\text{CoO}_{2-x}\square_x$, through acid-base Lux-Flood concept. This latter achieves its maximum at 250°C . Further heating, the layered $\text{Li}_{1-2x}\square_{2x}\text{CoO}_{2-x}\square_x$ is progressively converted into spinel Co_3O_4 . The formation of Co_3O_4 results from the deep delithiation leading to the transformation from layered

structure to spinel. When temperature reaches 400°C, the complete layered-spinel transformation achieved. Finally, during the isotherm step Co_3O_4 is consumed yielding the formation of $\text{K}_2\text{Co}_2(\text{SO}_4)_3$. Comparing with the variable temperature XRD result, we conclude that, despite the evolution of the second component, the temperature of formation and presence of each component are in accordance.

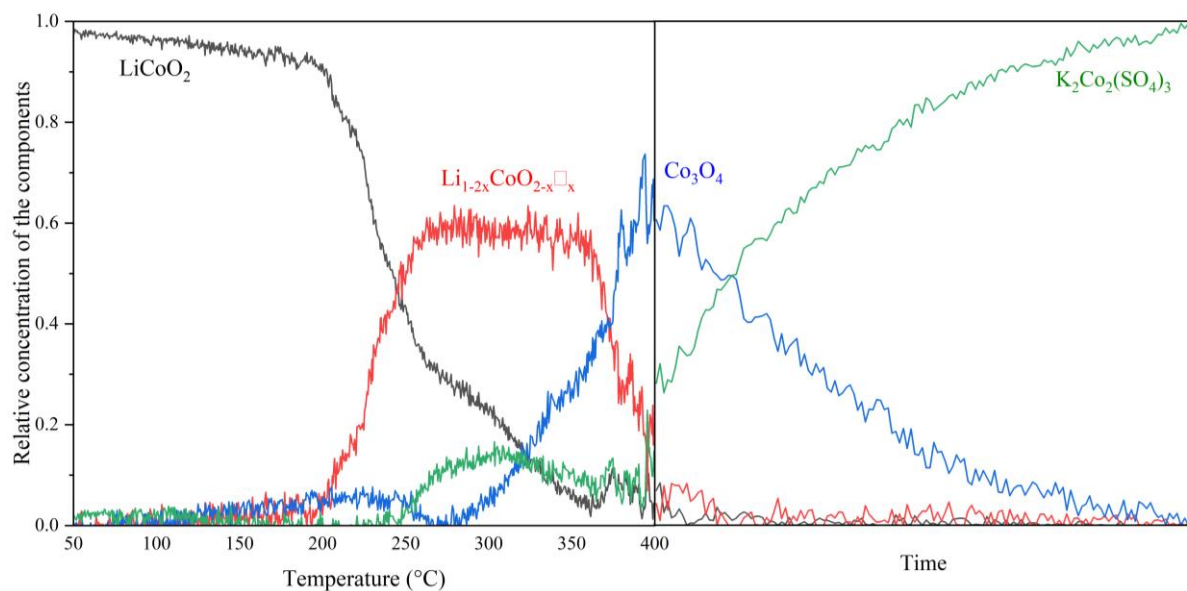
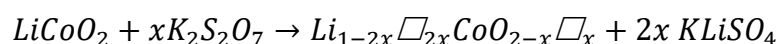


Figure III-12: Evolution of concentration profile of the four components involved upon the sulfation of LiCoO_2 .

III.4 Conclusion

The reactivity of LiCoO_2 with $\text{K}_2\text{S}_2\text{O}_7$ was shown to include several pathways discussed in the following. A first step occurring well below the melting point and therefore involving reaction at solid-solid interfaces takes place through the acid-base Lux-Flood concept. It involves $\text{K}_2\text{S}_2\text{O}_7$ as the oxoacid and LiCoO_2 as the oxobase and can be written as below:



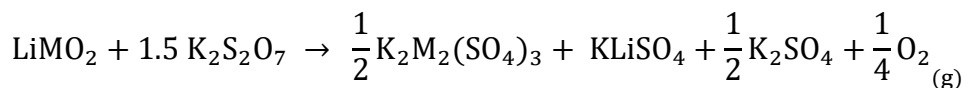
The reaction led to the formation of the double sulfate salt LiKSO_4 showing that $\text{K}_2\text{S}_2\text{O}_7$ is oxophile and selective to Li^+ ions. Variable temperature XRD showed that the defective phase is formed via a solid-solution behavior. An “average” composition $\text{Li}_{0.66}\square_{0.34}\text{CoO}_{1.83}\square_{0.17}$ was deduced from the refinement of the EXAFS of the PCA. The overall extraction of Li_2O from the layered structure leaving vacancies within both cationic and anionic sublattices further causes an instability which might be at the origin of the appearance of the spinel-like structure.

The layered to spinel-like phase transition has been widely investigated in layered positive electrode materials^{98,99}. Both structures are built from a cubic close-packed oxygen array so that the phase transition is due to cationic migration from the TM to Li ions slabs. Various factors have been shown to promote such a phase transition, namely the oxidation state, the lithium quantity and the temperature⁹⁹. Note that the layered $\text{Li}_{0.5}\text{CoO}_2$ was shown to be stable even after heating at 200 °C. The reactivity with $\text{K}_2\text{S}_2\text{O}_7$, however, implied both cationic and anionic vacancies driven by temperature, all these factors then facilitating the phase transition. As shown by variable temperature XRD analysis, both phases are intermediate appearing prior to the completion of the sulfation reaction and the growth of the langbeinite compound. It would be interesting to perform variable temperature XRD under equilibrium conditions, *i.e.*, slow heating ramp, mild temperature of around 200 °C along with a small content of $\text{K}_2\text{S}_2\text{O}_7$, particularly to stabilize $\text{Li}_{1-2x}\square_{2x}\text{CoO}_{2-x}\square_x$ with a controllable content of vacancies.

Finally, it was shown that the onset of the sulfation occurred at a temperature which is close to that of the melting point of $\text{K}_2\text{S}_2\text{O}_7$.

Chapter IV. General conclusion

In this work, we have explored a new method to recycle positive electrode materials of spent Li-ion batteries. This approach is based on the chemical conversion of lithiated transition metal oxide into water soluble sulfate products. We have shown that the sulfation of LiCoO₂ either with KHSO₄ or with K₂S₂O₇ result in water-soluble sulfate-based product: LiKSO₄, K₂SO₄, and the langbeinite sulfate salt K₂Co₂(SO₄)₃. Our study has been extended to NMC (LiNi_{1/3}Mn_{1/3}Co_{1/3}O₂) and NCA (LiNi_{0.82}Co_{0.15}Al_{0.03}O₂) materials. The overall reactions can be written as:

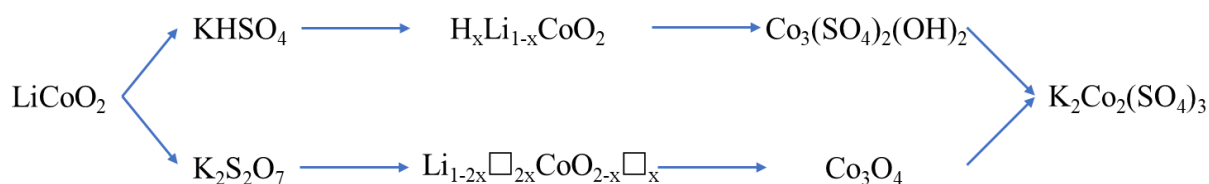


The conversion of LMO using KHSO₄ molten salt involves a complex reaction mechanism. An ionic exchange H⁺/Li⁺ between layered structure and molten salt occurs and it was carefully investigated by variable-temperature XRD, X-ray absorption spectroscopy (XAS) and DFT calculation. This H⁺/Li⁺ exchange allowing the formation of solid-solution H_xLi_{1-x}MO₂ with higher *c* parameter due to the repulsive force between facing oxide ions, caused by the removal of Li. The H⁺/Li⁺ substitution leads formation of hydroxyl ligand OH inducing a distortion of MO₆ octahedra around O-H, yielding elongation of M-O distance as shown by XAS (2.35Å for H_xLi_{1-x}CoO₂). According to DFT calculation in the case of LiCoO₂, at high H⁺/Li⁺ substitution rate, the H₂O molecule within H_xLi_{1-x}CoO₂ framework are spontaneously formed. Thereafter, the dehydration leads the migration of Co²⁺ into layer wherein H₂O molecule have been released. These Co^{II} sites are reactive to sulfation, allowing the formation of Co₃(SO₄)₂(OH)₂. Further heating, the cobalt hydroxy sulfate phase is converted to langbeinite K₂Co₂(SO₄)₃. In summary, this study reveals that the conversion mechanism with KHSO₄ is based on the presence of protons.

Moreover, to investigate the reaction of LMO with free proton molten salt, the reaction between LiCoO₂ and pyrosulfate (K₂S₂O₇) molten salt was studied. The variable-temperature XRD reveals the formation of KLiSO₄ and Li_{1-2x}□_{2x}CoO_{2-x}□_x according to Lux-Flood theory,

between $S_2O_7^{2-}$ oxoacid and $LiCoO_2$ oxobase. Upon further heating, the cation and anion vacancies induce through extraction of LiO_2 leads to the destabilization of the layered $Li_{1-2x}□_{2x}CoO_{2-x}□_x$ structure, yielding its transformation to spinel Co_3O_4 . Finally, the sulfation begins at temperature close to the melting point of $K_2S_2O_7$ allowing the formation of $K_2Co_2(SO_4)_3$.

To summarize both $KHSO_4$ and $K_2S_2O_7$ have the ability to convert lithiated transition metal oxide into water-soluble sulfate-based products: $K_2Co_2(SO_4)_3$, $KLiSO_4$, and K_2SO_4 . The reaction mechanism with $KHSO_4$ relies on the presence of proton, while, with $K_2S_2O_7$ reaction occurs following acid-base Lux-Flood reaction. The evolution of Co element upon reaction of $LiCoO_2$ with molten salt can be summarized as follow:



The sulfate-based products are soluble in water, thus during our research, a water leaching study was also realized on the recovered product after sulfation of $LiCoO_2$ by $KHSO_4$ (this study has not been discussed in this manuscript). First, we have estimated the solubility of sulfate product from the literature results on double salt dissolution^{100,101}. The result demonstrated that the solubility of sulfate product is limited by Co solubility ($0.160 \text{ mol. Kg}^{-1}$). In second part, the water leaching was carried out to recover Co and Li: 98.87% of Co is recovered using potassium oxalate ($K_2C_2O_4$) and 78% of the lithium was recovered as Li_3PO_4 . (details of the recovering processes are presented in appendix).

Overall, we have developed an alternative process for the recycling of positive electrode material of spent Li-ion batteries. The processes include a solid-state reaction between positive electrode material and molten salt, followed by water leaching. This work provides a more detailed understanding of mechanism that occurs during sulfation process, however, the water leaching process can be investigated in more details to experimentally determine the solubility of sulfate-based product resulting from reaction between LMO ($M= Co, Ni, Mn$) and molten

salt, improve the recovery of Li from LiCoO_2 , and extend the water leaching to other positive electrode material such as LiMn_2O_4 and $\text{Li}_2\text{Mn}_3\text{NiO}_4$.

Appendix

A. Chapter II.

A. 1. Detail of PCA result

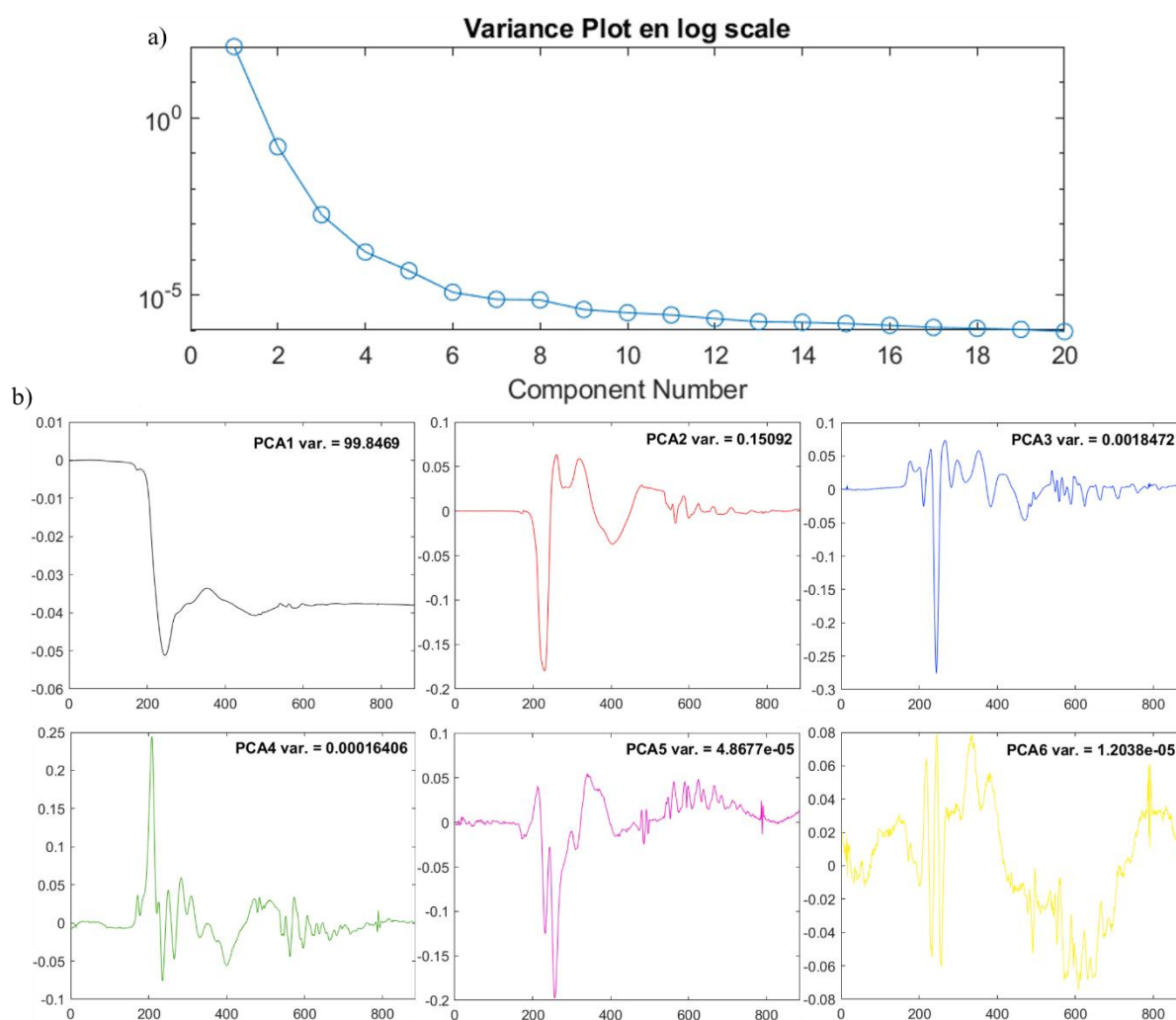
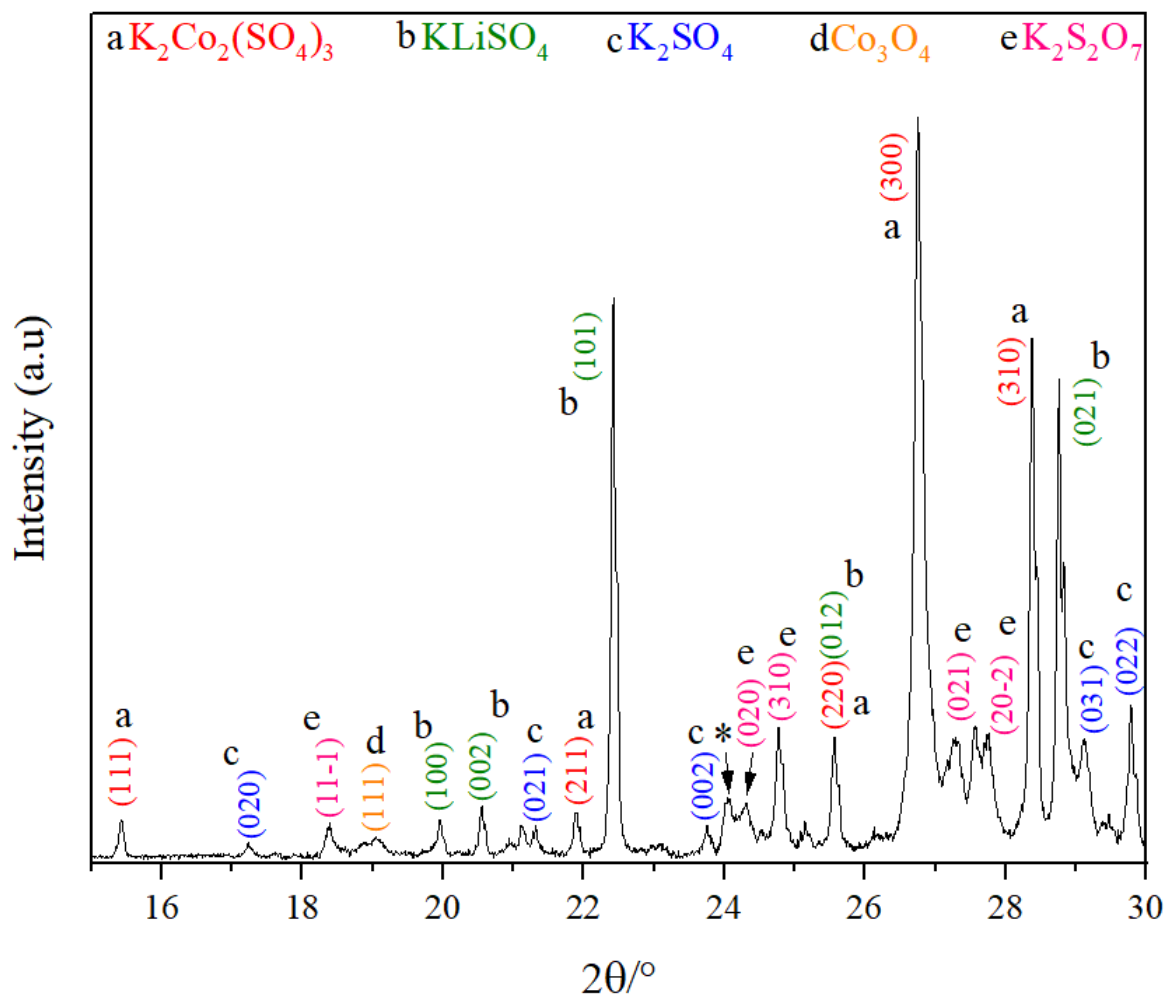


Fig.A. 1: Detailed PCA results for sulfation of LiCoO_2 using KHSO_4 . **a)** the variance plot. **b)** The evolution of scores for the six first components.

A. 2. XRD of sulfate product recovered after XAS analysis.

**Fig.A. 2:** XRD of product recovered after XAS analysis of $\text{LiCoO}_2:\text{KHSO}_4$ [1: 1.5]

A. Chapter III.

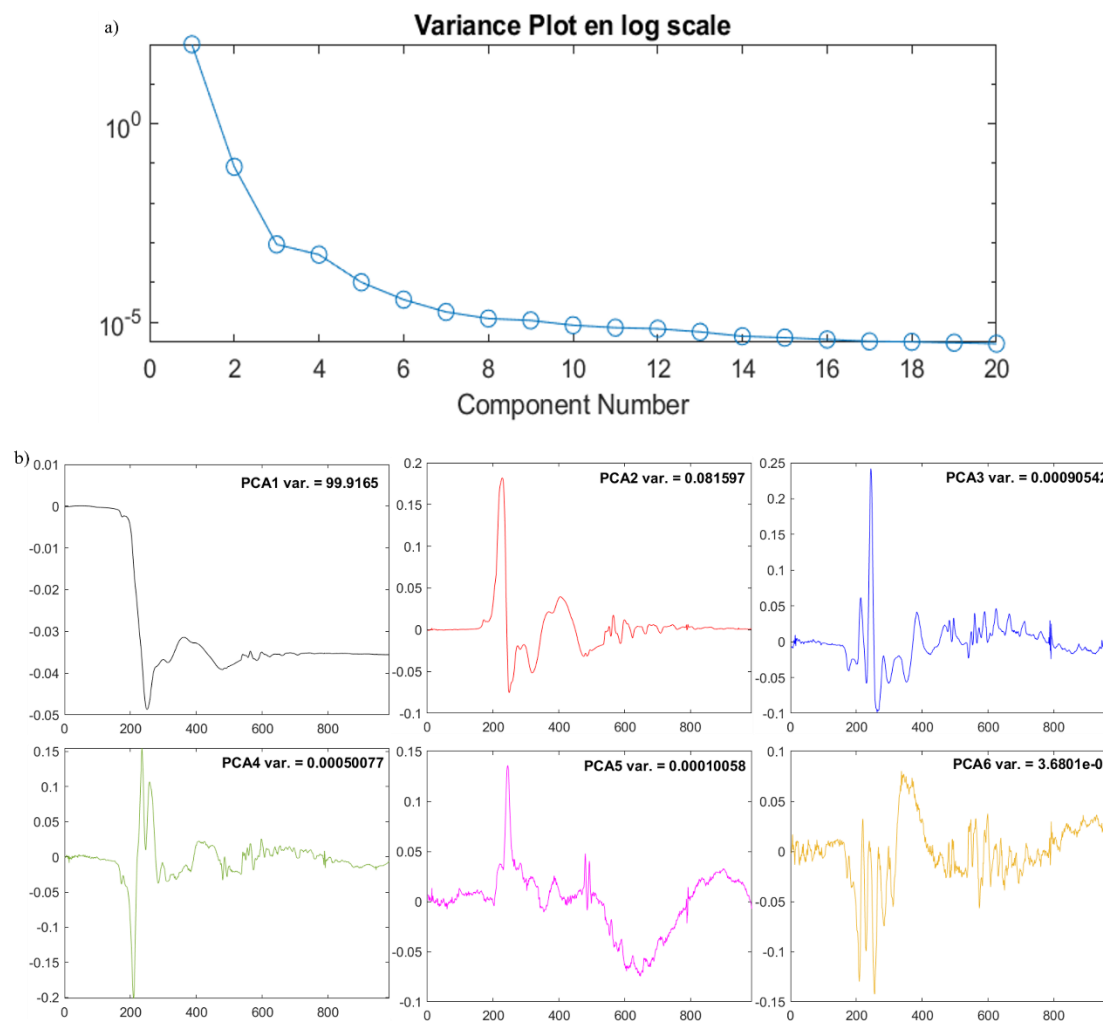
A. 3. Detail of PCA result of LiCoO_2 : $\text{K}_2\text{S}_2\text{O}_7$.

Fig.A. 3: Detailed PCA results for sulfation of LiCoO_2 using $\text{K}_2\text{S}_2\text{O}_7$. **a)** the variance plot. **b)** the evolution of scores for the six first components.

A. 4. Theoretical prediction of the solubility in water at 25 °C:

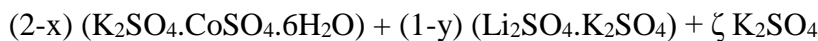
The formation of double salt in the quaternary system $\text{CoSO}_4\text{-Li}_2\text{SO}_4\text{-K}_2\text{SO}_4\text{-H}_2\text{O}$ lead to the arduous experimental determination of solubility. A regular control of several parameters such as stirring duration, temperature, pressures, solution density must be carried out. That was not easy to undertake in our laboratory. Thus, to determine the solubility of sulfate-based product, a theoretical calculation using the experimental data from the literature was applied.

1. Preliminary considerations:

Supposing that the addition of $6(2-x) + 55.5$ moles of water to the sulfate-based products solution lead to the saturated solution of CoSO_4 , Li_2SO_4 and K_2SO_4 . In the solid phase, the Tutton's double salt $\text{K}_2\text{Co}(\text{SO}_4)_2 \cdot 6\text{H}_2\text{O}$ written as $\text{K}_2\text{SO}_4 \cdot \text{CoSO}_4 \cdot 6\text{H}_2\text{O}$, the double salt KLiSO_4 written as $\text{Li}_2\text{SO}_4 \cdot \text{K}_2\text{SO}_4$ and K_2SO_4 were established. We can see that $6(2-x)$ moles of water initially added, were part of Tutton's salt and 55.5 remain in solution. To simplify the notation afterwards, the dissolved CoSO_4 , Li_2SO_4 and K_2SO_4 are note x , y and z respectively. With:

$$\begin{aligned} x &= \frac{[\text{CoSO}_4]}{m_0} \\ y &= \frac{[\text{Li}_2\text{SO}_4]}{m_0} \\ z &= \frac{[\text{K}_2\text{SO}_4]}{m_0} \end{aligned} \quad m_0 = 1 \text{ mol. Kg}^{-1}$$

Considering the stoichiometry of the double salts, the molar composition of the solid was:



The K_2SO_4 moles, ζ , was calculated according to: $2-x+1-y+z+\zeta=3$, where $\zeta=x+y-z>0$ so, $y>z$. This result was experimentally verified for various systems at 25 °C and it was observed that the solubility of K_2SO_4 still remains 0.8 mol Kg^{-1} , for examples:

Systems	Solid phase	y	z
$\text{Li}_2\text{SO}_4 - \text{K}_2\text{SO}_4 - \text{H}_2\text{O}^{102}$	$\text{Li}_2\text{SO}_4 \cdot \text{K}_2\text{SO}_4$ and K_2SO_4	1.23	0.78
$\text{Cs}_2\text{SO}_4 - \text{Li}_2\text{SO}_4 - \text{K}_2\text{SO}_4 - \text{H}_2\text{O}^{103}$ $m_{\text{Cs}_2\text{SO}_4}/m_0=0.039$	$9\text{Li}_2\text{SO}_4 \cdot 3\text{K}_2\text{SO}_4 \cdot 2\text{Cs}_2\text{SO}_4$, $\text{Li}_2\text{SO}_4 \cdot \text{K}_2\text{SO}_4$ and K_2SO_4	1.21	0.78
$\text{MgSO}_4 - \text{Li}_2\text{SO}_4 - \text{K}_2\text{SO}_4 - \text{H}_2\text{O}^{103}$ $m_{\text{MgSO}_4}/m_0=1.12$	$\text{K}_2\text{SO}_4 \cdot \text{MgSO}_4 \cdot 6\text{H}_2\text{O}$, $\text{Li}_2\text{SO}_4 \cdot \text{K}_2\text{SO}_4$ and K_2SO_4	0.97	0.83

To predict the solubility of the obtained sulphate-based product, the $\text{Li}_2\text{SO}_4 - \text{K}_2\text{SO}_4 - \text{H}_2\text{O}$ ¹⁰³ and $\text{K}_2\text{SO}_4 - \text{CoSO}_4 - \text{H}_2\text{O}$ ¹⁰¹ solubility diagrams at 25 °C represented in Fig.A.4 a and Fig.A.4 .b, respectively were used. Each diagram has two eutonic points where two solid phases coexist. It was showed that the dissolution of the double salts $\text{Li}_2\text{SO}_4 \cdot \text{K}_2\text{SO}_4$ (Fig.A. 4a) and $\text{K}_2\text{SO}_4 \cdot \text{CoSO}_4 \cdot 6\text{H}_2\text{O}$ (Fig.A. 4.b) is incongruent, *i.e.* the composition of the solid and the dissolved solutes was not stoichiometrically. The diagrams in Fig.A.4 were used to calculate the solubility of the heterogeneous sulphate-based product mixture.

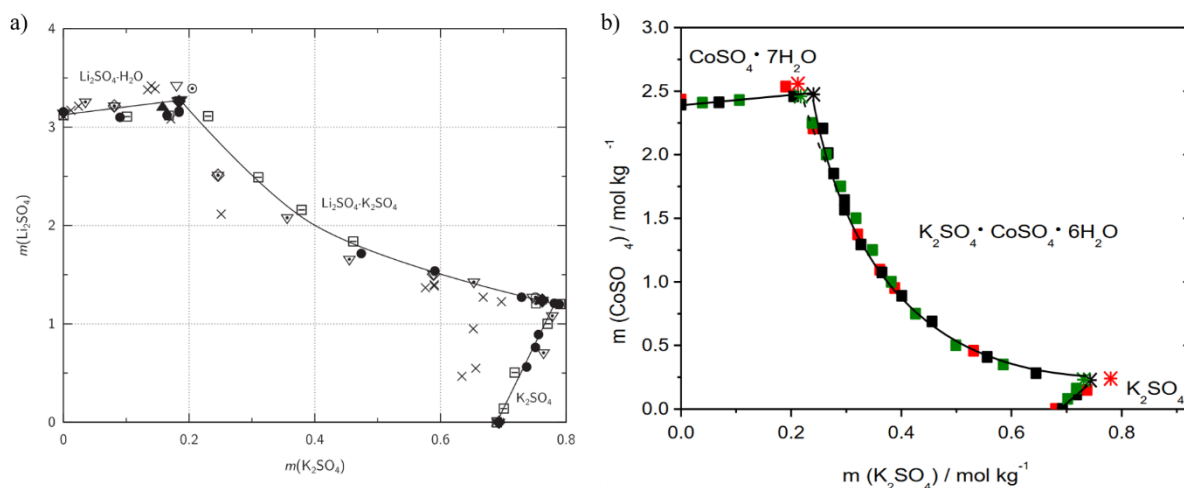


Fig.A. 4: Experimental data of the solubility at 25 °C of a) $\text{Li}_2\text{SO}_4 - \text{K}_2\text{SO}_4 - \text{H}_2\text{O}$ and b) $\text{K}_2\text{SO}_4 - \text{CoSO}_4 - \text{H}_2\text{O}$ systems.

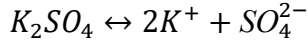
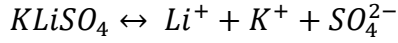
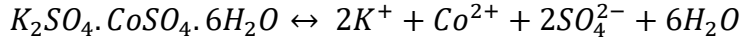
2. Study of ternary system $\text{Li}_2\text{SO}_4 - \text{K}_2\text{SO}_4 - \text{H}_2\text{O}$ and $\text{K}_2\text{SO}_4 - \text{CoSO}_4 - \text{H}_2\text{O}$

- Assumptions

- At equilibrium, the dissociation equation did not consider the formation of the KSO_4^- ion pair.
- The activity coefficients of common ions in the quaternary saturated solution $\text{Li}_2\text{SO}_4 - \text{K}_2\text{SO}_4 - \text{CoSO}_4 - \text{H}_2\text{O}$ and in the ternary saturated solutions $\text{Li}_2\text{SO}_4 - \text{K}_2\text{SO}_4 - \text{H}_2\text{O}$, $\text{K}_2\text{SO}_4 - \text{CoSO}_4 - \text{H}_2\text{O}$ of identical ionic strength are little different from each other.
- The activity of water transferred from solid $\text{K}_2\text{SO}_4 \cdot \text{CoSO}_4 \cdot 6\text{H}_2\text{O}$ to solutions was similar to that of the solvent¹⁰⁴.

- Variation of dissociation constants as a function of the ionic strength of the solution

at equilibrium:



K_x , K_y et K_z were the dissociation constant of Co^{2+} , Li^+ and K^+ respectively, at the equilibrium. These constants, as well as the ionic strength of the solution, I , are calculated from the solubility curves at 25 °C of the ternary systems presented in Fig.A.5 .a and Fig.A.5. b by the relationships:

$$K = \prod_{i=1}^N \alpha_{i(f)}^{v_i} \quad I = \frac{1}{2} \sum \alpha_i \times z_i^2$$

Where: $\alpha_{i(f)}$ the chemical activity of i at equilibrium ($\alpha_{i(f)} = x, y$ or z), v_i the stoichiometric coefficient and π the product operator, z charge number of ions.

$$\begin{array}{llll} K_x = 4xz^2(x+z)^2 & I = 4x+3z & \text{(Fig.A. 4.b)} & x = \frac{[CoSO_4]}{m_0} \\ K_y = 4yz(y+z) & I = 3(y+z) & \text{(Fig.A. 4.a)} & y = \frac{[Li_2SO_4]}{m_0} \\ K_z = 4z^2(y+z) & I = 3(y+z) & \text{(Fig.A. 4.a)} & z = \frac{[K_2SO_4]}{m_0} \end{array} \quad m_0 = 1 \text{ mol.Kg}^{-1}$$

In Fig.A. 5.a and Fig.A. 5.b, K_x , K_y et K_z are plotted as a function of the ionic strength I . The fitted curve of K_x was obtained by polynomial regression of degree 3 while those of K_y and de K_z were obtained by linear regression. The points (K_z , I) calculated from Fig.A. 4.a and from Fig.A. 4.b (dots in red), were consistent with our assumptions. The curve fit equations are:

$$K_x = -0.0070I^3 + 0.129I^2 - 0.344I + 0.48 \quad \text{(eq. 1)}$$

$$K_y = 0.333I + 5.428 \quad \text{(eq. 2)}$$

$$K_z = 0.920I - 0.708 \quad \text{(eq. 3)}$$

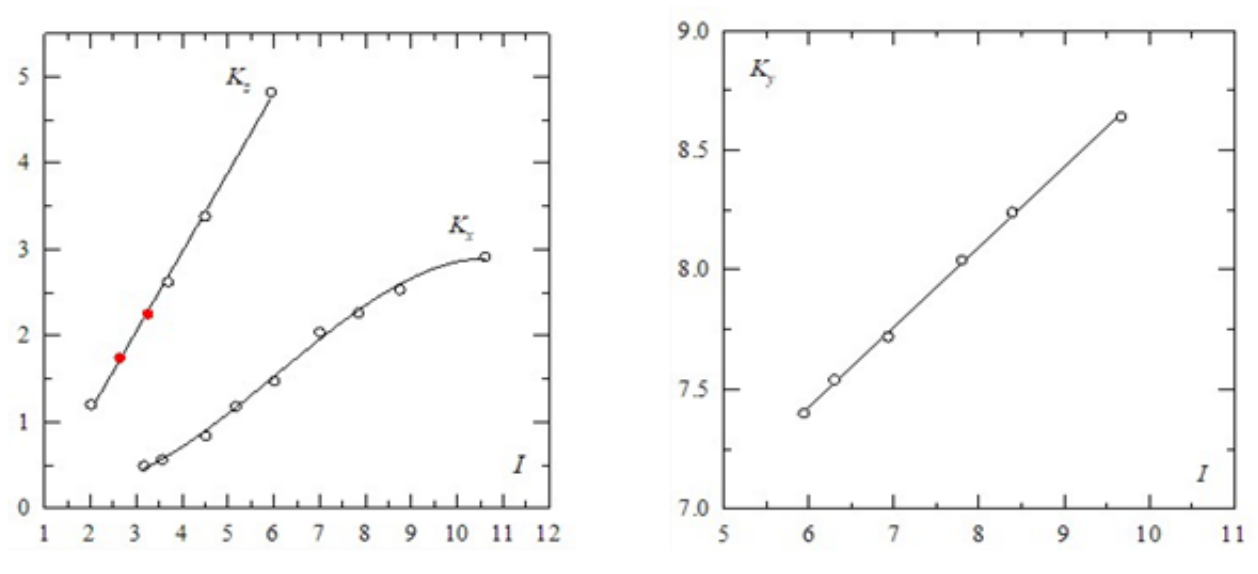


Fig.A. 5:Dissociation constants (a) K_x and K_z and (b) K_y as function of ionic strength I

3. The study of quaternary $\text{Li}_2\text{SO}_4 - \text{K}_2\text{SO}_4 - \text{CoSO}_4 - \text{H}_2\text{O}$ at 25°C :

The prepared solution, contains Li_2SO_4 , K_2SO_4 , CoSO_4 and H_2O . At equilibrium, by analogy to the previous result, we conclude that dissociation constants in quaternary system could be written as:

$$K_x = 4xz^2(x + y + z)^2$$

$$K_y = 4yz(x + y + z)$$

$$K_z = 4z^2(x + y + z)$$

and

$$I = 4x + 3(y + z) \quad (\text{eq. 4})$$

Leads to:

$$x = \frac{4K_x}{K_y^2} y^2 \quad (\text{eq. 5})$$

$$z = \frac{K_z}{K_y} y \quad (\text{eq. 6})$$

$$\frac{16K_x K_z}{K_y^3} y^4 + \frac{4K_z}{K_y} \left(1 + \frac{K_z}{K_y}\right) y^3 - K_y = 0 \quad (\text{eq. 7})$$

- Numeric application: test

The calculation was initiated with $z= 0.8$. from Fig.A. 4a, it observed that $y= 1.2$, and from Fig.A. 4.b it found that, $x=0.25$. Thus, $I= 7$ was calculated using **eq.4**. Then K_x , K_y and K_z were calculated by **eq.1** to **eq.3** and y , x , and z using **e.q 5** to **eq. 7**. Table 4 shows the obtained result following the loop Fig.A. 6. The calculation was done until the self-consistency, *i.e.* when a gap between two successful I was less than 0.01.

$$I = 4 \times 0.25 + 3 \times (1.2 + 0.8) = 7$$

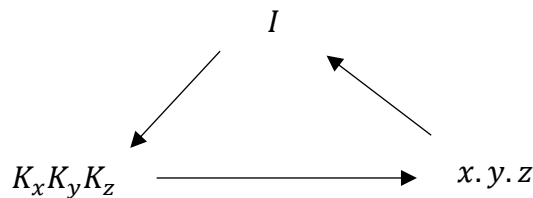


Fig.A. 6:loop of calculation of (K_x , K_y , K_z), (x , y , z) and I

Table 4: Value of calculated (K_x , K_y , K_z), (x , y , z) and I

I_{int}	K_x	K_y	K_z	y^4	y^3	y	x	z	I_{final}
7,000	1,996	7,759	5,732	0,392	5,138	1,116	0,165	0,824	6,482
6,482	1,768	7,587	5,255	0,340	4,691	1,143	0,161	0,792	6,446
6,446	1,752	7,575	5,223	0,337	4,660	1,145	0,160	0,789	6,444

the condition was satisfied for $I = 6.45$ and the following solubility values at 25°C were determined. Thus, we can conclude that the solubility of the recovered sulfate-based product is limited by solubility of cobalt.

$$m_{\text{CoSO}_4} = 0,160 \text{ mol. Kg}^{-1}, m_{\text{Li}_2\text{SO}_4} = 1,145 \text{ mol. Kg}^{-1} \text{ and } m_{\text{K}_2\text{SO}_4} = 0,790 \text{ mol. Kg}^{-1}$$

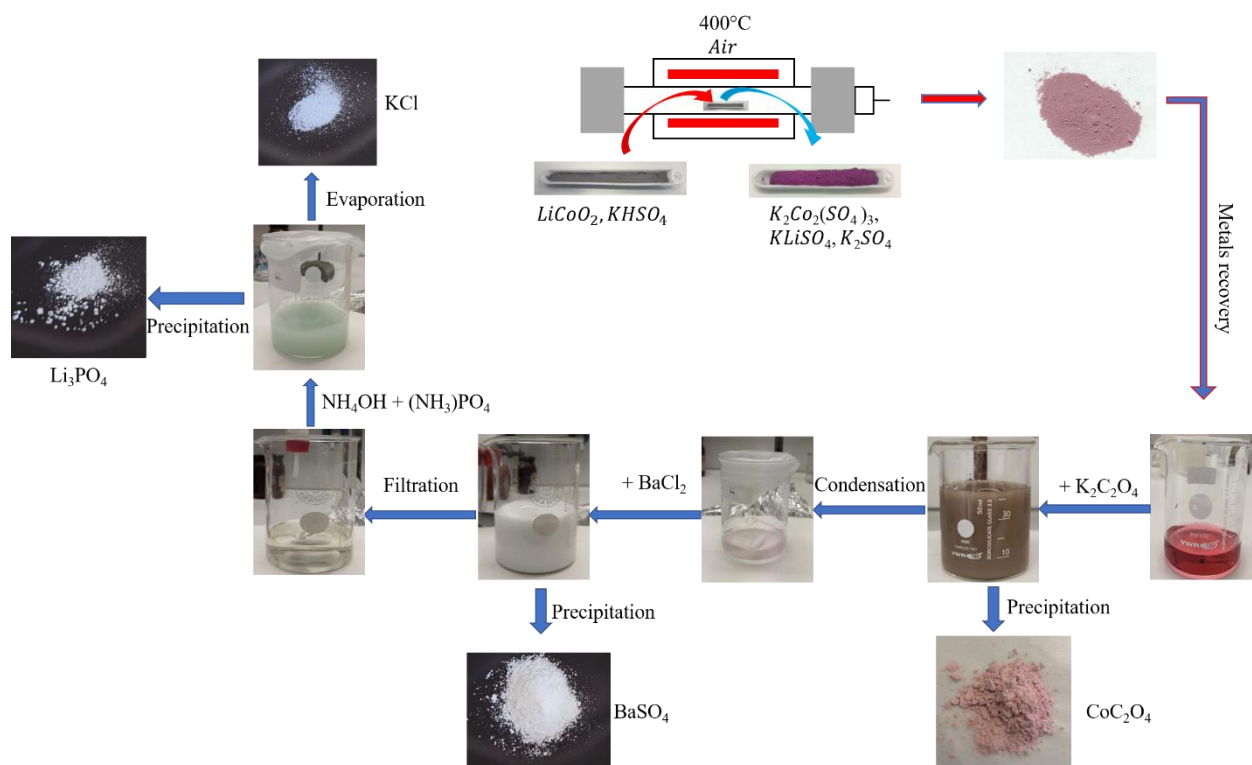
A. 5. Recovery of Co and Li from LiCoO_2 after sulfation with KHSO_4 molten salt.

Fig.A. 7: Illustration of the sulfation of LiCoO_2 using KHSO_4 molten salt, and the recovery of Co and Li element.

References

- (1) *Soutien à l'objectif de zéro émission pour les voitures et camionnettes en 2035 / Actualité / Parlement européen.* <https://www.europarl.europa.eu/news/fr/press-room/20220603IPR32129/soutien-a-l-objectif-de-zero-emission-pour-les-voitures-et-camionnettes-en-2035> (accessed 2022-10-15).
- (2) Swain, B. Cost Effective Recovery of Lithium from Lithium Ion Battery by Reverse Osmosis and Precipitation: A Perspective. *J. Chem. Technol. Biotechnol.* **2018**, *93* (2), 311–319. <https://doi.org/10.1002/jctb.5332>.
- (3) Raj, T.; Chandrasekhar, K.; Kumar, A. N.; Sharma, P.; Pandey, A.; Jang, M.; Jeon, B.-H.; Varjani, S.; Kim, S.-H. Recycling of Cathode Material from Spent Lithium-Ion Batteries: Challenges and Future Perspectives. *J. Hazard. Mater.* **2022**, *429*, 128312. <https://doi.org/10.1016/j.jhazmat.2022.128312>.
- (4) Lentz, G. Y.; Knorr, K.; Depmeier, W.; Baetz, C.; Knapp, M.; Morgenroth, W. Phase Transitions in Mercallite, KHSO₄. 2.
- (5) De Vries, K. J.; Gellings, P. J. The Thermal Decomposition of Potassium and Sodium-Pyrosulfate. *J. Inorg. Nucl. Chem.* **1969**, *31* (5), 1307–1313. [https://doi.org/10.1016/0022-1902\(69\)80241-1](https://doi.org/10.1016/0022-1902(69)80241-1).
- (6) Lux, H. “Säuren” Und “Basen” Im Schmelzfluss: Die Bestimmung Der Sauerstoffionen-Konzentration. *Z. Für Elektrochem. Angew. Phys. Chem.* **1939**, *45* (4), 303–309. <https://doi.org/10.1002/bbpc.19390450405>.
- (7) Flood, H.; FÖRLAND, T. The Acidic and Basic Properties of Oxides. *Acta Chem Scand* **1947**, *1* (6), 592--606.
- (8) Xu, K. Nonaqueous Liquid Electrolytes for Lithium-Based Rechargeable Batteries. *Chem. Rev.* **2004**, *104* (10), 4303–4418. <https://doi.org/10.1021/cr030203g>.
- (9) *The Nobel Prize in Chemistry 2019.* NobelPrize.org. <https://www.nobelprize.org/prizes/chemistry/2019/press-release/> (accessed 2022-10-03).
- (10) Whittingham, M. S. PREPARATION OF STOICHIOMETRIC TITANUM DSULFIDE. *U. S. Pat.* **1977**, *4,007,055*.
- (11) Mizushima, K.; Jones, P. C.; Wiseman, P. J.; Goodenough, J. B. Li_xCoO₂ (0. *Mater. Res. Bull.* **1980**, *15* (6), 783–789. [https://doi.org/10.1016/0025-5408\(80\)90012-4](https://doi.org/10.1016/0025-5408(80)90012-4).
- (12) Yoshino, A.; Sanechika, K.; Nakajima, T. Secondary Battery. US4668595A, May 26, 1987.
- (13) Jiang, Y.; Qin, C.; Yan, P.; Sui, M. Origins of Capacity and Voltage Fading of LiCoO₂ upon High Voltage Cycling. *J. Mater. Chem. A* **2019**, *7* (36), 20824–20831. <https://doi.org/10.1039/C9TA06579B>.

- (14) Noh, H.-J.; Youn, S.; Yoon, C. S.; Sun, Y.-K. Comparison of the Structural and Electrochemical Properties of Layered Li[NixCoyMnz]O₂ (x = 1/3, 0.5, 0.6, 0.7, 0.8 and 0.85) Cathode Material for Lithium-Ion Batteries. *J. Power Sources* **2013**, *233*, 121–130. <https://doi.org/10.1016/j.jpowsour.2013.01.063>.
- (15) Ceder, G.; Chiang, Y.-M.; Sadoway, D. R.; Aydinol, M. K.; Jang, Y.-I.; Huang, B. Identification of Cathode Materials for Lithium Batteries Guided by First-Principles Calculations. *Nature* **1998**, *392* (6677), 694–696. <https://doi.org/10.1038/33647>.
- (16) Thackeray, M. M.; David, W. I. F.; Bruce, P. G.; Goodenough, J. B. Lithium Insertion into Manganese Spinels. *Mater. Res. Bull.* **1983**, *18* (4), 461–472. [https://doi.org/10.1016/0025-5408\(83\)90138-1](https://doi.org/10.1016/0025-5408(83)90138-1).
- (17) Padhi, A. K. Phospho-Olivines as Positive-Electrode Materials for Rechargeable Lithium Batteries. *J. Electrochem. Soc.* **1997**. <https://doi.org/10.1149/1.1837571>.
- (18) Chung, S.-Y.; Bloking, J. T.; Chiang, Y.-M. Electronically Conductive Phospho-Olivines as Lithium Storage Electrodes. *Nat. Mater.* **2002**, *1* (2), 123–128. <https://doi.org/10.1038/nmat732>.
- (19) Ding, Y.; Cano, Z. P.; Yu, A.; Lu, J.; Chen, Z. Automotive Li-Ion Batteries: Current Status and Future Perspectives. *Electrochem. Energy Rev.* **2019**, *2* (1), 1–28. <https://doi.org/10.1007/s41918-018-0022-z>.
- (20) Annual Update on the Global Transition to Electric Vehicles: 2021. *International Council on Clean Transportation*.
- (21) Pillot, C. The Rechargeable Battery Market and Main Trends 2011-2020. **2018**, 25.
- (22) linda. Recyclage des batteries au lithium : que faut-il savoir. *Flash Battery*, 2020.
- (23) *De nouvelles règles européennes pour des batteries plus durables et éthiques | Actualité / Parlement européen.* <https://www.europarl.europa.eu/news/fr/headlines/economy/20220228STO24218/de-nouvelles-regles-europeennes-pour-des-batteries-plus-durables-et-ethiques> (accessed 2022-09-21).
- (24) Gaines, L.; Cuenca, R. Life-Cycle Costs of Lithium-Ion Vehicle Batteries. *SAE Trans.* **2000**, *109*, 1920–1931.
- (25) Zhou, M.; Li, B.; Li, J.; Xu, Z. Pyrometallurgical Technology in the Recycling of a Spent Lithium Ion Battery: Evolution and the Challenge. *ACS EST Eng.* **2021**, *1* (10), 1369–1382. <https://doi.org/10.1021/acsestengg.1c00067>.
- (26) Makuza, B.; Tian, Q.; Guo, X.; Chattopadhyay, K.; Yu, D. Pyrometallurgical Options for Recycling Spent Lithium-Ion Batteries: A Comprehensive Review. *J. Power Sources* **2021**, *491*, 229622. <https://doi.org/10.1016/j.jpowsour.2021.229622>.
- (27) Brückner, L.; Frank, J.; Elwert, T. Industrial Recycling of Lithium-Ion Batteries—A Critical Review of Metallurgical Process Routes. *Metals* **2020**, *10* (8), 1107. <https://doi.org/10.3390/met10081107>.

- (28) Kang, J.; Senanayake, G.; Sohn, J.; Shin, S. M. Recovery of Cobalt Sulfate from Spent Lithium Ion Batteries by Reductive Leaching and Solvent Extraction with Cyanex 272. *Hydrometallurgy* **2010**, *100* (3), 168–171. <https://doi.org/10.1016/j.hydromet.2009.10.010>.
- (29) Larouche, F.; Tedjar, F.; Amouzegar, K.; Houlachi, G.; Bouchard, P.; Demopoulos, G. P.; Zaghbi, K. Progress and Status of Hydrometallurgical and Direct Recycling of Li-Ion Batteries and Beyond. *Materials* **2020**, *13* (3), 801. <https://doi.org/10.3390/ma13030801>.
- (30) Yao, Y.; Zhu, M.; Zhao, Z.; Tong, B.; Fan, Y.; Hua, Z. Hydrometallurgical Processes for Recycling Spent Lithium-Ion Batteries: A Critical Review. *ACS Sustain. Chem. Eng.* **2018**, *6* (11), 13611–13627. <https://doi.org/10.1021/acssuschemeng.8b03545>.
- (31) Sun, L.; Qiu, K. Vacuum Pyrolysis and Hydrometallurgical Process for the Recovery of Valuable Metals from Spent Lithium-Ion Batteries. *J. Hazard. Mater.* **2011**, *194*, 378–384. <https://doi.org/10.1016/j.jhazmat.2011.07.114>.
- (32) Meshram, P.; Abhilash; Pandey, B. D.; Mankhand, T. R.; Deveci, H. Comparison of Different Reductants in Leaching of Spent Lithium Ion Batteries. *JOM* **2016**, *68* (10), 2613–2623. <https://doi.org/10.1007/s11837-016-2032-9>.
- (33) Kang, J.; Sohn, J.; Chang, H.; Senanayake, G.; Shin, S. M. Preparation of Cobalt Oxide from Concentrated Cathode Material of Spent Lithium Ion Batteries by Hydrometallurgical Method. *Adv. Powder Technol.* **2010**, *21* (2), 175–179. <https://doi.org/10.1016/j.apt.2009.10.015>.
- (34) Recovery of Co and Li from Spent Lithium-Ion Batteries by Combination Method of Acid Leaching and Chemical Precipitation. *Trans. Nonferrous Met. Soc. China* **2012**, *22* (9), 2274–2281. [https://doi.org/10.1016/S1003-6326\(11\)61460-X](https://doi.org/10.1016/S1003-6326(11)61460-X).
- (35) Pagnanelli, F.; Moscardini, E.; Altimari, P.; Abo Atia, T.; Toro, L. Cobalt Products from Real Waste Fractions of End of Life Lithium Ion Batteries. *Waste Manag.* **2016**, *51*, 214–221. <https://doi.org/10.1016/j.wasman.2015.11.003>.
- (36) Yang, Y.; Zheng, X.; Cao, H.; Zhao, C.; Lin, X.; Ning, P.; Zhang, Y.; Jin, W.; Sun, Z. A Closed-Loop Process for Selective Metal Recovery from Spent Lithium Iron Phosphate Batteries through Mechanochemical Activation. *ACS Sustain. Chem. Eng.* **2017**, *5* (11), 9972–9980. <https://doi.org/10.1021/acssuschemeng.7b01914>.
- (37) Zou, H.; Gratz, E.; Apelian, D.; Wang, Y. A Novel Method to Recycle Mixed Cathode Materials for Lithium Ion Batteries. *Green Chem.* **2013**, *15* (5), 1183–1191. <https://doi.org/10.1039/C3GC40182K>.
- (38) Shi, Y.; Chen, G.; Chen, Z. Effective Regeneration of LiCoO₂ from Spent Lithium-Ion Batteries: A Direct Approach towards High-Performance Active Particles. *Green Chem.* **2018**, *20* (4), 851–862. <https://doi.org/10.1039/C7GC02831H>.
- (39) Shi, Y.; Zhang, M.; Meng, Y. S.; Chen, Z. Ambient-Pressure Relithiation of Degraded Li_xNi_{0.5}Co_{0.2}Mn_{0.3}O₂ (0 < x < 1) via Eutectic Solutions for Direct Regeneration of Lithium-Ion Battery Cathodes. *Adv. Energy Mater.* **2019**, *9* (20), 1900454. <https://doi.org/10.1002/aenm.201900454>.

- (40) Xu, C.; Dai, Q.; Gaines, L.; Hu, M.; Tukker, A.; Steubing, B. Future Material Demand for Automotive Lithium-Based Batteries. *Commun. Mater.* **2020**, *1* (1), 1–10. <https://doi.org/10.1038/s43246-020-00095-x>.
- (41) Abbott, A. P.; Capper, G.; Davies, D. L.; Rasheed, R. K.; Tambyrajah, V. Novel Solvent Properties of Choline Chloride/Urea Mixtures Electronic Supplementary Information (ESI) Available: Spectroscopic Data. See <Http://Www.Rsc.Org/Suppdata/Cc/B2/B210714g/>. *Chem. Commun.* **2003**, No. 1, 70–71. <https://doi.org/10.1039/b210714g>.
- (42) Abbott, A. P.; Capper, G.; Davies, D. L.; McKenzie, K. J.; Obi, S. U. Solubility of Metal Oxides in Deep Eutectic Solvents Based on Choline Chloride. *J. Chem. Eng. Data* **2006**, *51* (4), 1280–1282. <https://doi.org/10.1021/je060038c>.
- (43) Tran, M. K.; Rodrigues, M.-T. F.; Kato, K.; Babu, G.; Ajayan, P. M. Deep Eutectic Solvents for Cathode Recycling of Li-Ion Batteries. *Nat. Energy* **2019**, *4* (4), 339–345. <https://doi.org/10.1038/s41560-019-0368-4>.
- (44) Fan, E.; Li, L.; Lin, J.; Wu, J.; Yang, J.; Wu, F.; Chen, R. Low-Temperature Molten-Salt-Assisted Recovery of Valuable Metals from Spent Lithium-Ion Batteries. *ACS Sustain. Chem. Eng.* **2019**, *7* (19), 16144–16150. <https://doi.org/10.1021/acssuschemeng.9b03054>.
- (45) Qu, X.; Xie, H.; Chen, X.; Tang, Y.; Zhang, B.; Xing, P.; Yin, H. Recovery of LiCoO₂ from Spent Lithium-Ion Batteries through a Low-Temperature Ammonium Chloride Roasting Approach: Thermodynamics and Reaction Mechanisms. *ACS Sustain. Chem. Eng.* **2020**, *8* (16), 6524–6532. <https://doi.org/10.1021/acssuschemeng.0c01205>.
- (46) Peng, C.; Liu, F.; Wang, Z.; Wilson, B. P.; Lundström, M. Selective Extraction of Lithium (Li) and Preparation of Battery Grade Lithium Carbonate (Li₂CO₃) from Spent Li-Ion Batteries in Nitrate System. *J. Power Sources* **2019**, *415*, 179–188. <https://doi.org/10.1016/j.jpowsour.2019.01.072>.
- (47) Wang, D.; Wen, H.; Chen, H.; Yang, Y.; Liang, H. Chemical Evolution of LiCoO₂ and NaHSO₄·H₂O Mixtures with Different Mixing Ratios during Roasting Process. *Chem. Res. Chin. Univ.* **2016**, *32* (4), 674–677. <https://doi.org/10.1007/s40242-016-5490-2>.
- (48) Wang, D.; Zhang, X.; Chen, H.; Sun, J. Separation of Li and Co from the Active Mass of Spent Li-Ion Batteries by Selective Sulfating Roasting with Sodium Bisulfate and Water Leaching. *Miner. Eng.* **2018**, *126*, 28–35. <https://doi.org/10.1016/j.mineng.2018.06.023>.
- (49) Lin, J.; Liu, C.; Cao, H.; Chen, R.; Yang, Y.; Li, L.; Sun, Z. Environmentally Benign Process for Selective Recovery of Valuable Metals from Spent Lithium-Ion Batteries by Using Conventional Sulfation Roasting. *Green Chem.* **2019**, *21* (21), 5904–5913. <https://doi.org/10.1039/C9GC01350D>.
- (50) Lin, J.; Li, L.; Fan, E.; Liu, C.; Zhang, X.; Cao, H.; Sun, Z.; Chen, R. Conversion Mechanisms of Selective Extraction of Lithium from Spent Lithium-Ion Batteries by Sulfation Roasting. *ACS Appl. Mater. Interfaces* **2020**, *12* (16), 18482–18489. <https://doi.org/10.1021/acsaami.0c00420>.

- (51) Tang, Y.; Qu, X.; Zhang, B.; Zhao, Y.; Xie, H.; Zhao, J.; Ning, Z.; Xing, P.; Yin, H. Recycling of Spent Lithium Nickel Cobalt Manganese Oxides via a Low-Temperature Ammonium Sulfation Roasting Approach. *J. Clean. Prod.* **2021**, *279*, 123633. <https://doi.org/10.1016/j.jclepro.2020.123633>.
- (52) Chen, H.; Hu, P.; Wang, D.; Liu, Z. Selective Leaching of Li from Spent LiNi_{0.8}Co_{0.1}Mn_{0.1}O₂ Cathode Material by Sulfation Roast with NaHSO₄·H₂O and Water Leach. *Hydrometallurgy* **2022**, *210*, 105865. <https://doi.org/10.1016/j.hydromet.2022.105865>.
- (53) Yang, C.; Zhang, J.; Cao, Z.; Jing, Q.; Chen, Y.; Wang, C. Sustainable and Facile Process for Lithium Recovery from Spent LiNi_xCo_yMn_zO₂ Cathode Materials via Selective Sulfation with Ammonium Sulfate. *ACS Sustain. Chem. Eng.* **2020**, *8* (41), 15732–15739. <https://doi.org/10.1021/acssuschemeng.0c05676>.
- (54) Moriyoshi, C.; Itoh, K.; Hikita, T. Structural Study of Phase Transition in K₂Co₂(SO₄)₃ Crystals. *J. Phys. Soc. Jpn.* **1995**, *64* (12), 4726–4732. <https://doi.org/10.1143/JPSJ.64.4726>.
- (55) Bhakay-Tamhane, S.; Sequiera, A.; Chidambaram, R. Structure of Lithium Potassium Sulphate, LiKSO₄: A Neutron Diffraction Study. *Acta Crystallogr. C* **1984**, *40* (10), 1648–1651. <https://doi.org/10.1107/S0108270184009045>.
- (56) McGinney, J. A. Redetermination of the Structures of Potassium Sulphate and Potassium Chromate: The Effect of Electrostatic Crystal Forces upon Observed Bond Lengths. *Acta Crystallogr. B* **1972**, *28* (9), 2845–2852. <https://doi.org/10.1107/S0567740872007022>.
- (57) Dubler, E.; Oswald, H. R. Ein neuartiges, niedrigbasisches Kobaltsulfat: Co₃(OH)₂(SO₄)₂·2 H₂O. *Naturwissenschaften* **1969**, *56* (6), 327–327. <https://doi.org/10.1007/BF00602175>.
- (58) Akimoto, J.; Gotoh, Y.; Oosawa, Y. Synthesis and Structure Refinement of LiCoO₂ Single Crystals. *J. Solid State Chem.* **1998**, *141* (1), 298–302. <https://doi.org/10.1006/jssc.1998.7966>.
- (59) Picard, J. P.; Baud, G.; Besse, J. P.; Chevalier, R. Croissance cristalline et étude structurale de Co₃O₄. *J. Common Met.* **1980**, *75* (1), 99–104. [https://doi.org/10.1016/0022-5088\(80\)90373-2](https://doi.org/10.1016/0022-5088(80)90373-2).
- (60) Tilley, R. J. D. *Colour and the Optical Properties of Materials: An Exploration of the Relationship Between Light, the Optical Properties of Materials and Colour*; John Wiley & Sons, 2010.
- (61) Nalini, G.; Row, T. N. G. Phase Transitions in A₄Li(HSO₄)₃(SO₄); A = Rb, K: Single Crystal X-Ray Diffraction Studies. *J. Chem. Sci.* **2003**, *115* (5), 473–490. <https://doi.org/10.1007/BF02708239>.
- (62) Ståhl, K.; Balic-Zunic, T.; da Silva, F.; Michael Eriksen, K.; Berg, R. W.; Fehrmann, R. The Crystal Structure Determinations and Refinements of K₂S₂O₇, KNa₂S₂O₇ and Na₂S₂O₇ from X-Ray Powder and Single Crystal Diffraction Data. *J. Solid State Chem.* **2005**, *178* (5), 1697–1704. <https://doi.org/10.1016/j.jssc.2005.03.022>.

- (63) Speer, D.; Salje, E. Phase Transitions in Langbeinites I: Crystal Chemistry and Structures of K-Double Sulfates of the Langbeinite Type $M_2 + K_2(SO_4)_3$, $M = Mg, Ni, Co, Zn, Ca$. *Phys. Chem. Miner.* **1986**, *13* (1), 17–24. <https://doi.org/10.1007/BF00307309>.
- (64) Zemann, A.; Zemann, J. Die Kristallstruktur von Langbeinit, $K_2Mg_2(SO_4)_3$. *Acta Crystallogr.* **1957**, *10* (6), 409–413. <https://doi.org/10.1107/S0365110X57001346>.
- (65) Oelkrug, H.; Brückel, T.; Hohlwein, D.; Hoser, A.; Prandl, W. The Magnetic Structure of the Langbeinite $K_2Mn_2(SO_4)_3$. *Phys. Chem. Miner.* **1988**, *16* (3), 246–249. <https://doi.org/10.1007/BF00220692>.
- (66) Lander, L.; Rouse, G.; Batuk, D.; Colin, C. V.; Dalla Corte, D. A.; Tarascon, J.-M. Synthesis, Structure, and Electrochemical Properties of K-Based Sulfates $K_2M_2(SO_4)_3$ with $M = Fe$ and Cu . *Inorg. Chem.* **2017**, *56* (4), 2013–2021. <https://doi.org/10.1021/acs.inorgchem.6b02526>.
- (67) Moriyoshi, C.; Itoh, K.; Hikita, T. Structural Study of Phase Transition in $K_2Co_2(SO_4)_3$ Crystals. *J. Phys. Soc. Jpn.* **1995**, *64* (12), 4726–4732. <https://doi.org/10.1143/JPSJ.64.4726>.
- (68) Moriyoshi, C.; Itoh, K. Structural Study of Phase Transition Mechanism of Langbeinite-Type $K_2Zn_2(SO_4)_3$ Crystals. *J. Phys. Soc. Jpn.* **1996**, *65* (11), 3537–3543. <https://doi.org/10.1143/JPSJ.65.3537>.
- (69) Percival, M. J. L.; Schmahl, W. W.; Salje, E. Structure of Cobalt Doped $K_2Cd_2(SO_4)_3$ Langbeinite at Three Temperatures above the P213-P212121 Phase Transition, and a New Trigger Mechanism for the Ferroelastic Transformation. *Phys. Chem. Miner.* **1989**, *16* (6), 569–575. <https://doi.org/10.1007/BF00202213>.
- (70) Tahoov, K. K.; ABOSEHLYa, A. M.; EL-SHARKAWYa, A. A. THERMAL STUDY OF THE PHASE TRANSITIONS. 7.
- (71) Vries, K. J. de; Gellings, P. J. The Thermal Decomposition of Potassium and Sodium-Pyrosulfate. *J. Inorg. Nucl. Chem.* **1969**, *31* (5), 1307–1313. [https://doi.org/10.1016/0022-1902\(69\)80241-1](https://doi.org/10.1016/0022-1902(69)80241-1).
- (72) Diosa, J. E.; Vargas, R. A.; Mina, E.; Torijano, E.; Mellander, B.-E. Phase Transitions of $KHSO_4$ above Room Temperature. *Phys. Status Solidi B* **2000**, *220* (1), 641–645. [https://doi.org/10.1002/1521-3951\(200007\)220:1<641::AID-PSSB641>3.0.CO;2-X](https://doi.org/10.1002/1521-3951(200007)220:1<641::AID-PSSB641>3.0.CO;2-X).
- (73) Lentz, G. Y.; Knorr, K.; Depmeier, W.; Baetz, C.; Knapp, M.; Morgenroth, W. Phase Transitions in Mercallite, $KHSO_4$. 2.
- (74) YOSHIDA, Y.; MATSUO, Y.; IKEHATA, S. NMR Study on Phase Transitions in $KHSO_4$. *Ferroelectrics* **2004**, *302* (1), 85–90. <https://doi.org/10.1080/00150190490456646>.
- (75) Yano, J.; Yachandra, V. K. X-Ray Absorption Spectroscopy. *Photosynth. Res.* **2009**, *102* (2), 241–254. <https://doi.org/10.1007/s11120-009-9473-8>.
- (76) Koningsberger, D. C.; Prins, R. X-Ray Absorption: Principles, Applications, Techniques of EXAFS, SEXAFS and XANES. **1987**.

- (77) Rehr, J. J.; Albers, R. C. Scattering-Matrix Formulation of Curved-Wave Multiple-Scattering Theory: Application to x-Ray-Absorption Fine Structure. *Phys. Rev. B* **1990**, *41* (12), 8139–8149. <https://doi.org/10.1103/PhysRevB.41.8139>.
- (78) Zabinsky, S. I.; Rehr, J. J.; Ankudinov, A.; Albers, R. C.; Eller, M. J. Multiple-Scattering Calculations of x-Ray-Absorption Spectra. *Phys. Rev. B* **1995**, *52* (4), 2995–3009. <https://doi.org/10.1103/PhysRevB.52.2995>.
- (79) Safarzadeh, Z.; Gomes, J. C.; Sirieix-Plénet, J.; Ruiz, N.; Hamitouche, L.; Michot, L.; Carré, L.; Barthe, L.; Briois, V.; Rollet, A.-L. Advanced Design of a X-Ray Absorption Spectroscopy Setup for Measuring Transition Metals Speciation in Molten Carbonates, Hydroxides and Hydrogenosulfates. *Rev. Sci. Instrum.* **2022**, *93* (7), 075102. <https://doi.org/10.1063/5.0087698>.
- (80) Mikkelsen, J. C.; Boyce, J. B.; Allen, R. Sample Cell for EXAFS Measurements on Molten Materials at Elevated Temperatures. *Rev. Sci. Instrum.* **1980**, *51* (3), 388–389. <https://doi.org/10.1063/1.1136190>.
- (81) Koyama, Y.; Arai, H.; Ogumi, Z.; Tanaka, I.; Uchimoto, Y. Co K -Edge XANES of LiCoO₂ and CoO₂ with a Variety of Structures by Supercell Density Functional Calculations with a Core Hole. *Phys. Rev. B* **2012**, *85* (7), 075129. <https://doi.org/10.1103/PhysRevB.85.075129>.
- (82) Juhin, A.; de Groot, F.; Vankó, G.; Calandra, M.; Brouder, C. Angular Dependence of Core Hole Screening in LiCoO₂: A DFT + U Calculation of the Oxygen and Cobalt K -Edge x-Ray Absorption Spectra. *Phys. Rev. B* **2010**, *81* (11), 115115. <https://doi.org/10.1103/PhysRevB.81.115115>.
- (83) Okumura, T.; Yamaguchi, Y.; Shikano, M.; Kobayashi, H. Correlation of Lithium Ion Distribution and X-Ray Absorption near-Edge Structure in O₃- and O₂-Lithium Cobalt Oxides from First-Principle Calculation. *J. Mater. Chem.* **2012**, *22* (33), 17340. <https://doi.org/10.1039/c2jm32024j>.
- (84) Slutsky, B. Handbook of Chemometrics and Qualimetrics: Part A By D. L. Massart, B. G. M. Vandeginste, L. M. C. Buydens, S. De Jong, P. J. Lewi, and J. Smeyers-Verbeke. Data Handling in Science and Technology Volume 20A. Elsevier: Amsterdam. 1997. Xvii + 867 Pp. ISBN 0-444-89724-0. \$293.25. *J. Chem. Inf. Comput. Sci.* **1998**, *38* (6), 1254–1254. <https://doi.org/10.1021/ci980427d>.
- (85) Kresse, G.; Hafner, J. Ab Initio Molecular Dynamics for Liquid Metals. *Phys. Rev. B* **1993**, *47* (1), 558–561. <https://doi.org/10.1103/PhysRevB.47.558>.
- (86) Kresse, G.; Furthmüller, J. Efficiency of Ab-Initio Total Energy Calculations for Metals and Semiconductors Using a Plane-Wave Basis Set. *Comput. Mater. Sci.* **1996**, *6* (1), 15–50. [https://doi.org/10.1016/0927-0256\(96\)00008-0](https://doi.org/10.1016/0927-0256(96)00008-0).
- (87) Blöchl, P. E. Projector Augmented-Wave Method. *Phys. Rev. B* **1994**, *50* (24), 17953–17979. <https://doi.org/10.1103/PhysRevB.50.17953>.
- (88) Perdew, J. P.; Burke, K.; Ernzerhof, M. Generalized Gradient Approximation Made Simple. *Phys. Rev. Lett.* **1996**, *77* (18), 3865–3868. <https://doi.org/10.1103/PhysRevLett.77.3865>.

- (89) Dudarev, S. L.; Botton, G. A.; Savrasov, S. Y.; Humphreys, C. J.; Sutton, A. P. Electron-Energy-Loss Spectra and the Structural Stability of Nickel Oxide: An LSDA+U Study. *Phys. Rev. B* **1998**, *57* (3), 1505–1509. <https://doi.org/10.1103/PhysRevB.57.1505>.
- (90) Ford, A.; Meehan, B.; Tariq, S. Molten Potassium Pyrosulfate: Reactions of Metals. *Aust. J. Chem.* **1982**, *35* (2), 437. <https://doi.org/10.1071/CH9820437>.
- (91) Berg, R. W.; Thorup, N. The Reaction between ZnO and Molten $\text{Na}_2\text{S}_2\text{O}_7$ or $\text{K}_2\text{S}_2\text{O}_7$ Forming $\text{Na}_2\text{Zn}(\text{SO}_4)_2$ or $\text{K}_2\text{Zn}(\text{SO}_4)_2$, Studied by Raman Spectroscopy and X-Ray Diffraction. *Inorg. Chem.* **2005**, *44* (10), 3485–3493. <https://doi.org/10.1021/ic0500513>.
- (92) Al-Shukry, R. M.; Jasim, F. Thermoanalytical Investigation of Some β -Manganese(IV)Oxide-Alkalimetalpersulfate Systems. *J. Therm. Anal.* **1980**, *19* (1), 125–132. <https://doi.org/10.1007/BF01928438>.
- (93) Mazur, M.; Gontarz, Z. Reactions of Manganese Oxides with $\text{K}_2\text{S}_2\text{O}_7$. *J. Therm. Anal. Calorim.* **2010**, *100* (3), 993–998. <https://doi.org/10.1007/s10973-009-0409-5>.
- (94) Guo, C.; Zhao, L.; Yang, J.; Wang, K.; Zou, J. A Novel Perspective Process for Alumina Extraction from Coal Fly Ash via Potassium Pyrosulfate Calcination Activation Method. *J. Clean. Prod.* **2020**, *271*, 122703. <https://doi.org/10.1016/j.jclepro.2020.122703>.
- (95) Salem, S. M.; Tariq, S. A. Molten Potassium Pyrosulphate: Reactions of Oxides of Ten Main-Group Elements. *Thermochim. Acta* **1997**, *307* (2), 123–125. [https://doi.org/10.1016/S0040-6031\(97\)00297-9](https://doi.org/10.1016/S0040-6031(97)00297-9).
- (96) Eriksen, K. M.; Fehrmann, R.; Hatem, G.; Gaune-Escard, M.; Lapina, O. B.; Mastikhin, V. M. Conductivity, NMR, Thermal Measurements and Phase Diagram of the $\text{K}_2\text{S}_2\text{O}_7$ - KHSO_4 System. *ECS Proc. Vol.* **1994**, *1994-13* (1), 124. <https://doi.org/10.1149/199413.0124PV>.
- (97) Fehrmann, R.; Hansen, N. H.; Bjerrum, N. J. Raman Spectroscopic and Spectrophotometric Study of the System Potassium Pyrosulfate-Potassium Hydrogen Sulfate in the Temperature Range 200–450.Degree.C. *Inorg. Chem.* **1983**, *22* (26), 4009–4014. <https://doi.org/10.1021/ic00168a038>.
- (98) Croguennec, L.; Palacin, M. R. Recent Achievements on Inorganic Electrode Materials for Lithium-Ion Batteries. *J. Am. Chem. Soc.* **2015**, *137* (9), 3140–3156. <https://doi.org/10.1021/ja507828x>.
- (99) Choi, S.; Manthiram, A. Factors Influencing the Layered to Spinel-like Phase Transition in Layered Oxide Cathodes. *J. Electrochem. Soc.* **2002**, *149* (9), A1157. <https://doi.org/10.1149/1.1497171>.
- (100) Sohr, J.; Voigt, W.; Zeng, D. IUPAC-NIST Solubility Data Series. 104. Lithium Sulfate and Its Double Salts in Aqueous Solutions. *J. Phys. Chem. Ref. Data* **2017**, *46* (2), 023101. <https://doi.org/10.1063/1.4977190>.
- (101) Wollmann, G. Crystallization Fields of Polyhalite and Its Heavy Metal Analogues. **2010**.

- (102) Li, B.; Li, J.; Fang, C.-H.; Wang, Q.-Z.; Song, P.-S. Study on Phase Diagrams and Properties of Solutions in Ternary Systems $\text{Li}^+, \text{K}^+(\text{Mg}^{2+})/\text{SO}_4^{2-}-\text{H}_2\text{O}$ at 25°C . *Chin. J. Chem.* **1995**, *13* (2), 112–117. <https://doi.org/10.1002/cjoc.19950130204>.
- (103) Sohr, J.; Voigt, W.; Zeng, D. IUPAC-NIST Solubility Data Series. 104. Lithium Sulfate and Its Double Salts in Aqueous Solutions. *J. Phys. Chem. Ref. Data* **2017**, *46* (2), 023101. <https://doi.org/10.1063/1.4977190>.
- (104) Melssner, H. P.; Kusik, C. L. Double Salt Solubilities. *Ind. Eng. Chem. Process Des. Dev.* **1979**, *18* (3), 391–394. <https://doi.org/10.1021/i260071a006>.

Abstract

Recycling of spent Li-ion batteries is mandatory to overcome economic and environmental problems caused by their storage. Here we propose a novel approach to chemically convert positive electrode material of spent Li-ion batteries into water-soluble sulfate product. The process includes solid-state reaction between LMO (M= cobalt, nickel, and manganese) and molten salt, yielding the formation of $K_2M_2(SO_4)_3$, $KLiSO_4$, and K_2SO_4 . In this work we have investigated the sulfation of $LiCoO_2$ using $KHSO_4$ and $K_2S_2O_7$ molten salts. In the case of $KHSO_4$, we showed that the process involves several steps implying a Li^+/H^+ ionic exchange between $LiCoO_2$ and $KHSO_4$, the formation of $Co_3(SO_4)_2(OH)_2$ intermediate, and final conversion into $K_2Co_2(SO_4)_3$. The sulfation of $LiCoO_2$ by $K_2S_2O_7$ is based on the Lux-Flood reaction between $K_2S_2O_7$ as the oxoacid and $LiCoO_2$ as the oxobase yielding the formation of $Li_{1-2x}\square_{2x}CoO_{2-x}\square_x$ (where \square represents a vacancy) which is converted into spinel Co_3O_4 prior to the formation of $K_2Co_2(SO_4)_3$.

Résumé:

Le recyclage des batteries Li-ion usagées est indispensable pour surmonter les problèmes économiques et environnementaux causés par leur stockage. Dans ces travaux, nous proposons une nouvelle approche pour convertir chimiquement le matériau de l'électrode positive des batteries Li-ion usagées en produit sulfate soluble dans l'eau. Le processus comprend une réaction à l'état solide entre le LMO (M= cobalt, nickel et manganèse) et le sel fondu, donnant lieu à la formation de $K_2M_2(SO_4)_3$, $KLiSO_4$ et K_2SO_4 . Dans ce travail, nous avons étudié la réaction impliquée lors de la sulfatation de $LiCoO_2$ en utilisant les sels fondus $KHSO_4$ et $K_2S_2O_7$. Dans le cas de $KHSO_4$, nous avons montré que le processus comporte plusieurs étapes impliquant un échange ionique Li^+/H^+ entre $LiCoO_2$ et $KHSO_4$, la formation d'un intermédiaire $Co_3(SO_4)_2(OH)_2$, et enfin la conversion en $K_2Co_2(SO_4)_3$. La sulfatation du $LiCoO_2$ par le sel fondu $K_2S_2O_7$ est basée sur la réaction de Lux-Flood entre l'oxoacide $K_2S_2O_7$ et l'oxobase $LiCoO_2$ donnant lieu à la formation de $Li_{1-2}\square_{2x}CoO_{2-x}\square_x$ (\square représente une lacune) qui est converti en spinelle Co_3O_4 avant la formation de $K_2Co_2(SO_4)_3$.